



ZnS and Cu_xS_y nanoparticles from dithiocarbamate ligands

BY

KHUMBLANI MNQIWU

DISSERTATION SUBMITTED IN PARTIAL FULFILMENT OF THE
REQUIREMENT FOR THE DEGREE MAGISTER TECHNOLOGIAE IN THE
FACULTY OF APPLIED AND COMPUTER SCIENCES AT VAAL
UNIVERSITY OF TECHNOLOGY

SUPERVISOR: Ms. T. XABA

CO-SUPERVISOR: PROF. M.J MOLOTO

ACADEMIC YEAR: 2017



DECLARATION STATEMENT

I hereby declare that the work on “ZnS and Cu_xS_y nanoparticles from dithiocarbamate ligands” is my work and all sources used are acknowledged by referencing.

K. MNQIWU (210117419)

..... **Date:**

SUPERVISOR: Ms. T. XABA

..... **Date:**

DEDICATION

I would like to dedicate this work to my late father (Zandisile Alfred Mnqiwu), thank you dad I wish you were here to see me prosper just the way I always told you I would. At this stage I would like to think that I'm keeping the promises I made to you. You'll always be remembered and loved father.

ACKNOWLEDGEMENTS

I would like to pass my deepest gratitude to my supervisors Ms. T. Xaba and Prof. MJ Moloto for their tireless encouragements, guidance, and motivation throughout this dissertation. I would specifically like to thank Prof. MJ Moloto for his dedication towards this work even when my main supervisor (Ms. Xaba) was not around he was always there, even when I thought he was hard on me but that strictness payed off eventually. So thank you very much Prof. no words can describe how grateful I am, but I hope to repay you by being the best student you always pushed me to be. I would like to thank the source of funding, that sponsored this project and made it happen: National Research Foundation (NRF) and VUT Hub and Spokes. My other special thanks goes to Thapelo Mofokeng, thank you very much my friend for being the best research partner, you played a vital role in this dissertation in many ways because you have been there from the word go until the end. We had sleepless nights together going back and forth to the lab and library in the morning and at night. To the NCAP (Nano-Catalysis-Adsorption-Phytochemistry) group, you have become my second family because you shaped and groomed me into a person I never thought I would be, your advices gave me direction when I was lost and without hope. Those times we had talking about research have opened my eyes and taught me to be open minded about chemistry because now I have basic understanding in several fields (catalysis, organic synthesis, adsorption and medicinal chemistry). To the other Moloto group at Wits I am grateful for the times we spent together presenting to each other sharing eye opening advices, therefore you guys are the best especially Prof. Nosipho Moloto who always have a brilliant opinion that gives you direction, I'm grateful for that. I would also like to thank special individuals from Mintek who played a crucial role in this work, they played a big part in a way that I wish I had something to repay them with.

Those individuals are: Mr. Sanele Nyembe, Mr. Phumlani Tetyana and Dr. Poslet Shumbula. To those I didn't mention by names just know that your contributions meant a lot to me and they are the reason why I have completed this dissertation.

To my family and friends, I would like to thank my mother (Nothembele Mnqiwu) she is the best mother in the world. Without my father she has been the pillar of my strength and the reason why I want to be best. Because she accepted the fact that at home there's no bread winner and my education meant a lot to me, she never criticized my decision to pursue my educational studies even though I felt I was selfish, she told me that everything can wait until I feel I have accomplished my dream of being a doctor because I always believe that one day she'll be the happiest woman on earth after my PhD studies. Thank you very much mommy God made you my mom for a reason, I thank the almighty for that. I would also like to thank my siblings, my brothers: Silungile Mnqiwu, Masibonge Mnqiwu, Masixole Mnqiwu, and Sibulelo Mnqiwu not forgetting my cousin who is also my brother Fikelela Mnqiwu, my sisters: Nothembisa Mnqiwu, Nomveliso Mnqiwu, Siphokazi Mnqiwu and Busisiwe Mnqiwu. The best family is the family that supports you without expectations and that is how I describe you guys and I thank the fact that we never separated we have always been united even in tough times you never judged me for furthering my studies instead you saw me as a role model. I would also like to send my heartfelt gratitude to the second woman after my mother, Lesego Princess Moagi, thank you for your understanding and support even when I didn't believe I would finish you always guided me towards the right paths, your encouragement and believe you had in me gave me strength and forced me to believe in myself. The other person I would like to thank for the support and believe is Ms. Mahadi Lesaoana, she has been the consistent reminder that I know more than I could imagine, so thank you so much for those bold words of courage I really appreciate that. I would like to thank my son (Sibusiso

Shaun Moagi) who always put a smile on my face even when he is on his worst behavior, thank you my boy you played a crucial role in this work because I always think I should set a right path for you and by doing my best at school, I thought you would follow me in the same direction

To Vaal University of Technology I am very grateful for the opportunity of using your premises.

The first and the last thanks goes to the almighty God for keeping me safe and guiding me towards the right direction.

LIST OF PUBLICATIONS AND PRESENTATIONS

Presentations

“ZnS and Cu_xS_y nanoparticles from aniline dithiocarbamate ligand” Oral presentation at SACI Young Chemist Symposium held at UNISA, South Africa. November 2015

“ZnS and Cu_xS_y nanoparticles from aniline dithiocarbamate ligand” Poster presentation at SACI 2015 Convention held in Durban, South Africa. December 2015

“Copper sulfide nanoparticles from cyclohexylamine-N-dithiocarbamate ligand” Oral presentation at 1st VUT Interdisciplinary Research and Postgraduate Conference held at VUT, South Africa. November 2016. **WON 1st PRIZE**

“Copper sulfide nanoparticles from cyclohexylamine-N-dithiocarbamate ligand” Poster presentation at International Conference on Environment, Materials and Green Technology held at VUT, South Africa. November 2016.

“Copper sulfide nanoparticles from the cyclohexylamine-N-dithiocarbamate ligand and their antimicrobial activity” Oral presentation at the 13th International Conference on Nanotek and Expo held during December 2016 in Phoenix, USA.

Publication(s)

MNQIWU, K., XABA, T., MOLOTO, M.J., MUBIAYI, P.K., NYAMUKAMBA, P. & SIBOKOZA, S.B.
Plasmonic electron deficient Cu_{2-x}S semiconductor nanoparticles from cyclohexylamine-N-dithiocarbamate ligand. *Mater. Lett.* **199** (2017) pp. 28–31.

ABSTRACT

Dithiocarbamate ligands and their complexes has been a subject of interest in various fields but they found much interest in medical applications as potential anti-microbial agents. The dithiocarbamate ligands were used to prepare complexes of copper and zinc. All the prepared ligands and complexes were characterized using techniques such as IR and ^{13}C NMR spectroscopy and thermogravimetric analysis (complexes). The data obtained from the spectroscopies was consistent with the coordination of the ligand to the metal ion through the sulfur atoms of the dithiocarbamate or thioureide moiety. The thermal analysis of the prepared complexes gave a final residue of metal sulfide, thus indicating the potential of the prepared complexes as single molecular precursor for the synthesis of metal sulfide nanoparticles.

The prepared complexes were then used to synthesize metal sulfide nanoparticles. The nanoparticles were successfully prepared by thermal decomposition of a single-source precursor (dithiocarbamate complexes) in a solution of hexadecylamine (HDA) or tri-n-octylphosphine oxide (TOPO). The investigated parameters were the capping molecule (HDA and TOPO), and capping molecule concentration (3 g and 6 g) to see their effect on the shape and size of the synthesized nanomaterials. The synthesized metal sulfide nanoparticles were characterized using techniques such as UV-vis spectroscopy, photoluminescence spectroscopy, X-ray diffraction analysis and transmission electron microscopy.

The absorption study showed some interesting features in the prepared nanomaterials. The first was the red-shifted spectra of the ZnS nanoparticles which was attributed to the impurities and that assumption was further confirmed by the XRD analysis that showed a sulfur impurity and other amorphous peaks. The second was the localized surface plasmon resonances on the copper sulfide

nanoparticles that suggested the formation of electron deficient copper sulfide stoichiometry that was further confirmed by XRD analysis that gave hexagonal phase copper sulfide covellite. The TEM images of the prepared nanoparticles showed that the concentration and the capping molecule has an effect on the size and shape of the synthesized nanoparticles. The increase in capping concentration gave a decrease in particle size in most of the prepared nanoparticles, while they were few exceptions. The capping molecule effect showed that most of the nanoparticles prepared from TOPO were spherical in shape and were well dispersed compared to the mixed morphological nanoparticles prepared from HDA. There were also exceptions of the well dispersed HDA-capped nanoparticles.

Contents

DECLARATION STATEMENT	i
DEDICATION	ii
ACKNOWLEDGEMENTS	iii
LIST OF PUBLICATIONS AND PRESENTATIONS	vi
ABSTRACT	vii
LIST OF FIGURES	xii
LIST OF TABLES	xiv
LIST OF ABBREVIATIONS	xv
Chapter 1	1
Introduction and literature review.....	1
1.1 Background on dithiocarbamates (DTC's)	1
1.2 Binding modes	3
1.3 Complexes (from sulfur based ligands)	6
1.3.1 Xanthate complexes	7
1.3.2 Dithiophosphates	8
1.3.3 Dithiocarbamates	9
1.4 General introduction of nanotechnology.....	10
1.4.1 Nanoparticle properties	12
1.4.1.1 Semiconductor nanoparticles or quantum dots (QD's).....	14
1.4.1.1. (i). ZnS nanoparticles.....	16
1.4.1.1. (ii). CuS nanoparticles.....	17
1.4.1.2 Surface plasmon resonance (SPR)	20
1.5 Nanoparticle synthesis methods.....	22
1.5.1 Colloidal method.....	23
1.5.2 Hydro/Solvothermal method.....	24
1.5.3 Single-source precursor method.....	25
1.6 Potential applications of nanoparticles	27
1.6.1 Biological applications.....	27
1.6.2 Solar cells.....	28
1.7 Aims and objectives	29
1.8 References.....	30

Chapter 2	43
Methodology	43
2. Experimental	43
2.1 Materials and reagents	43
2.2 Instrumentation	43
2.2.1 Fourier transform infrared (FTIR) spectroscopy.....	43
2.2.2 Solid state nuclear magnetic resonance (NMR) spectroscopy	43
2.2.3 Thermogravimetric analysis (TGA).....	44
2.2.4 Ultra-violet visible (UV-vis) spectrometry	44
2.2.5 Photoluminescence (PL) spectroscopy	44
2.2.6 X-ray diffraction (XRD) analysis	44
2.2.7 Transmission electron microscopy (TEM).....	45
2.3 Experimental procedure	45
2.3.1 Preparation of cyclohexylamine-N-dithiocarbamate ligand (Ligand 1).....	45
2.3.2 Preparation of transition metal complexes.....	46
2.3.2.1 Preparation of bis (cyclohexylamine-N-dithiocarbamato) copper (II)/zinc (II)	46
2.3.2.2 Preparation of bis (pyrrolidine-N-dithiocarbamato) copper (II)/zinc (II)	46
2.3.3 Synthesis of metal sulfide nanoparticles	47
2.4 References.....	47
Chapter 3	49
Characterization of dithiocarbamate (DTC) ligands and complexes	49
3.1 Introduction and spectral analysis of the ligands and complexes	49
3.1.1 Cyclohexylamine-N-dithiocarbamate ligand (Ligand 1) and its zinc complex, 1	53
3.1.2. Cyclohexylamine-N-dithiocarbamate ligand 1 and its copper complex, 2	56
3.1.3. N-Phenyldithiocarbamate ligand (ligand 2) and its zinc complex, 3	57
3.1.4. N-Phenyldithiocarbamate ligand 2 and its copper complex, 4	59
3.1.5 Ammonium pyrrolidinedithiocarbamate ligand and their complexes.....	61
3.2. ¹³ C nuclear magnetic resonance (NMR) spectra studies of the ligands	64
3.2.1 Cyclohexylamine-N-dithiocarbamate ligand (Ligand 1)	65
3.2.2 bis(cyclohexylamine-N-dithiocarbamato)Zn(II) [complex 1]	66
3.2.3 N-Phenyldithiocarbamate ligand (Ligand 2).....	67
3.2.4. bis(N-phenyldithiocarbamato)Zn(II) [complex 3]	68
3.2.5 Ammonium pyrrolidine dithiocarbamate ligand (Ligand 3).....	69

3.2.6. bis(N-pyrrolidinedithiocarbamato)Zn(II) complex (complex 5).....	70
3.4 Thermal studies of complexes.....	72
3.4.1 Cyclohexylamine complexes	72
3.4.2 N-phenyldithiocarbamato complexes	74
3.4.3 N-pyrrolidinedithiocarbamato complexes.....	75
3.5 Conclusion	76
3.6 References.....	77
Chapter 4	81
Characterization of metal sulfide (capped) nanoparticles	81
4.1 Introduction.....	81
4.2 Results and discussion	82
4.2.1 Copper sulfide nanoparticles.....	83
4.2.1.1 Optical properties.....	83
4.2.1.2 Powder X-ray diffraction analysis	90
4.2.1.3 Transmission electron microscopy (TEM) images	91
4.2.2 Zinc sulfide nanoparticles	108
4.2.2.1 Optical properties.....	108
4.2.2.2 Powder X-ray diffraction analysis	114
4.2.2.3 Transmission electron microscopy (TEM images)	116
4.3 Conclusion	131
4.4 References.....	132
Chapter 5	137
Overall conclusions, recommendations and future work.....	137
5.1 Overall conclusions.....	137
5.2 Recommendations and future work	139

LIST OF FIGURES

CHAPTER 1

Figure 1.1: Resonance structures of dithiocarbamate ligand	2
Figure 1.2: Dithiocarbamate binding modes.....	4
Figure 1.3: Nanometer-scale of comparison with common objects (Tyner, 2015).	12
Figure 1.4: Schematic energy level structure of (left) molecular dye, (center) quantum dots, and (right) bulk semiconductor (O’Farrell et al., 2006).....	16

CHAPTER 3

Figure 3.1: Resonance forms of dithiocarbamic-NCS ₂ - moiety (Alverdi et al., 2004)	52
Figure 3.2: FTIR spectra of (a) Pristine cyclohexylamine, (b) Ligand 1, and (c) Complex 1	54
Figure 3.3: FTIR spectra of (a) Ligand 1 and (b) complex 2.....	56
Figure 3.4: FTIR spectra of (a) Pristine Aniline, (b) Ligand 2, and (c) Complex 3	58
Figure 3.5: FTIR spectra of (a) Complex 4 and (b) Ligand 2.....	61
Figure 3.6: FTIR spectra of (a) Ligand 2, (b) Complex 5 and (c) Complex 6.....	62
Figure 3.7: NMR spectrum of cyclohexylamine-N-dithiocarbamate ligand	66
Figure 3.8: NMR spectrum of bis(cyclohexylamine-N-dithiocarbamato)Zn(II) complex.	67
Figure 3.9: NMR spectrum of N-phenyldithiocarbamate ligand.	68
Figure 3.10: NMR spectrum of bis(N-phenyldithiocarbamato)Zn(II) complex (complex 3).....	69
Figure 3.11: NMR spectrum of ammonium pyrrolidine dithiocarbamate (APDTC) ligand.....	70
Figure 3.12: NMR spectrum of bis(N-pyrrolidinedithiocarbamato)Zn(II) complex (complex 5).....	71
Figure 3.13: TGA and DTA curves of (a) complex 2 and (b) complex 1.....	73
Figure 3.14: TGA and DTA curves of (a) complex 3 and (b) complex 4.....	74
Figure 3.15: TGA and DTA curves of (a) complex 5 and (b) complex 6.....	76

CHAPTER 4

Figure 4.1: Absorption spectra of Cu _{2-x} S nanoparticles in [A] (i) 3g-HDA and (ii) 6g-HDA, [B] (inset Tauc plot).....	86
Figure 4.2: Emission spectra of Cu _{2-x} S nanoparticles in (a) 3g-HDA and (b) 6g-HDA.	87
Figure 4.3: Absorption spectra of Cu _{2-x} S nanoparticles in [A] (i) 3g-TOPO and (ii) 6g-TOPO, [B] Inset Tauc plot of the prepared nanoparticles.	88
Figure 4.4: Emission spectra of Cu _{2-x} S nanoparticles in (a) 3g-TOPO and (b) 6g-TOPO.....	89
Figure 4.5: XRD patterns of CuS nanoparticles synthesized in (a) HDA and (b) TOPO.....	90
Figure 4.6: TEM images and histograms of CuS nanoparticles prepared in (a) 3g HDA, (b) 6g HDA, (c) 3g TOPO and (d) 6g TOPO.	92
Figure 4.7: Absorption spectra of Cu _{2-x} S nanoparticles in [A] (i) 3g-HDA and (ii) 6g-HDA, [B] (inset Tauc plot).....	93
Figure 4.8: Emission spectra of Cu _{2-x} S nanoparticles in (a) 3g-HDA and (b) 6g-HDA.	94
Figure 4.9: Absorption spectra of Cu _{2-x} S nanoparticles in [A] (i) 3g-TOPO and (ii) 6g-TOPO, [B] (inset Tauc plot).....	95

Figure 4.10: Emission spectra of Cu _{2-x} S nanoparticles in (a) 3g-TOPO and (b) 6g-TOPO.....	97
Figure 4.11: XRD patterns of CuS nanoparticles synthesized in (a) (i) 3g, (ii) 6g HDA and (b) (i) 3g, (ii) 6g TOPO.	98
Figure 4.12: TEM images and histograms of CuS nanoparticles prepared in (a) 3g HDA, (b) 6g HDA, (c) 3g TOPO and (d) 6g TOPO.	99
Figure 4.13: Absorption spectra of Cu _{2-x} S nanoparticles in [A] (i) 3g-HDA and (ii) 6g-HDA, [B] (inset Tauc plot).....	101
Figure 4.14: Emission spectra of Cu _{2-x} S nanoparticles in (a) 3g-HDA and (b) 6g-HDA	102
Figure 4.15: Absorption spectra of Cu _{2-x} S nanoparticles in [A] (i) 3g-TOPO and (ii) 6g-TOPO, [B] (inset Tauc plot).....	103
Figure 4.16: Emission spectra of Cu _{2-x} S in (a) 3g-TOPO and (b) 6g-TOPO.....	104
Figure 4.17: XRD patterns of CuS nanoparticles synthesized in (a) (i) 3g, (ii) 6g HDA and (b) (i) 3g, (ii) 6g TOPO.	105
Figure 4.18: TEM images and histograms of CuS nanoparticles prepared in (a) 3g HDA, (b) 6g HDA, (c) 3g TOPO and (d) 6g TOPO.	107
Figure 4.19: Absorption spectra of ZnS nanoparticles in [A] (i) 3g-HDA and (ii) 6g-HDA, [B] (inset Tauc plot).....	111
Figure 4.20: Emission spectra of ZnS nanoparticles in (a) 3g-HDA and (b) 6g-HDA.....	112
Figure 4.21: Absorption spectra of ZnS nanoparticles in [A] (i) 3g-TOPO and (ii) 6g-TOPO, [B] (inset Tauc plot).....	113
Figure 4.22: Emission spectra of ZnS nanoparticles in (a) 3g-TOPO and (b) 6g-TOPO	114
Figure 4.23: XRD patterns of ZnS nanoparticles synthesized in (a) (i) 3g, (ii) 6g HDA and (b) (i) 3g, (ii) 6g TOPO.	115
Figure 4.24: TEM images and histograms of ZnS nanoparticles prepared in (a) 3g HDA, (b) 6g HDA, (c) 3g TOPO and (d) 6g TOPO	117
Figure 4.25: Absorption spectra of ZnS nanoparticles in [A] (i) 3g-HDA and (ii) 6g-HDA, [B] (inset Tauc plot).....	118
Figure 4.26: Emission spectra of ZnS nanoparticles in (a) 3g-HDA and (b) 6g-HDA.....	119
Figure 4.27: XRD patterns of ZnS nanoparticles synthesized in (a) (i) 3g, (ii) 6g HDA and (b) (i) 3g, (ii) 6g TOPO	120
Figure 4.28: TEM images and histograms of ZnS nanoparticles prepared in (a) 3g HDA, (b) 6g HDA, (c) 3g TOPO and (d) 6g TOPO.	122
Figure 4.29: Absorption spectra of ZnS nanoparticles in [A] (i) 3g-HDA and (ii) 6g-HDA, [B] (inset Tauc plot).....	123
Figure 4.30: Emission spectra of ZnS nanoparticles in (a) 3g-HDA and (b) 6g-HDA.....	124
Figure 4.31: Absorption spectra of ZnS nanoparticles in [A] (i) 3g-TOPO and (ii) 6g-TOPO, [B] (inset Tauc plot).....	125
Figure 4.32: Emission spectra of ZnS nanoparticles in (a) 3g-TOPO and (b) 6g-TOPO	127
Figure 4.33: XRD patterns of ZnS nanoparticles synthesized in (a) (i) 3g, (ii) 6g HDA and (b) (i) 3g, (ii) 6g TOPO.	128
Figure 4.34: TEM images and histograms (a and d) of CuS nanoparticles prepared in (a) 3g HDA, (b) 6g HDA, (c) 3g TOPO and (d) 6g TOPO.	129
Figure 1.1: Resonance structures of a dithiocarbamate ligand.....	2
Figure 1.2: Dithiocarbamate binding modes	4
Figure 1.3: Nanometer-scale of comparison with common objects (Tyner, 2015).....	12

Figure 1.4: Schematic energy level structure of (left) molecular dye, (center) quantum dots, and (right) bulk semiconductor (O'Farrell et al., 2006). 16

LIST OF TABLES

Tables

Table 1: Major types of 1,1-dithiolates (Cotton et al., 1996).	6
Table 2: Diagnostic IR bands of all ligands and their complexes.....	51
Table 3: Comparison of selected peaks from FTIR spectra with literature	63
Table 4: ¹³ C NMR spectral data of NCS ₂ moiety for the ligands and complexes	65
Table 5: Summarized NMR spectrum signals of ligands and complexes.....	71
Table 6: Summarized CuS nanoparticles results from the copper complexes.....	108
Table 7: Summarized results of ZnS nanoparticles prepared from Zn complexes	131
Table 8: Mole ratio of complex to capping agent concentration	141

Schemes

Scheme 3. 1: Reaction for the formation of ligand, and complexes via (i) monodentate and (ii) bidentate bonding	55
Scheme 3. 2: Reaction for the formation of aniline ligand and its corresponding complexes.....	60
Scheme 2.1: Synthetic pathway to make the ligands	46
Scheme 2.2: Synthetic pathway to make the complexes.....	46
Scheme 3. 1: Reaction for the formation of ligand, and complexes via (i) monodentate and (ii) bidentate bonding.....	55
Scheme 3. 2: Reaction for the formation of aniline ligand and its corresponding complexes.....	60

LIST OF ABBREVIATIONS

DTC's	Dithiocarbamates
NP's	Nanoparticles
°C	Degree celcius
Cyc	Cyclohexylamine
Pyr	Pyrrolidine
ADTC	Aniline dithiocarbamate
PDTC	Pyrrolidine dithiocarbamate
CDTC	Cyclohexylamine dithiocarbamate
HDA	Hexadecylamine
TOPO	Tri-octylphosphine-n-oxide
TOP	Tri-octylphosphine
OLA	Oleylamine
Ligand 1	Cyclohexylamine-N-dithiocarbamate
Ligand 2	N-phenylaminedithiocarbamate
Ligand 3	Ammonium pyrrolidine dithiocarbamate
Complex 1	Bis(cyclohexylamine-N-dithiocarbamato)Zn(II)
Complex 2	Bis(cyclohexylamine-N-dithiocarbamato)Cu(II)
Complex 3	Bis(N-phenylaminedithiocarbamato)Zn(II)
Complex 4	Bis(N-phenylaminedithiocarbamato)Cu(II)
Complex 5	Bis(N-pyrrolidinedithiocarbamato)Zn(II)
Complex 6	Bis(N-pyrrolidinedithiocarbamato)Cu(II)
FTIR	Fourier transform infrared spectroscopy
NMR	Nuclear magnetic resonance spectroscopy
TEM	Transmission electron microscopy
XRD	X-ray diffraction

Chapter 1

Introduction and literature review

1.1 Background on dithiocarbamates (DTC's)

Dithiocarbamates (DTC's) are a class of organic compounds known as the 1,1-dithiolates (Cocouvanis, 1979) that consists of nitrogen, carbon, and sulfur, with a formula $R_2NCS_2^-$ where R = alkyl, aryl, vinyl etc. They are mostly prepared by reaction of carbon disulfide and an amine (primary or secondary) in the presence of a strong base. They exhibit a rich coordination chemistry with a variety of transition metals (Ivanov et al., 2001). The DTC ligands consist of nitrogen (hard) and sulfur (soft) atoms, which can be utilized for coordination with the metal center upon complexation. DTC ligands form chelates with all transition metals ions through its two sulfur donor atoms, displaying both mono and bidentate coordination with a transition metal ion (Hogarth, 2005) and (Shaheen et al., 2007). They have very strong complexing capabilities with a wide range of metal ions, forming stable complexes. The sulfur atoms of the dithiocarbamate ligands possess δ -donor and π -back-donation characteristics, with a special feature of π -electron flow from the nitrogen to the sulfur atom via a planar delocalized π -orbital system. This makes them strong electron donors able to accommodate metal ions in higher oxidation states, as shown below (**Figure 1.1**). They are described by four resonance structures.

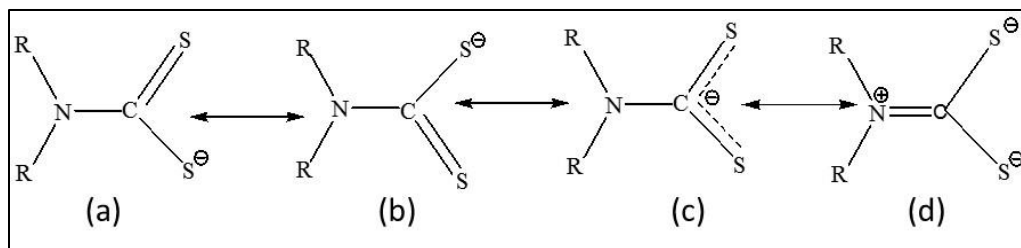


Figure 1.1: Resonance structures of a dithiocarbamate ligand

Fig 1.1(a-c) shows the dithiocarbamate form of the resonance while Fig 1.1 (d) shows the thioureide form of resonance. In the dithiocarbamate form of resonance, the single bond between the nitrogen and the sulfur bearing carbon atoms is maintained, and the delocalization of the -1 charge occurs only between the carbon and the two sulfur atoms. The thioureide form consists of a double bond between the nitrogen and the sulfur bearing carbon atom. This double bond results from the delocalization of the lone pair on the nitrogen atom and this gives a negative charge on the two sulfur atoms. This nitrogen then becomes sp^2 hybridized in the thioureide resonance. The dithiocarbamate resonance is said to be a soft ligand (stabilize soft metals in lower oxidation states), while the latter is a hard ligand (stabilize hard metals in higher oxidation states). Another interesting feature of the dithiocarbamates is their ability to act as both a *strong-* and *weak-field* ligand, showing the flexibility of the DTC's (Hogarth, 2005). Thus, if the DTC's resonance form dominates then it would be considered a *strong-field* ligand (low-spin), while if the thioureide resonance form dominates it is considered a *weak-field* ligand (high-spin) (Hogarth, 2005). The mentioned resonance phenomena does comply with other compounds but does not to others. An interesting instance was the study of pyrrole dithiocarbamate, which was reported to only favor the DTC's resonance (*strong-field*) form, due to the reluctance of the pyrrole ring to donate π -electron density to the CS_2 fragment (Robert Daniel Bereman & Nalewajek, 1978), (Kellner et al.,

1974), (Bereman & Nalewajek, 1977), (Anderson & Baird, 1988), (Herrick et al., 1983), (Bereman et al., 1979), (Robert D. Bereman & Nalewajek, 1978), (Herrick & Templeton, 1986), (Bereman et al., 1983), (Baird et al., 1985) and (El A'mma & Drago, 1977). In contrast to the pyrrole DTC complex, the pyrrolidine DTC complex (one of the studied complex in this work) showed a high-spin (*weak-field*) behavior (Bereman & Nalewajek, 1977) and (Bereman et al., 1979). This thus makes pyrrole DTC a poor electron donor as compared to other DTC compounds. Their resonances bring about strong electron donation between the metal and the ligand causing a high electron density around the metal ion, thus leading the metal to its next higher oxidation state (Pandeya et al., 1986). The next section will further elaborate on this resonance and binding modes of the sulfur to the metal and other possible coordination modes.

1.2 Binding modes

Dithiocarbamates are versatile types of ligands that are known to bind to metals in many different ways. Their diverse nature of ligation is illustrated in **Figure 1.2**, where the ligand moiety can act as either a monodentate, bidentate or as multidentate ligand. DTC's can accommodate one to four transition metal atoms using various ways that are shown in **Figure 1.2** (Cotton et al., 1996). Their versatility is clearly shown by nine types of coordination modes (**Fig. 1.2**) and in these nine coordination modes, six of them are a common type of coordination while the other three are very rare (Hogarth, 2012).

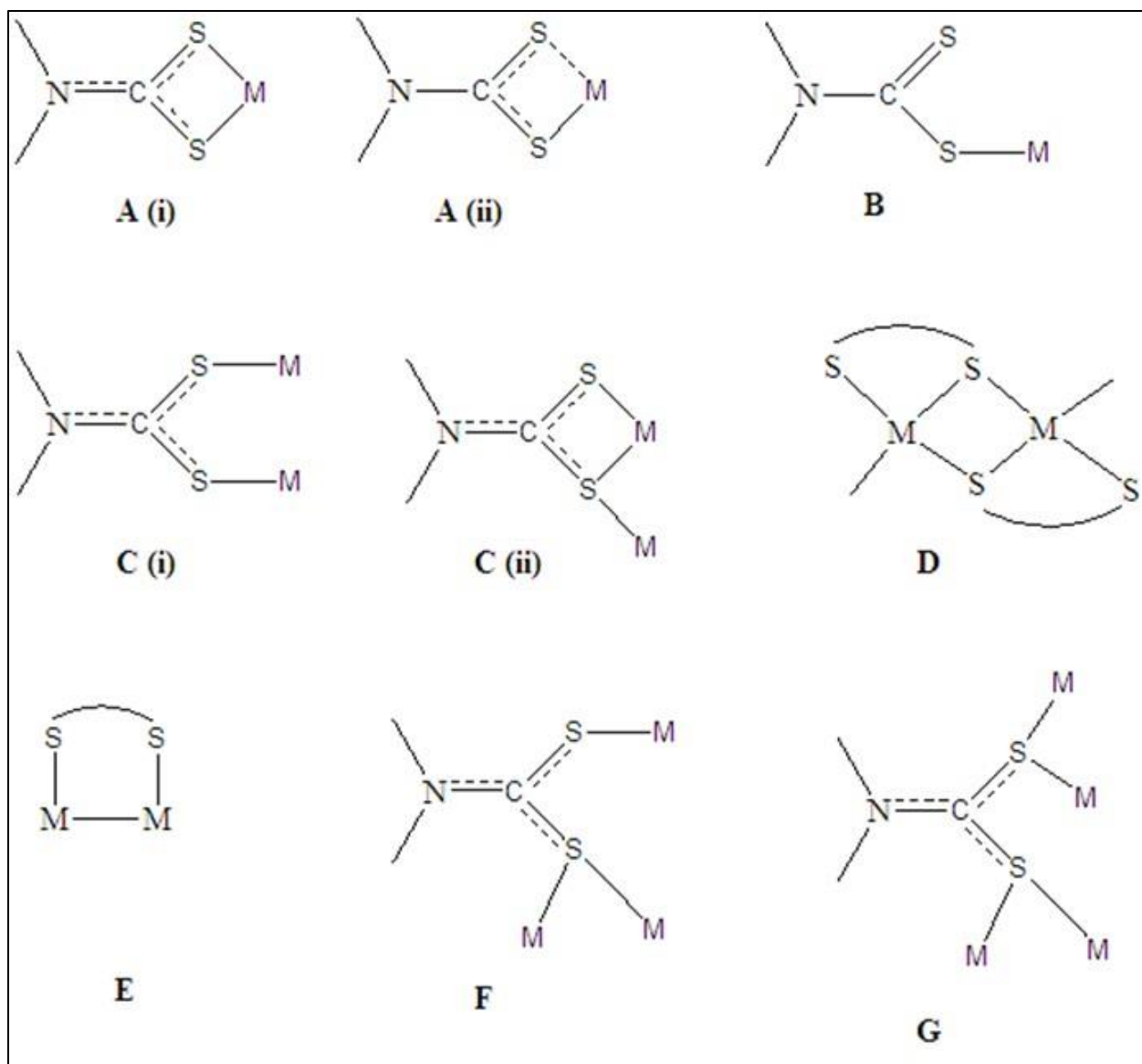


Figure 1.2: Dithiocarbamate binding modes

By far, the most common type of bonding is the *bidentate* coordination mode. In *bidentate* coordination two sulfur atoms are covalently coordinated to the same metal atom, forming a four coordinate ring chelate. *Bidentate* coordination can be either **A(i)** symmetrical by involving two sulfur atoms and/or **A(ii)** asymmetrical by involving one sulfur atom and these types of

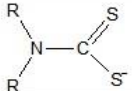
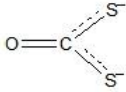
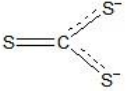
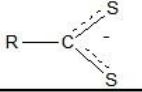
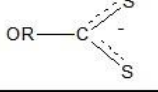
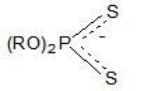
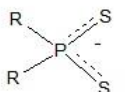
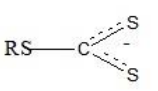
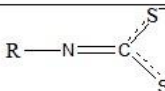
coordination are also known as the *aniso-bidentate* coordination mode. The bidentate mode is a common bonding in almost all transition metals in all accessible oxidation states (Cotton et al., 1996). The other relatively common type of coordination is the *monodentate* coordination mode **(B)**. Only one of the sulfurs is covalently bonded to the metal ion in *monodentate* binding. The coordination is highly asymmetrical with an unequal C-S bond in each dithiocarbamate ligand. It consists of a short and a long C-S bond for both dithiocarbamate ligands (Coucouvanis, 1979). This type of bonding is common in gold DTC complexes (Noordik, 1973), it occurs when there is no room for bidentate coordination, due to electronic demands of a metal center (Hogarth, 2012). Then due to the flexibility of the dithiocarbamate ligands, bridging of metals can occur forming dimeric structures from **(C-F)**, where sulfur can bind to more than one different metal up to a maximum of four metals (Hogarth, 2005). A face-capped copper cube $[\text{Cu}_8(\mu_4\text{-S}_2\text{CNPr}_2)_6][\text{ClO}_4]_2$ is the reported example of bridging metal atoms (Cardell et al., 2006). One sulfur atom can also bridge two metal centers in such a way that the three M-S interactions are equivalent as shown in mode **D**. In **E-F** both sulfur atoms bridge three metal centers in different ways (Knight et al., 2009). The ligand can also accommodate four metals as shown in mode **G** to four metal atoms, even though these type of binding modes are rare and limited to other transition metals (Mamba, 2011). Their ligand versatility makes dithiocarbamates the most studied type of ligands and their complexes become the most sort after in new developing technologies. In this study, the complexes of Zn and Cu dithiocarbamates are explored for the synthesis of ZnS and CuS nanoparticles.

1.3 Complexes (from sulfur based ligands)

The significance of carbon disulfide as a source of sulfur has been studied for over a century (Galindo et al., 1999). CS₂ reacts with a primary or secondary amine in a basic medium to produce dithiocarbamates, its reaction with metal alkoxides in an alcohol produces xanthates, and another reaction with Grignard reagents produces dithiocarboxylates and many other 1,1 dithiolates compounds. In the major types of 1,1-dithiolate ligands, only few will be selected and discussed.

Table 1 shows the 1,1-dithiolate compounds.

Table 1: Major types of 1,1-dithiolates (Cotton et al., 1996).

Composition	Structure	Name
R ₂ NCS ₂ ⁻		Dithiocarbamates
OCS ₂ ²⁻		Dithiocarbonate
CS ₃ ²⁻		trithiocarbonate
RCS ₂ ⁻		Dithiocarboxylate
ROCS ₂ ⁻		Xanthate
(RO) ₂ PS ₂ ⁻		Dithiophosphate
R ₂ PS ₂ ⁻		Dithiophosphate
RCS ₃		Thioxanthate
RNCS ₂ ²⁻		Dithiocarbamate

1.3.1 Xanthate complexes

A lot of research has been done on different kinds of sulfur donor complexes, amongst them, xanthate complexes have received a lot of interest due to its two sulfur atoms. Related to the dithiocarbamates, the xanthates have an electronegative oxygen atom in its backbone structure. Like dithiocarbamates, xanthates are formed by reaction with carbon disulfide (CS_2). They find a lot of uses in industrial applications, the most common application is in the production of cellophane (Sellotape or scotch tape) and other related polymers from the reaction with cellulose and also in the mining industry for collection and flotation purposes (Rajput et al., 2012).

Most recently the xanthates and other 1,1-dithiolate compounds have been found to be most interesting compounds due to the presence of the two sulfur atoms. They have been used to make complexes. Singh and co-workers studied the mononuclear complexes of Cu^{I} with xanthate, dithiocarbamate, and phosphate ligands. Their study was facilitated by the most interesting features in the three ligands. They reported that although monoanionic xanthate and dithiocarbamate ligands have some common features, their coordination behavior differed significantly due to the dominant resonance structures they exhibit in their complexes. They reported that xanthates and phosphates reduce Cu^{II} to Cu^{I} , while the dithiocarbamates stabilized the +2 oxidation state in the complex (Singh et al., 2011). The xanthate complexes can then be used in the synthesis of metal sulfide nanoparticles. (Pradhan et al., 2003) they synthesized high-quality metal sulfide nanoparticles from alkyl xanthate as a precursor in alkyl amine solvents. Onwudiwe and co-workers used a laser-assisted solid state reaction to synthesize ZnS and CdS nanoparticles from metal xanthates. The photoluminescence findings were bizarre, in that they found a two-photon emission spectra of which they attributed to surface defects (trap states). The

TEM images of ZnS had aggregates with no crystal edges, while they obtained average particle size of 4.8 nm for the CdS nanoparticles (Onwudiwe et al., 2014).

1.3.2 Dithiophosphates

The exploration of the electron donors has lead researchers to investigate different materials with different chemistry. The dithiophosphates have been studied but less studied compared to other 1,1-dithiolate compounds such as metal xanthates and dithiocarbamates. This is because the phosphate moiety has a complex chemistry and complex ways of synthesizing such compounds. Their backbone also does not make it a versatile material. The dithiophosphates with the formula, $(RO)_2PS_2^-$ contain oxygen, carbon, phosphorus, and sulfur. The complexes formed from this compound depends on the metal center. In the main group metals, the most asymmetric type (aniso-bidentate) occurs when the covalent bond is associated with the secondary bond (Haiduc & Devillanova, 2007), while the symmetric type (iso-bidentate) is mostly found with transition metal complexes (Haiduc & Devillanova, 2007).

The use of the dithiophosphates as precursors to make metal sulfide nanoparticles has been less studied. Lou and co-workers (Lou, Chen, Wang & Weimin Liu, 2007b) made many studies on the use of dithiophosphates with different metals. Different shapes (rods, triangles and spheres) of nanoparticles were obtained with different metals (Cu, Bi, and Cd). The synthesis of monodispersed faceted and triangular CuS nanocrystals were made. In the synthesis of Bi_2S_3 and Sb_2S_3 , the rod-like shaped nanoparticles were obtained (Lou, Chen, Wang & Weimin Liu, 2007a). While the synthesis of CdS nanoparticles produced near spherical monodispersed nanoparticles (Lou, Chen, Wang & Weiming Liu, 2007).

1.3.3 Dithiocarbamates

Dithiocarbamates (DTC's) are relatively the most studied material across all fields when compared to all 1,1-dithiolate compounds mentioned in table 1, due to their versatility in molecular structure. The low spin – high spin crossover phenomena makes them a subject of interest in different fields. This phenomenon enables DTC's to stabilize high and low oxidation state metals, due to the backbone nitrogen atom which undergoes delocalization to form a thioureide resonant structure. The xanthates and dithiophosphates which do not form these resonant structure due to the backbone electronegative oxygen atom. Like the xanthates and the dithiophosphates, the DTC's also find use in the synthesis of nanoparticles. Their use in nanotechnology is also accompanied by their applications as metal complexes, which can be used to enhance the activity of the nanoparticles since they contains functional groups (sulfur and nitrogen) that confer enhanced activity in most biological applications. Dithiocarbamates gained a lot of credentials due to their strong coordinating capacity with various metal ions, which resulted in dithiocarbamates being widely used in several areas such as in industry, agriculture, medicine, and in analytical chemistry (Breviglieri et al., 1996). The thermolysis of the DTC metal complexes has proved to be a most interesting route for the synthesis of metal chalcogenide nanoparticles.

A lot of studies have been moderating different methods to synthesize nanoparticles, but in those methods, the metal sulfide source in most cases have been the DTC's. Dithiocarbamates have been used to synthesize high quality and well-dispersed particles. Ligand properties of the metal complexes used as precursor could be used in the modification of the size and shapes of nanoparticles (Onwudiwe & Ajibade, 2011). For example, as reported by Memon et al. (Memon et al., 2006) the variation of alkyl groups on the dithiocarbamate ligand was found to give a non-spherical morphology. The synthesis and characterization of metal sulfide nanoparticles / poly

(methyl methacrylate) nanocomposites has been reported by Ajibade (Ajibade & Mbese, 2014). The precursor used was ammonium aniline dithiocarbamates. They obtained small particles ranging from 4-20 nm. Nirmal et al. (Nirmal et al., 1994) did the synthesis of CdS nanocrystals using a cadmium salt with pyrrolidine dithiocarbamate as a single source precursor employing HDA as both the solvent and capping agent. They decomposed the precursor at 150°C using microwave irradiation and hexagonal shaped CdS nanoparticles were obtained. Mthethwa et al. (Mthethwa et al., 2009) reported the use of heterocyclic cadmium dithiocarbamate $[\text{Cd}(\text{S}_2\text{CNC}_9\text{H}_{10})_2]$ and $[\text{Cd}(\text{S}_2\text{CNC}_5\text{H}_{10})_2]$ and the preparation of anisotropic and isotropic HDA capped CdS nanoparticles by varying the capping agent concentration (3 g and 6 g) and temperature.

1.4 General introduction of nanotechnology

Nanotechnology is the understanding and control of matter at dimensions between ≈ 1 and 100 nanometers or it is the manipulation of atoms, molecules, and materials to form structures on the scale of nanometers (Haiduc & Devillanova, 2007; Kent & Riegel, 2012). These structures (nanoparticles) at this scale tend to exhibit unusually special properties due to quantum effects, as reported by Feynman (Feynman, 1960). He pointed out some potential quantum benefits from miniaturization. Nanotechnology is one of the most interdisciplinary technologies which promises a bright future in terms of challenges that we are facing. It brings glimpses of hope in fields like medicine for drug-resistant diseases, in engineering and many applications are envisaged in military use and in industries. Therefore knowledge in this field has been forever growing because

scientists are extensively studying and discovering novel applications in various fields. Nanotechnology encompasses the production and application of the physical, chemical, and biological systems at scales ranging from individual atoms or molecules to submicron dimensions, as well as the incorporation of the resulting nanostructures into larger systems (Bhushan, 2010).

An important part of nanotechnology before all these exhilarating applications is the synthesis and processing of the nanoparticles. The synthesis of uniform, high quality, and defect free nanoparticles is a major challenge in nanotechnology and scientists all over the world have devoted their energies and resources to finding the solution for this problem. Many methods have been employed in the synthesis of these nanoparticles. There are two types of approaches that are considered, called the ‘bottom up’ or the ‘top down’ approach. But the widely used and studied approach has been the bottom-up approach since it uses a chemical approach and can be modified to create specific particle shapes and sizes. To obtain those specific shapes and sizes, certain conditions have to be considered, viz. the parameters that affect the nucleation and growth of particles such as capping agent, capping concentration, temperature, time, pH, etc. Therefore several methods that cover the conditions and parameters mentioned above have been widely studied, methods such as the use of a single source precursor, colloidal, hydrothermal, sol-gel, etc. These methods have been solely explored for different kinds of nanoparticles; metal, metal chalcogenide semiconductor and other hybrid types of particles. In this study the single source precursor method was used to synthesize metal sulfide semiconductor nanoparticles.

Ligand properties of the metal complexes can be used in the modification of the size and shapes of nanoparticles (Onwudiwe & Ajibade, 2011). This is due to their strong chelating capabilities

with metal ions forming stable complexes which are then used to prepare nanoparticles (Coucovanis, 1979), (Coffey et al., 1993) and (Heard, 2005). Therefore in this study dithiocarbamates are used as precursors for the synthesis of nanoparticles.

1.4.1 Nanoparticle properties

The term ‘nano’ refers to the 10^{-9} m size regime and the term nanoparticle includes a material with at least one dimension ranging from 1-100 nm. This is the intermediate size range between the bulk and the molecular size, and at this size, particles exhibit unusual properties distinct from the bulk and molecule size. **Figure 1.3** below shows the nanoscale size of materials of common objects.

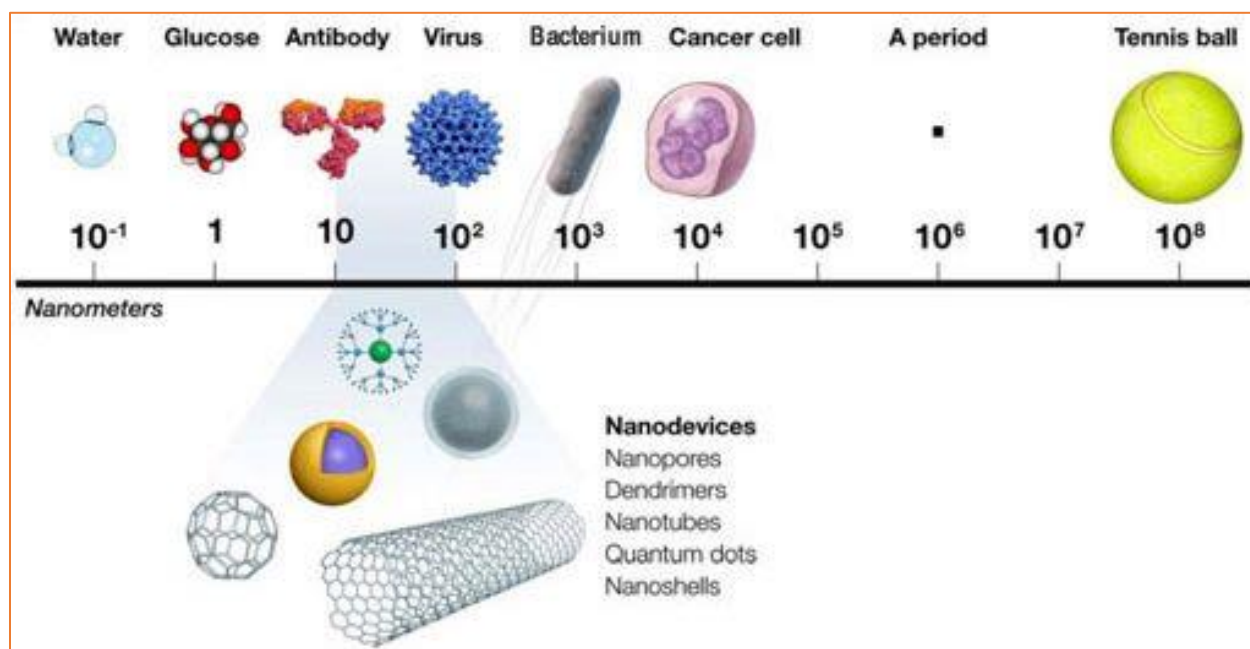


Figure 1.3: Nanometer-scale of comparison with common objects (Tyner, 2015).

There are two phenomena that are responsible for these unusual properties of nanoparticles: The first one is the high dispersity of the nanocrystalline system (“What makes nanoparticles different,” 2002), as the number of atoms at the surface of the crystal compared to the crystal itself, increases with the decrease in crystal size. Therefore, properties which are usually determined by the molecular structure of the bulk lattice, now become increasingly dominated by the defect structure of the surface (“What makes nanoparticles different,” 2002). It is then easier to imagine that this crystal will have a high surface to volume ratio which will, therefore, make the crystal have a higher chemical reactivity compared to its bulk counterpart. The second is said to be noticeable only in metals and semiconductors (“What makes nanoparticles different,” 2002). This phenomenon is known as size quantization which arises because the size of a nanoparticle is comparable to the de Broglie wavelength of its charge carrier (i.e. electrons and holes). This is all due to spatial confinement of the charge carriers, which thus make the edge of the valence band and conduction band split into discrete or quantized, electronic levels (Revaprasadu & Mlondo, 2006).

The quantum size effect is an important outcome of the nanometer size regime of particles. This was first observed by Faraday, who reported the red color of a colloidal gold solution (Faraday, 1857). This red color was due to a surface plasmon resonance (SPR), which is due to the interaction of light with the free charge carriers in the conduction band, which thus leads to the absorption profile of a nanoparticle being controlled by its size (Kelly et al., 2003). The quantum size effect is mainly observed in quantum dots (QD's) or semiconducting nanoparticles and relates the size of the nanoparticles to the size of the band gap, such that it increases with a decrease in size of the nanoparticles.

1.4.1.1 Semiconductor nanoparticles or quantum dots (QD's)

Semiconductor nanostructured materials have been extensively studied due to their unique properties that enable further development of novel properties different from the bulk counterparts (Itoh et al., 2006). Among the various nanocrystals, semiconducting metal chalcogenides are regarded as important nanomaterials as a result of their interesting properties, which are different from those of bulk substances (Hagfeldt & Graetzel, 1995). Semiconducting nanomaterials with all three dimensions in the range of 1-20 nm tend to have unique properties. These properties such as the electronic, magnetic, catalytic and optical properties are due to a large surface area obtained by reducing the size of the particles. As the diameter of the particles approaches the excitonic Bohr diameter, the charge carriers become confined in three dimensions with zero degrees of freedom (Landes et al., 2002) and (Zhang et al., 2003). As a result of the geometric constraints, the particle boundaries are then felt by the electron and it responds to particle size by adjusting its energy. The quantum size effect causes the continuous band of the solid to split into discrete, quantized levels and the band gap to increase (Revaprasadu & Mlondo, 2006).

The most conspicuous unique property of quantum dots (QDs) is that the absorption and emission can be tuned to any desired wavelength by simply changing their size (Ozin & Cademartiri, 2009). The structural size limits the exciton-Bohr radius of the bound electron-hole pairs, thus leading to altered electronic and optical properties (Franzl et al., 2007). This is due to the unique size and shape dependent optical properties which are totally different at the atomic/molecular level (Kailasa et al., 2013). A limited number of atoms may be present in each particle, due to their discrete energy levels in both the valence and conduction bands. Therefore, the absorbed energy should be greater than the band gap energy, so that electrons in the valence band can absorb energy and be excited and promoted to the conduction band, thus forming short-lived electron-hole pairs.

The bound state of the electron-hole pair is called an exciton (Brus, 1984). An exciton can be considered as analogous to a hydrogen atom, as it consists of a single positive and negative charge bound together. In quantum mechanics, a hole is assumed to behave as a particle (quasi-particle) with a certain effective mass and carries a positive charge. Therefore, an electron-hole recombination results with a photon emission of specific energy corresponding to the band gap, which is the band edge emission (Kailasa et al., 2013). Therefore, charge carriers adjust to higher kinetic energies, which thus leads to an increase in the band gap and the quantization of the energy levels to discrete levels. This whole phenomenon is called the quantum confinement effect. The schematic diagram below summarizes the difference between the molecule, quantum dot, and the bulk material. Since the nanomaterials are intermediate between the molecule and the bulk material they show quantized energy levels and the band gap is determined by the difference between the top of the valence band and the bottom of the conduction band (O'Farrell et al., 2006).

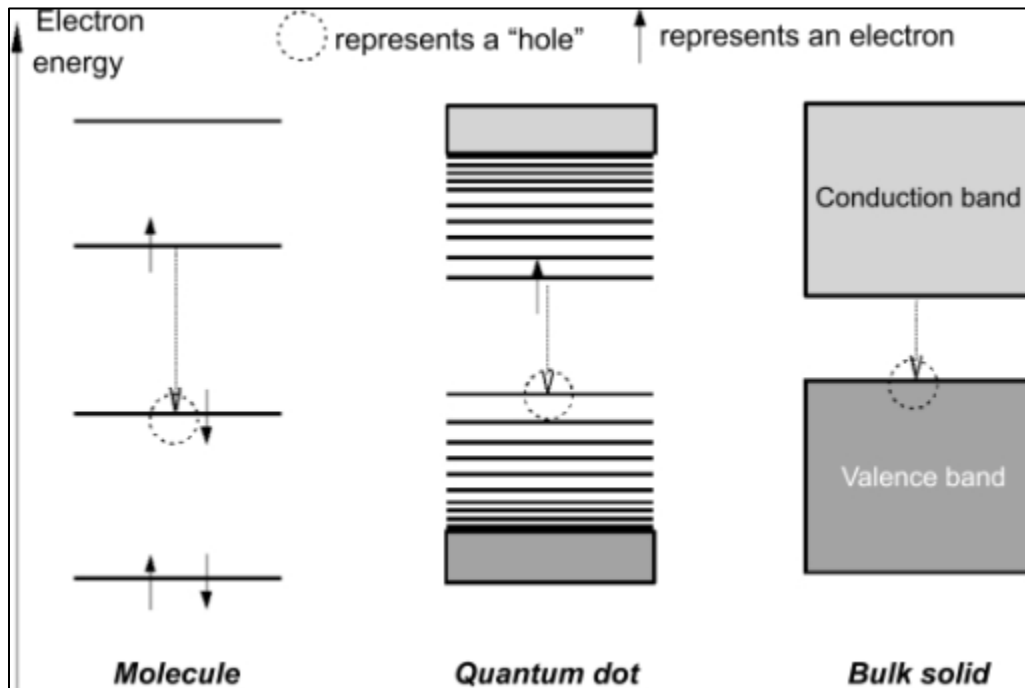


Figure 1.4: Schematic energy level structure of (left) molecular dye, (center) quantum dots, and (right) bulk semiconductor (O'Farrell et al., 2006).

The most studied semiconducting metal chalcogenides have been zinc sulfide and copper sulfide nanoparticles. Zinc sulfide has been studied due to its wide band gap energy of 3.60 eV (Kook et al., 2005). Copper sulfide has been widely studied due to its stoichiometric form, ranging from copper rich Cu_2S (Chalcocite) to copper poor CuS (Covellite). This variety in stoichiometries, results in copper sulfide use in many application in different fields of study. Copper chalcogenides have been studied because of their tunable near-infrared (NIR) plasmonic properties (Zhao et al., 2009), leading to their potential applications as alternatives to expensive noble metal nanoparticles. For example, in biomedicine they have been used in photothermal therapy or as biosensors and in many other applications. Cu_xS among the metal chalcogenide semiconductor nanomaterials has been reported to be a very attractive in biological applications. In comparison to cadmium-based II-VI semiconductors, copper based nanomaterials are preferred as they contain less a toxic metal (Metcalf et al., 1982).

1.4.1.1. (i). ZnS nanoparticles

Zinc sulfide (ZnS), is a direct band gap semiconductor with band gap energy of 3.60 eV, which makes it one of the most important materials in photonic research (Nyamen et al., 2014). It plays a vital role as a device material, which can be used for detectors, emitters, and modulators in optoelectronics (Kook et al., 2005), and in a blue light emitting laser diode (Kook et al., 2005). Many methods have been employed in the preparation of ZnS nanoparticles, methods such as thermal decomposition, hydrothermal/solvothermal, sol-gel, colloidal, and the single source

precursor method. The single source precursor method has been reported to be the most efficient route for the synthesis of high-quality metal chalcogenide nanoparticles (Pickett & O'Brien, 2001).

A dithiocarbamate approach has been widely studied in the synthesis of ZnS nanoparticles, Pickett and O'Brien synthesized high quality, defect free, monodispersed nanoparticles using bis(dialkyldithio-/diselenocarbamate) cadmium(II) and zinc(II) compounds as single source precursors for CdS/ZnS nanoparticles, and suggested that the precursor to nanoparticle deposition route is strongly influenced by the alkyl substituent groups present. they can, therefore, determine the phase and quality of the metal chalcogenide nanoparticles produced (Pickett & O'Brien, 2001). Nyameni et al. prepared almost spherical ZnS nanoparticles using heterocyclic piperidine and tetrahydroisoquinoline dithiocarbamates as the single source precursor for ZnS nanoparticles by varying the capping agents (HDA & TOPO) at different temperatures. When they passivated with HDA they produced elongated particles and in TOPO almost spherical particles were obtained (Nyameni et al., 2013). Ajibade and Osuntokun (Ajibade & Osuntokun, 2014) carried out the synthesis and characterization of hexadecylamine capped ZnS, CdS, and HgS nanoparticles using heteroleptic single molecular precursors. This produced ZnS nanoparticles in the hexagonal phase with particle sizes of 8–15 nm, while CdS nanoparticles were made in the cubic phase with the particle sizes in the range 4–7 nm and HgS nanoparticles was indexed to a face-centered cubic phase which had an average particle size of 7–12 nm.

1.4.1.1. (ii). CuS nanoparticles

Copper sulfide is a semiconductor with two types of band gaps depending on the stoichiometry of the quantum dots synthesized. These band gaps are classified as copper-poor and copper-rich

copper sulfide, which are also known as direct and indirect band gaps. Due to the flexibility of copper sulfide stoichiometries, Cu has attracted a wide attention in applications and lots of reports has been devoted to the synthesis of stoichiometric copper sulfide nanoparticles. These include covellite (CuS), djurleite (Cu_{1.98}S), digenite (Cu₉S₅), anilite (Cu₇S₄) and chalcocite (Cu₂S) this is especially due to the narrow band gap of nanocrystalline Cu_xS (1.2 – 2.3 eV) to allow for Cu generation of free charge carriers, thus resulting in direct and indirect band gaps (Zou et al., 2007). Cu_xS has been reported to be a very attractive material in biological applications among the metal chalcogenide semiconductor nanomaterials. In comparison to cadmium-based II-VI semiconductors, copper based nanomaterials are preferred as they contain a less toxic metal (Metcalf et al., 1982). The copper poor stoichiometric form has been found to be most interesting compared to the copper-rich form due to their absorption optical properties that are caused by the created holes (free carrier charges) in the valence band of the electron deficient copper sulfide form. The copper deficient form leads to an emergence of a near-IR band (Dorfs et al., 2011) and (Luther et al., 2011). The detailed information on the surface plasmon resonances will be discussed further in the section that follows. The plasmonic behavior of copper sulphide nanoparticles makes them very useful materials for applications in various fields such as photothermal ablation (Feng et al., 2015), bio-imaging (Cai & Chen, 2007), biosensors (Goel et al., 2014), solar cells (Singh et al., 2014), nanoscale switches (Jahan et al., 2015) and optical filters (Yu et al., 2007).

Different sulfur donors have been used in the synthesis of copper sulfide nanoparticles using different methods. Chen and co-workers synthesized novel copper sulfide hollow spheres that were generated from a copper (II)–thiourea complex. A reaction temperature increase gave much smaller hexagonal CuS nanoflakes that were generated from copper(II)–thiourea complex which

formed and they self-assembled into hollow spheres. Gorai et al. (Soma Gorai et al., 2005) produced flower-like Cu_2S dendrites via a solvothermal route using thiourea as a precursor. The growth of dendritic flower, stoichiometric copper sulfide was found to be depended on reaction time at a constant temperature of $130\text{ }^\circ\text{C}$. In another report a series of stoichiometric and non-stoichiometric copper sulfide was prepared via the solvothermal route using ethylenediamine–water as the solvent system at $130\text{ }^\circ\text{C}$ with thiourea as a molecular precursor. Dendritic or rod-like copper sulfide nanoparticles were obtained at elevated temperature and pressure. These conditions were used to break down the thiourea in the presence of ethylenediamine–water which also played an important role in determining the morphology and stoichiometry of copper sulfide (S. Gorai et al., 2005). Ajibade and Botha produced CuS nanoparticles from the synthesis and characterization of HDA-capped copper sulfide nanoparticles using copper(II)-N-phenyldithiocarbamate, copper(II)-N,N-ethylphenyldithiocarbamate and morpholine dithiocarbamate complexes as precursors (Ajibade & Botha, 2016). The TEM micrograph of nanoparticles synthesized from N-phenyldithiocarbamate showed a rod-like shape, N,N-ethylphenyldithiocarbamate gave a sphere-like morphology and morpholine-dithiocarbamate gave almost spherical particles. The plasmonic behavior of the copper chalcogenide particles was studied by other authors. Dorfs et al. (Dorfs et al., 2011) studied the reversible tunability of the near-infrared valence band plasmon resonance in Cu_{2-x}Se nanocrystals. The stoichiometry had an effect on the near-infrared peak. As the x-value in Cu_{2-x}Se decreased the near-infrared peak became more red-shifted. Hsu studied the localized surface plasmon resonances of anisotropic semiconductor nanocrystals. They demonstrated that anisotropic semiconductor nanocrystals (Cu_{2-x}S) displayed a localized surface plasmon resonances that was dependent on the nanocrystal shape and covered a broad spectral region in the near-IR wavelength (Hsu et al., 2011).

The literature has shown that different precursors and methods give different morphologies and stoichiometries. It has also been revealed that stoichiometric Cu_{2-x}S shows an interesting phenomenon (surface plasmon resonance) that in past years was only possible for noble metal particles. The plasmonic behavior of copper sulfide will be discussed in detail in the following section.

1.4.1.2 Surface plasmon resonance (SPR)

Localized surface plasmon resonance (LSPR) is a collective oscillation of free carriers (electrons) in the conduction band in resonance with incident light (Luther et al., 2011); (Chen et al., 2015). These electrons thus cause a charge separation with respect to the ionic lattice upon their oscillation around the particle surface, forming a dipole oscillation along a direction of the electric field of the light (Huang & El-sayed, 2010). It is only called a localized surface plasmon resonance when the amplitude of oscillation reaches a maximum at a specific frequency. The LSPRs were only known to occur on metals, but now due to the low carrier density of semiconductors (10^{21} cm^{-3}) relative to metals (10^{23} cm^{-3}), the LSPR has also been observed on semiconductors due to the appreciable carrier densities. For these reasons, semiconductors exhibit LSPR responses in the near-infrared (NIR) and mid-infrared (MIR) regions (Xie et al., 2013) & (Luther et al., 2011). This relation is understood from the Drude model in equation 1.

$$\omega_p = \sqrt{\frac{N_h e^2}{\epsilon_0 m_h}} \dots\dots\dots \mathbf{1}$$

Where ω_p is the bulk plasma frequency, N_h is the density of free carriers, e is the electron charge, ϵ_0 is the dielectric constant of vacuum and m_h is the hole effective mass.

LSPRs have been extensively studied but most studies have been related to noble metal nanoparticles that possess different sizes and shapes. These noble metallic nanoplasmonic studies have been immense in the last few decades due to their ability to alter light-matter interactions and their potential applications in enhanced spectroscopies (Kneipp et al., 1997) & (Fauchaux et al., 2014), sensing (Larsson et al., 2009), photocatalysis (Fan et al., 2016), imaging and optical devices. These applications are mainly due to the enhanced radiative and non-radiative properties of the nanoparticles thus offering multiple modalities for biological and medical applications (Huang & El-sayed, 2010). Among the doped semiconducting nanoparticles, the p-type semiconductor nanoparticles are mainly effective type in semiconductors that show LSPRs and specifically the copper chalcogenide nanoparticles (Kriegel et al., 2012). The copper chalcogenide nanoparticle LSPR is mainly affected by the stoichiometric form. In particular, copper sulfide nanoparticles, as reported by Luther et al. (Luther et al., 2011), showed that the copper rich phase chalcocite (Cu_2S) form do not support the plasmon resonances, while its copper deficient non-stoichiometric form ($Cu_{2-x}S$, $x > 0$) does develop an extinction band in the NIR region. Copper sulfide gives rise to hole carrier concentrations that are capable of sustaining an LSPR in the near infrared (NIR) region, due to its ability to support multiple copper deficient stoichiometries that are naturally p-doped (Fauchaux et al., 2014). The semiconductor nanoplasmonics have a superior property compared to a metal plasmon, including tunability which is only offered by

semiconductors, that is, through the change in the free carrier concentration, as described by Drude model in equation 1.1. The lack of tunability in metals is due to the large carrier density of (10^{23}cm^{-3}) which are difficult to change. Small shifts of LSPRs in the visible region which were said to originate from the charging/discharging of metal particles have been reported by (Novo et al., 2008) & (Hirakawa & Kamat, 2005). In contrast, electron doping has allowed semiconductor nanoparticles to have smaller carrier densities varying from 10^{16}cm^{-3} to 10^{21}cm^{-3} (Xie et al., 2013).

1.5 Nanoparticle synthesis methods

There have been several reported methods reported for the synthesis of well-dispersed nanoparticles. There are two approaches to the synthesis of nanoparticles and they are commonly known as the ‘top-down’ and the ‘bottom-up’ approach. The top-down approach involves the production of nanomaterials from the size reduction of bulk material. The examples of the top-down approach include mechanochemical processing, inert gas evaporation, high-energy milling, and sputtering amongst others. These types of approach use lithographic patterning techniques for the fabrication of nanomaterials. The bottom-up approach is more of a chemical approach in the sense that nanomaterials are built from molecular structures (atoms, molecules) and these structures assemble themselves chemically by principles of molecular recognition. Examples of bottom-up approaches include sol-gel methods, hydro/solvothermal methods, chemical vapor deposition (CVD), precipitation methods and precursor decomposition methods/single-source precursor methods which are the focus of this dissertation.

The most commonly used approach in the above-mentioned two approaches has been the bottom-up approach. It is favored due to the ease control of size, shape, and manipulation of nanoparticles.

It is a chemical route approach. Like every approach some of the methods used in the bottom-up approach suffer from drawbacks, methods such as colloidal, chemical vapor deposition and molecular epitaxy methods have limitations as they produce particles that are aggregated or attached to each other, thereby limiting their potential applications. In the mentioned methods the colloidal methods do produce agglomerated particles but its advantage over chemical vapor deposition and other mentioned methods is its use of a green chemical approach in the synthesis of nanomaterials. They, therefore, find use in biochemical applications.

1.5.1 Colloidal method

The colloidal method was the first reported method that was used to synthesize small particles and involves a controlled precipitation reaction in a homogeneous solution. La Mer and Dinegar showed the critical step of achieving narrowly dispersed particles (LaMer & Dinegar, 1950). That fundamental step is the separation of the nucleation and growth processes. The highly monodispersed particles are obtained if nucleation and growth process are evidently separated from one another (fast nucleation and slow growth). This separation thus give rise to the process known as Ostwald ripening, the process, which promotes the dissolution of nanocrystals which are less stable and then recrystallization on larger ones, that are more stable.

The colloidal method has gained a lot of interest recently due to its use of eco-friendly chemicals (amino acids, sugars, low temperatures and less toxic solvent) for the synthesis of nanomaterials. The produced colloidal particles under such conditions are water soluble, which makes them biocompatible for biological systems (biological imaging, drug deliverance, and much more). The colloidal method uses green materials but its disadvantage is that it cannot be employed to easily synthesize some types of semiconductors like CdSe, GaAs, InP, and InAs. The instability of

colloids at high temperatures makes annealing of the particles difficult, which leads to poor crystalline materials being formed.

Dutta and Dolui (Dutta & Dolui, 2008) prepared colloidal dispersions of CuS nanoparticles stabilized by sodium dodecyl sulphate (SDS). The average size of the particles was found to be about 76 nm. The optimum conditions produced spherical shaped particles. While colloidal copper(I) sulfide nanorods were obtained by (Kruszynska et al., 2012). Gayou and co-workers (Gayou et al., 2010) synthesized colloidal uncapped ZnS agglomerates that showed almost hexagonal shape by HRTEM studies (Gayou et al., 2010). While Rahdar et al. produced colloidal ZnS particles of different sizes using mercaptoethanol as capping agent (Rahdar et al., 2012).

1.5.2 Hydro/Solvothermal method

Solvothermal synthesis is a process of transforming reactants or precursors in solution medium and in a closed system usually a stainless steel autoclave which is heated to a certain temperature and high pressure for a particular time. In this method, the reaction temperature is higher than the boiling point of the solvent. It is called hydrothermal when water is used in the synthesis. In hydrothermal the synthesis is usually undertaken at a temperature below the supercritical temperature of water (340°C). The drawback of this synthetic route is the prolonged time of synthesis that ranges between 1 h to 30 days, inability to control the morphology of the nanoparticles; (products which can be amorphous, crystalline solid, nanorods and flower-like) (Huang et al., 2008). Gorai et al (Soma Gorai et al., 2005) used the solvothermal route to synthesize flower-like dendrite Cu₂S particles. Hoa et al. (Hoa et al., 2009) then synthesized novel CuS with a hierarchical structure at 200°C for 12 h using the solvothermal route. The ZnS nanoparticles had an almost spherical shape and were synthesized using a hydrothermal route,

while spherical particles with a small degree of aggregation were synthesized *via* a hydrothermal method assisted by a microemulsion technique. The reaction temperature was at 160°C for 12 h (Liu et al., 2009).

1.5.3 Single-source precursor method

The use of single-molecule precursors whereby the metal-chalcogenide bond is available has proven to be a very efficient route to the synthesis of high-quality nanoparticles. This method serves as an alternative that is more effective to the problems that are encountered in the colloidal route. The method was first used by Murray et al. (Murray et al., 1993) by injecting a volatile metal alkyl (dimethylcadmium) and a chalcogenide source TOPSe (tri-n-octylphosphine selenide mixed in tri-n-octylphosphine (TOP)) into hot TOPO (tri-n-octylphosphine oxide), a polar coordinating Lewis base solvent. This method gave rise to well dispersed, defect free and high-quality nanoparticles (Murray et al., 1993). Some of the examples of the high quality, monodisperse crystalline nanoparticles that were prepared by this route include CdSe, CdS, and CdTe.

Although the method proved to be satisfactory for the synthesis of highly monodispersed nanoparticles, the most concerning issue above all, was the use of hazardous chemicals (dimethylcadmium) that was used to synthesize the nanoparticles. To avoid the use of toxic chemicals the method known as single source precursors was used. A single source precursor means that a single compound with all elements required to produce a metal chalcogenide nanocrystal available in one molecule. This type of method have a lot of advantages in comparison to other methods, these advantages include;

- (I) Avoiding the use of toxic, volatile and pyrophoric precursors.
- (II) Low-temperature deposition routes are possible.

- (III) Some nanoparticles are air sensitive. The precursors for those are synthesized under both aerobic and anaerobic conditions, with its resulting precursor being air and moisture stable.
- (IV) The use of one involatile precursor minimize the chance of incorporating impurities into nanoparticles.

Originally, single-molecular precursors were used in the preparation of semiconductor thin films by CVD techniques, but this method has proved problematic because of the low volatility of the precursors and lack of stoichiometric control of the resultant materials. Trindade and O'Brien first reported the use of bis(dialkyldithio/seleno-carbamato)cadmium(II)/zinc(II) complexes for the synthesis of zinc and cadmium sulfide selenium nanoparticles. Bis(dialkyldithio/seleno-carbamato)cadmium(II)/zinc(II) complexes were thermolysed in TOPO or in 4-ethylpyridine to prepare MS and MSe nanoparticles (M = Cd, Zn)(Trindade & Brien, 1996). In this route, the decomposition of the precursor is an essential condition for the formation of nanoparticles and growth is terminated when the precursor is exhausted. The initial rapid nucleation at the beginning of the injection introduces a controlled growth of the nuclei. When the growth of nanoparticles reaches the expected size, further growth is terminated by a sudden cooling of the solution. The product which in this case is the nanoparticles is separated on addition of a solvent which can precipitate it; this solvent should be miscible with the nanoparticles and immiscible with the capping agent preventing aggregation that is due to flocculation.

1.6 Potential applications of nanoparticles

Nanotechnology is a fascinating field of science with lots of possibilities in wide fields. The size, morphology, and composition are the dependent variables for better future applications which still have the problems, but a lot of research is being done to overcome this particular problem. The size and morphology make these nanoparticles very special and superior to its bulk counterparts. At the nanoscale they exhibit interesting and unusual properties such as higher luminescence, electronic, optical, magnetic and catalytic properties. These properties are achieved by a phenomenon known as quantum size confinement. Using this phenomenon novelty applications could be engineered in industries for a wide range of applications, smaller medicines which can be of great importance, can be manufactured for diseases that have no cure, such as cancer which is an imminent threat to our everyday lives. In biological application it can open up possibilities of *in vivo* applications, were nanoparticles could be directed to the specific disease site.

1.6.1 Biological applications

The synthesis of metal chalcogenide nanoparticles brings about a lot of possibilities of applications in materials, devices, and human species. These nanoparticles can be used in biological applications as antimicrobial agents (CuS nanoparticles) in the intensively studied gram positive and gram negative bacterial. They have also been studied in photothermal therapy in hybrid form with gold nanoparticles as an alternative for photodynamic therapy. They have also investigated future applications e.g. *in vivo* for their luminescence properties for biological cellular imaging. CuS has been suggested as suitable for use in optical sensors and human eye protection devices because of its optical limiting property. ZnS nanoparticles have been used in probing of DNA structure.

Quantum dots have a variety of applications; some of them like CuS nanoparticles can be applied in biological labeling or biological imaging with *in vivo* technique, especially in cancer applications where lot of attention is currently devoted. Many people are diagnosed with cancer which comes from different unknown sources of our surroundings from the environment. These quantum dots have the ability to fluoresce at multiple wavelengths spanning the visible spectrum, due to their spectral band gaps (Feng et al., 2015). Due to their unique luminescent properties, many-color probes can be simultaneously excited by a single narrow-band excitation source and distinguished in a single exposure. This makes semiconductor nanocrystals (QDs) superior to commonly used organic chromophores. QDs have been considered as the best tools for intracellular studies such as visualizing cellular structures, studying the dynamics of cellular processes, and tracking single molecules in the cell. When incorporated into polymers the ligand surrounding on the quantum dots can be tailored to target specific cancer lines.

1.6.2 Solar cells

There is a growing need for sustainable energy. This demand is a challenge that is faced globally. Renewable energy is a problem that the world is currently facing. The solution or rather positive response to the problem is the use of the sun as a source of energy. The energy that the sun radiates in one hour is more than the energy that the earth uses in one year (Kiehl & Trenberth, 1997). Therefore the need to harness the energy from the sun is of great importance. The use of nanotechnology can significantly improve the efficiency of the absorber layers of the solar cell because nanoparticles have a high surface to volume ratio for enhancement of the absorber layers, and this would improve the enhancement of the conversion efficiency. Photovoltaic or solar cells are used to harness the solar radiation and they directly convert the energy to electrical power.

The use of nanotechnology in solar cells to create “smart energy” is fast becoming important due to its benefits that include;

- Low carbon emission
- The energy is replenished at a faster rate than it is consumed
- The energy is derived from natural processes that are free of pollution derived from fossil fuels

Plasmonic nanoparticles are the ideal type of particles because they can form multiple resonances in the visible region, which can be used to trap more light thus increasing efficiency. This is ideal because we only get a certain percentage of the sun radiation, with other percentage being reflective.

1.7 Aims and objectives

Aim:

To synthesize and characterize dithiocarbamate ligands, and their Zn and Cu complexes and their metal chalcogenide (Cu_xS_y and ZnS) nanoparticles

Objectives:

- (i) To synthesize and characterize dithiocarbamate ligands based on cyclohexylamine, aniline and pyrrolidine. The prepared ligands are to be characterized by Fourier transform infrared (FTIR) spectroscopy, and nuclear magnetic resonance (NMR) spectroscopy
- (ii) To synthesize and characterize Cu and Zn complexes of the prepared dithiocarbamate ligands. They are to be characterized by thermogravimetric analysis (TGA), and FTIR and NMR spectroscopy.

- (iii) To synthesize and characterize CuS and/or ZnS nanoparticles by varying amount/concentration of capping agents (3 g and 6 g see appendix for ratios). The resulting nanoparticles are to be characterized by ultraviolet-visible spectrophotometry (UV-vis), photoluminescence (PL), X-ray diffraction (XRD), and transmission electron microscopy (TEM).
- (iv) To investigate the effect of the capping agents hexadecylamine (HDA) and tri-octyl-n-phosphine oxide (TOPO) on the size and shape of the nanoparticles.

1.8 References

- EL A'MMA, A.G. & DRAGO, R.S.. 1977. Unusual Oxidation-State Stabilization of Iron Complexes by the Pyrrole-N-carbodithioate Ligand. *Inorg. Chem.* **16** (11) pp. 2975–2977.
- AJIBADE, P.A. & BOTHA, N.L.. 2016. Synthesis and structural studies of copper sulfide nanocrystals. *Results Phys.* **6** pp. 581–589.
- AJIBADE, P.A. & MBESE, J.Z.. 2014. Synthesis and Characterization of Metal Sulfides Nanoparticles / Poly (methyl methacrylate) Nanocomposites. *Int. J. Polym. Sci.* **2014** pp. 1–8.
- AJIBADE, P.A. & OSUNTOKUN, J.. 2014. Synthesis and Characterization of Hexadecylamine Capped ZnS , CdS , and HgS Nanoparticles Using Heteroleptic Single Molecular Precursors. *J. Nanomater.* **2014** pp. 1–7.
- ANDERSON, W.P. & BAIRD, D.M.. 1988. Comparative Study of the Electronic Structures of N,N'-Diethyldithiocarbamate and Pyrrole-N-carbodithioate and Their Nickel(II) Complexes. *Inorg. Chem.* **27** (18) pp. 3240–3242.

- BAIRD, D.M., FANWICK, P.E. & BARWICK, T.O.M.. 1985. Preparations and Structures of cis -
[Mo₂(S₂CNC₄H₄)₂(O₂CCH₃)₂OPPh₃] and [Mo₂(S₂PEt₃)(O₂CCH₃)₂OPEt₃](BF₄): Two
Quadruply Bonded Dimers Involving Dithio Acid Ligands. *Inorg. Chem.* **24** (8) pp. 3753–
3758.
- BEREMAN, R.D., BAIRD, D.M., VANCE, C.T., HUTCHINSON, J. & ZUBIETA, J.. 1983. Coordination
chemistry of new sulfur-containing ligands. 25. Reduction and deoxygenation of MoO₃⁺(aq)
by pyrrole-N-carbodithioate (L) to yield eight-coordinate MoL₄: crystal and molecular
structure of tetrakis(pyrrole-N-carbodithioato)molybdenum-hemi(meth. *Inorg. Chem.* **22**
(16) pp. 2316–2318.
- BEREMAN, R.D., CHURCHILL, M.R. & SHIELDS, G.. 1979. Coordination Chemistry of Sulfur-
Containing Ligands. *Inorg. Chem.* **18** (11) pp. 3117–3121.
- BEREMAN, R.D. & NALEWAJEK, D.. 1978. Oxovanadium(IV) complexes of the dithiocarbamate
ligands derived from indole, indoline, carbazole and pyrrole. *J. Inorg. Nucl. Chem.* **40** (7)
pp. 1313–1316.
- BEREMAN, R.D. & NALEWAJEK, D.. 1977. Preparation and Characterization of Pyrrole-N-
carbodithioate Complexes of Selected Transition Elements. *Inorg. Chem.* **16** (11) p. 2687.
- BEREMAN, R.D. & NALEWAJEK, D.. 1978. Preparation of Dithiocarbamate ligand derived from
Indole, Carbazole, and Imidazole and representative transition-element complexes. *Inorg.*
Chem. **17** (4) p. 1085.
- BHUSHAN, B.. 2010. Introduction to nanotechnology. In *Springer Handbook of Nanotechnology*.
Springer Berlin Heidelberg, pp. 1–13.

- BREVIOLIERI, S.T., CAVALHEIRO, E.T.G. & CHIERICET, G.O.. 1996. STUDIES OF Fe (III) BEHAVIOUR IN THE PRESENCE OF BIS (2-HYDROXYETHYL) DITHIOCARBAMATE. *Polyhedron* **15** (5–6) pp. 839–843.
- BRUS, L.E.. 1984. Electron–electron and electron-hole interactions in small semiconductor crystallites: The size dependence of the lowest excited electronic state. *J. Chem. Phys.* **80** (9) p. 4403.
- CAI, W. & CHEN, X.. 2007. Nanoplatfoms for targeted molecular imaging in living subjects. *Small Rev.* **3** (11) pp. 1840–1854.
- CARDELL, D., HOGARTH, G. & FAULKNER, S.. 2006. A dithiocarbamate-stabilized copper(I) cube. *Inorganica Chim. Acta* **359** (4) pp. 1321–1324.
- CHEN, L., SAKAMOTO, M., SATO, R. & TERANISHI, T.. 2015. Determination of a localized surface plasmon resonance mode of Cu 7 S 4 nanodisks by plasmon coupling. *Faraday Discuss.* **0** pp. 1–10.
- COFFEY, T.A., FORSTER, G.D. & HOGARTH, G.. 1993. Double Sulfur-Carbon Bond Cleavage of a Dithiocarbamate Ligand at a Molybdenum(VI) Centre; Synthesis and X-Ray Structure of the Disulfur Complex [Mo(NPh)(S₂)(edtc)₂] (edtc = S₂CNEt₂). *J. Chem. Soc. Commun.* **511** (3) pp. 1524–1525.
- COTTON, F.A., WILKINSON, G., MURILLO, C. A. & BOCHMANN, M.. 1996. Advanced Inorganic Chemistry: Sixth Edition. *John Wiley Sons, Inc, New York* pp. 1–1376.
- COUCOUVANIS, D.. 1979. *The Chemistry of the Dithioacid and 1. 1.Dithiolate Complexes. 1968-1977.* LIPPARD, S. J., ED. John Wiley & Sons, Inc.

- DORFS, D., HÄRTLING, T., MISZTA, K., BIGALL, N.C., KIM, M.R., GENOVESE, A., FALQUI, A., POVIA, M. & MANNA, L.. 2011. Reversible tunability of the near-infrared valence band plasmon resonance in Cu_{2-x}Se nanocrystals. *J. Am. Chem. Soc.* **133** (29) pp. 11175–11180.
- DUTTA, A. & DOLUI, S.K.. 2008. Preparation of colloidal dispersion of CuS nanoparticles stabilized by SDS. *Mater. Chem. Phys.* **112** (2) pp. 448–452.
- FAN, W., LEUNG, M.K.H., YU, J.C. & HO, W.K.. 2016. Recent development of plasmonic resonance-based photocatalysis and photovoltaics for solar utilization. *Mol. Rev.* **21** (180) pp. 1–26.
- FARADAY, M.. 1857. The Bakerian lecture: experimental relations of gold (and other metals) to light. *Phil. Trans. R. Soc. Lond.* **147** (0) pp. 145–181.
- FAUCHEAUX, J.A., STANTON, A.L.D. & JAIN, P.K.. 2014. Plasmon Resonances of Semiconductor Nanocrystals: Physical Principles and New Opportunities. *J. Phys. Chem. Lett.* **5** (6) pp. 976–985.
- FENG, W., NIE, W., CHENG, Y., ZHOU, X., CHEN, L., QIU, K., CHEN, Z., ZHU, M. & HE, C.. 2015. In vitro and in vivo toxicity studies of copper sulfide nanoplates for potential photothermal applications. *Nanomedicine Nanotechnology, Biol. Med.* **11** (4) p. 901-912.
- FEYNMAN, R.P.. 1960. There's plenty of room at the bottom. *Eng. Sci.* **23** (5) pp. 22–36.
- FRANZL, T., MULLER, J., KLAR, T. A., ROGACH, A.L., FELDMANN, J., TALAPIN, D. V. & WELLER, H.. 2007. CdSe:Te nanocrystals: Band-edge versus Te-related emission. *J. Phys. Chem. C* **111** (7) pp. 2974–2979.
- GALINDO, A., MIGUEL, D. & PEREZ, J.. 1999. Phosphine-carbon disulfide adducts, S₂CPR₃:

- Versatile ligands in coordination chemistry. *Coord. Chem. Rev.* **193–195** pp. 643–690.
- GAYOU, V.L., SALAZAR HERNÁNDEZ, B., DELGADO MACUIL, R., ZAVALA, G., SANTIAGO, P. & OLIVA, A. I. 2010. Structural Studies of ZnS Nanoparticles by High Resolution Transmission Electron Microscopy. *J. Nano Res.* **9** (2010) pp. 125–132.
- GOEL, S., CHEN, F. & CAI, W.. 2014. Synthesis and biomedical applications of copper sulfide nanoparticles: from sensors to theranostics. *Small* **10** (4) pp. 631–45.
- GORAI, S., GANGULI, D. & CHAUDHURI, S.. 2005. Shape selective solvothermal synthesis of copper sulphides: Role of ethylenediamine-water solvent system. *Mater. Sci. Eng. B Solid-State Mater. Adv. Technol.* **116** (2) pp. 221–225.
- GORAI, S., GANGULI, D. & CHAUDHURI, S.. 2005. Synthesis of flower-like Cu₂S dendrites via solvothermal route. *Mater. Lett.* **59** (7) pp. 826–828.
- HAGFELDT, A. & GRAETZEL, M.. 1995. Light-Induced Redox Reactions in Nanocrystalline Systems. *Chem. Rev.* **95** (1) pp. 49–68.
- H Aiduc, I. & Devillanova, F.. 2007. *Handbook of chalcogen chemistry*. Devillanova, F. A., ED. Cambridge CB4 0WF, UK: RSC Publishing.
- HEARD, P.J.. 2005. Main Group Dithiocarbamate Complexes. In KARLIN, K. D., ED. *Progress in Inorganic Chemistry, Volume 53*. London UK, WC1E 7HX: 2005 John Wiley & Sons, Inc.
- HERRICK, R.S., BURGMAYER, S.J.N. & TEMPLETON, J.L.. 1983. Complexes Containing the Electronically Unique Pyrrole-N-carbodithioate Ligand. *Inorg. Chem.* **22** (1) pp. 3275–3281.
- HERRICK, R.S. & TEMPLETON, J.L.. 1986. Syntheses, spectral properties and substitution

- reactions of $M(\text{CO})_3(\text{S}_2\text{CNC}_4\text{H}_4)_2$ ($M = \text{Mo}, \text{W}$) complexes containing the electronically unique pyrrole-N-carbodithioate ligand. *Inorg. Chem.* **25** (8) pp. 1270–1276.
- HIRAKAWA, T. & KAMAT, P. V.. 2005. Charge separation and catalytic activity of Ag@TiO₂ core-shell composite clusters under UV-irradiation. *J. Am. Chem. Soc.* **127** (11) pp. 3928–3934.
- HOA, T.T.Q., VU, L. VAN, CANH, T.D. & LONG, N.N.. 2009. Preparation of ZnS nanoparticles by hydrothermal method. In *Journal of Physics: Conference Series*. 2009 IOP Publishing Ltd, p. 12081.
- HOGARTH, G.. 2012. Metal-dithiocarbamate complexes: chemistry and biological activity. *Mini Rev. Med. Chem.* **12** (12) pp. 1202–15.
- HOGARTH, G.. 2005. Transition Metal Dithiocarbamates: 1978-2003. In KARLIN, K. D., ED. *Progress in Inorganic Chemistry, Volume 53*. London, UK: 2005 John Wiley & Sons, Inc, pp. 1978–2003.
- HSU, S.-W., ON, K. & TAO, A.R.. 2011. Localized surface plasmon resonances of anisotropic semiconductor nanocrystals. *J. Am. Chem. Soc.* **133** (47) pp. 19072–5.
- HUANG, W., XU, Z., LIU, R., YE, X. & ZHENG, Y.. 2008. Tungstenic acid induced assembly of hierarchical flower-like MoS₂ spheres. *Mater. Res. Bull.* **43** (10) pp. 2799–2805.
- HUANG, X. & EL-SAYED, M.A.. 2010. Gold nanoparticles : Optical properties and implementations in cancer diagnosis and photothermal therapy. *J. Adv. Res.* **1** pp. 13–28.
- ITOH, K., KUZUYA, T. & SUMIYAMA, K.. 2006. Morphology and Composition-Controls of Cu_xS Nanocrystals Using Alkyl-Amine Ligands. *Mater. Trans.* **47** (8) pp. 1953–1956.

IVANOV, A. V, KRITIKOS, M., ANTZUTKIN, O.N. & FÖRSLING, W.. 2001. The structural reorganisation of bis (diethyldithiocarbamate) morpholine – zinc (II) and – copper (II) in the course of solid-state solvation with morpholine and benzene molecules studied by ESR , solid-state ^{13}C and ^{15}N CP / MAS NMR spectroscopy. *Inorganica Chim. Acta* **321** pp. 63–74.

JAHAN, S., LITON, M.N.H., KHAN, M.K.R. & RAHMAN, M.M.. 2015. EFFECT OF ALUMINUM DOPING ON THE PROPERTIES OF SPRAY DEPOSITED COPPER SULFIDE (Cu_2S) THIN FILMS. *Int. J. Adv. Eng. Technol.* **6** (1) pp. 1–6.

KAILASA, S.K., CHENG, K.H. & WU, H.F.. 2013. Semiconductor nanomaterials-based fluorescence spectroscopic and matrix-assisted laser desorption/ionization (MALDI) mass spectrometric approaches to proteome analysis. *Materials (Basel)*. **6** (12) pp. 5763–5795.

KELLNER, R., PROKOPOWSKI, P. & MALLISA, H.. 1974. Beitrag zum problem der bandenverschiebung in den ir-spektren von dialkyldithiocarbamidaten: Teil III. Pyrroldithiocarboxylate. der bereich von $4000\text{--}300\text{ cm}^{-1}$. *Anal. Chem. Acta* **68** pp. 401–406.

KELLY, K.L., CORONADO, E., ZHAO, L.L. & SCHATZ, G.C.. 2003. The Optical Properties of Metal Nanoparticles: The Influence of Size, Shape, and Dielectric Environment. *J. Phys. Chem. B* **107** (3) pp. 668–677.

KENT, J.A. & RIEGEL. 2012. HAND BOOK OF INDUSTRIAL CHEMISTRY AND BIOTECHNOLOGY. 11TH ED. KENT, J. A., ED. MORGANTOWN, WEST VIRGINIA, USA: © 2007 SPRINGER SCIENCE+BUSINESS MEDIA, LLC.

- KIEHL, J.T. & TRENBERTH, K.E.. 1997. Earth's Annual Global Mean Energy Budget. *Bull. Am. Meteorol. Soc.* **78** (2) pp. 197–208.
- KNEIPP, K., WANG, Y., KNEIPP, H., PERELMAN, L.T., ITZKAN, I., DASARI, R.R. & FELD, M.S.. 1997. Single molecule detection using surface-enhanced Raman scattering (SERS). *Phys. Rev. Lett.* **78** (9) pp. 1667–1670.
- KNIGHT, E.R., COWLEY, A.R., HOGARTH, G. & WILTON-ELY, J.D.E.T.. 2009. Bifunctional dithiocarbamates: a bridge between coordination chemistry and nanoscale materials. *Dalton Trans.* **9226** (4) pp. 607–609.
- KOOK, W.S., SEOK, H.Y., SEUNG, S.L. & SHIM, I.W.. 2005. Preparation of ZnS thin film using Zn(dithiocarbamate)₂ precursors by MOCVD method. *Bull. Korean Chem. Soc.* **26** (10) pp. 1582–1584.
- KRIEGEL, I., JIANG, C., RODRÍGUEZ-FERNÁNDEZ, J., SCHALLER, R.D., TALAPIN, D. V., DA COMO, E. & FELDMANN, J.. 2012. Tuning the excitonic and plasmonic properties of copper chalcogenide nanocrystals. *J. Am. Chem. Soc.* **134** (3) pp. 1583–1590.
- KRUSZYNSKA, M., BORCHERT, H., BACHMATIUK, A., RÜMMELI, M.H., BUECHNER, B., PARISI, J. & KOLNY-OLESIK, J.. 2012. Size and Shape Control of Colloidal Copper (I) Sulfide Nanorods. *ACS Nano* **6** (7) p. A-H.
- LAMER, V. & DINEGAR, R.. 1950. Theory, production and mechanism of formation of monodispersed hydrosols. *J. Am. Chem. Soc.* **72** (11) pp. 4847–4854.
- LANDES, C.F., LINK, S., MOHAMED, M.B., NIKOBAKHT, B. & EL-SAYED, M. A.. 2002. Some properties of spherical and rod-shaped semiconductor and metal nanocrystals. *Pure Appl.*

- Chem.* **74** (9) pp. 1675–1692.
- LARSSON, E.M., LANGHAMMER, C., ZORIĆ, I. & KASEMO, B.. 2009. Nanoplasmonic probes of catalytic reactions. *Science* **326** (2009) pp. 1091–1094.
- LIU, J., MA, J., LIU, Y., SONG, Z., SUN, Y., FANG, J. & LIU, Z.. 2009. Synthesis of ZnS nanoparticles via hydrothermal process assisted by microemulsion technique. *J. Alloys Compd.* **486** (1–2) pp. 40–43.
- LOU, W., CHEN, M., WANG, X. & LIU, W.. 2007a. Novel single-source precursors approach to prepare highly uniform Bi₂S₃ and Sb₂S₃ nanorods via a solvothermal treatment. *Chem. Mater.* **19** (4) pp. 872–878.
- LOU, W., CHEN, M., WANG, X. & LIU, W.. 2007b. Size control of monodisperse copper sulfide faceted nanocrystals and triangular nanoplates. *J. Phys. Chem. C* **111** (27) pp. 9658–9663.
- LOU, W., CHEN, M., WANG, X. & LIU, W.. 2007. Synthesis of high-luminescent cadmium sulfide nanocrystallites by a novel single-source precursor route. *Mater. Lett.* **61** (17) pp. 3612–3615.
- LUTHER, J.M., JAIN, P.K., EWERS, T. & ALIVISATOS, A P.. 2011. Localized surface plasmon resonances arising from free carriers in doped quantum dots. *Nat. Mater.* **10** (5) pp. 361–366.
- MAMBA, S.M.. 2011. Synthesis, Characterization And Applications Of Dithiocarbamate Transition Metal Complexes. *Inorganica Chim. Acta* p. <http://hdl.handle.net/10210/3629>.
- MTHETHWA, T., PULLABHOTLA, V.S.R.R., MDLULI, P.S., WESLEY-SMITH, J. & REVAPRASADU, N.. 2009. Synthesis of hexadecylamine capped CdS nanoparticles using heterocyclic cadmium

- dithiocarbamates as single source precursors. *Polyhedron* **28** (14) pp. 2977–2982.
- MURRAY, C.B., NORRIS, D. & BAWENDI, M.G.. 1993. Synthesis and characterization of nearly monodisperse CdE (E= S, Se, Te) semiconductor nanocrystallites. *J. Am. Chem. Soc.* **115** (4) pp. 8706–8715.
- NIRMAL, M., MURRAY, C.B. & BAWENDI, M.G.. 1994. Fluorescence-line narrowing in CdSe quantum dots: Surface localization of the photogenerated exciton. *Phys. Rev. B* **50** (4) pp. 2293–2300.
- NOORDIK, J... 1973. TRIS(N,N-DIETHYLDITHIOCARBAMATO)GOLD(III), C₁₅H₃₀AuN₃S₆. *Cryst. Struct. Commun.* **2** pp. 81–84.
- NOVO, C., FUNSTON, A.M. & MULVANEY, P.. 2008. Direct observation of chemical reactions on single gold nanocrystals using surface plasmon spectroscopy. *Nat Nanotechnol* **3** (10) pp. 598–602.
- NYAMEN, L.D., NEJO, A. A., PULLABHOTLA, V.S.R., NDIFON, P.T., MALIK, M.A., AKHTAR, J., O'BRIEN, P. & REVAPRASADU, N.. 2014. The syntheses and structures of Zn(II) heterocyclic piperidine and tetrahydroquinoline dithiocarbamates and their use as single source precursors for ZnS nanoparticles. *Polyhedron* **67** (2) pp. 129–135.
- NYAMEN, L.D., REVAPRASADU, N., PULLABHOTLA, R.V.S.R., NEJO, A. A., NDIFON, P.T., MALIK, M.A. & O'BRIEN, P.. 2013. Synthesis of multi-podal CdS nanostructures using heterocyclic dithiocarbamato complexes as precursors. *Polyhedron* **56** pp. 62–70.
- O'FARRELL, N., HOULTON, A. & HORROCKS, B.R.. 2006. Silicon nanoparticles: Applications in cell biology and medicine. *Int. J. Nanomedicine* **1** (4) pp. 451–472.

- ONWUDIWE, D.C. & AJIBADE, P. A.. 2011. ZnS, CdS and HgS nanoparticles via Alkyl-Phenyl dithiocarbamate complexes as single source precursors. *Int. J. Mol. Sci.* **12** pp. 5538–5551.
- ONWUDIWE, D.C., KRÜGER, T.P.J., OLUWATOBI, O.S. & STRYDOM, C. A.. 2014. Nanosecond laser irradiation synthesis of CdS nanoparticles in a PVA system. *Appl. Surf. Sci.* **290** pp. 18–26.
- OZIN, G. A & CADEMARTIRI, L.. 2009. An Introduction to Nanochemistry Concepts. In *Concepts of Nanochemistry*. KGaA, Weinheim: 2009 WILEY-VCH Verlag GmbH & Co., pp. 11–50.
- PANDEYA, K.B., SINGH, R., MATHUR, P.K. & SINGH, R.P.. 1986. E . s . r . Spectra of Mixed Ligand Manganese (II) Dithiocarbamates. *Transit. Met. Chem.* **11** pp. 347–350.
- PICKETT, N.L. & O'BRIEN, P.. 2001. Syntheses of semiconductor nanoparticles using single-molecular precursors. *Chem. Rec.* **1** pp. 467–479.
- PRADHAN, N., KATZ, B. & EFRIMA, S.. 2003. Synthesis of High-Quality Metal Sulfide Nanoparticles from Alkyl Xanthate Single Precursors in Alkylamine Solvents. *J. Phys. Chem. B* **107** pp. 13843–13854.
- RAHDAR, A., ARBABI, V. & GHANBARI, H.. 2012. Study of Electro-Optical Properties of ZnS Nanoparticles Prepared by Colloidal Particles Method. *Int. J. Chem. Biol. Eng.* **6** (1) pp. 81–83.
- RAJPUT, G., SINGH, V., SINGH, S.K., PRASAD, L.B., DREW, M.G.B. & SINGH, N.. 2012. COOPERATIVE METAL-LIGAND-INDUCED PROPERTIES OF HETEROLEPTIC COPPER(I) XANTHATE/DITHIOCARBAMATE PPH₃ COMPLEXES. *EUR. J. INORG. CHEM.* **24** pp. 3885–3891.
- REVAPRASADU, N. & MLONDO, S.N.. 2006. Use of metal complexes to synthesize semiconductor

- nanoparticles. *Pure Appl. Chem.* **78** (9) pp. 1691–1702.
- SHAHEEN, F., BADSHAH, A., GIELEN, M., DUSEK, M., FEJFAROVA, K., DE VOS, D. & MIRZA, B.. 2007. Synthesis, characterization, antibacterial and cytotoxic activity of new palladium(II) complexes with dithiocarbamate ligands: X-ray structure of bis(dibenzyl-1-S:S'-dithiocarbamato)Pd(II). *J. Organomet. Chem.* **692** pp. 3019–3026.
- SINGH, A., MANIVANNAN, R. & NOYEL VICTORIA, S.. 2014. Simple one-pot sonochemical synthesis of copper sulphide nanoparticles for solar cell applications. *Arab. J. Chem.* **8** pp. 1–9.
- SINGH, B., DREW, M.G.B., KOCIOK-KOHN, G., MOLLOY, K.C. & SINGH, N.. 2011. Unprecedented coordination of dithiocarbamate in multinuclear and heteroleptic complexes. *Dalton Trans.* **40** (3) pp. 623–631.
- TRINDADE, T. & BRIEN, P.O.. 1996. A Single Source Approach to the Synthesis of CdSe Nanocrystallites. *Adv. Mater.* **8** (2) pp. 161–163.
- TYNER, K.. 2015. Quality Considerations and Regulatory Perspectives for Drug Products Containing Nanomaterials. In *Quality Considerations and Regulatory Perspectives for Drug Products Containing Nanomaterials*. pp. 1–46.
- XIE, Y., CARBONE, L., NOBILE, C., GRILLO, V., D'AGOSTINO, S., DELLA SALA, F., GIANNINI, C., ALTAMURA, D., OELSNER, C., KRYSCHI, X.C., ET AL.. 2013. Metallic-like Stoichiometric Copper Surface Plasmon Resonance Properties, and Their Modeling. *ACS Nano* **7** (8) pp. 7352–7369.
- YU, X., CAO, C., ZHU, H., LI, Q., LIU, C. & GONG, Q.. 2007. Nanometer-sized copper sulfide

hollow spheres with strong optical-limiting properties. *Adv. Funct. Mater.* **17** (8) pp. 1397–1401.

ZHANG, L.Z., SUN, W. & CHENG, P.. 2003. Spectroscopic and theoretical studies of quantum and electronic confinement effects in nanostructured materials. **8** (1) pp. 207–222.

ZHAO, Y., PAN, H., LOU, Y., QIU, X., ZHU, J. & BURDA, C.. 2009. Plasmonic Cu_{2-x}S nanocrystals: Optical and structural properties of copper-deficient copper(I) sulfides. *J. Am. Chem. Soc.* **131** (12) pp. 4253–4261.

ZOU, J., ZHANG, J., ZHANG, B., ZHAO, P. & HUANG, K.. 2007. Low-temperature synthesis of copper sulfide nano-crystals of novel morphologies by hydrothermal process. *Mater. Lett.* **61** (28) pp. 5029–5032.

Chapter 2

Methodology

2. Experimental

2.1 Materials and reagents

Zinc chloride, copper chloride (97 %), hexadecylamine (90 %), tri-octylphosphine oxide (90 %), oleylamine, carbon disulphide, aniline, cyclohexylamine, ammonia solution (32 %), and the ammonium pyrrolidine dithiocarbamate ligand were purchased from Sigma Aldrich and used without any purification. Solvents used in this study were methanol, acetone and toluene; all of them were analytical grade and they were also purchased from Sigma Aldrich. The other solvent used was de-ionized water.

2.2 Instrumentation

2.2.1 Fourier transform infrared (FTIR) spectroscopy

All IR spectra were recorded on FT-IR Perkin Elmer 400 spectrometer. Spectra were collected over the range from 650 to 4000 cm^{-1} . FTIR spectroscopy was used to study the structure of the molecules.

2.2.2 Solid state nuclear magnetic resonance (NMR) spectroscopy

Solid state NMR experiments were carried out using 4 mm and 2.5 mm outer diameter zirconia rotors (Bruker, Karlsruhe, Germany); ^{13}C NMR spectra were obtained with a Bruker Advance 111 HD MHz (11.1 Tesla) standard bore spectrometer and either a double beam resonance BBO

or triple channel broad band probe (TrigammaTMMAS probe), at a magic angle spinning rate of 10 KHz, frequency of 125.8 MHz. The ¹³C spectra were reported as ppm. NMR spectroscopy was also used to study the structure of the molecules.

2.2.3 Thermogravimetric analysis (TGA)

TGA was performed on a Perkin Elmer Pyris 6 manager TGA under an inert atmosphere of dry nitrogen, and at a heating rate of 10 °C/min using an alumina pan as a reference. The sample preparation for thermogravimetric analysis was done by weighing 10-15 mg of the sample. The samples were decomposed at temperature ranging from 30 to 900 °C. Thermal analysis was used to determine the temperature at which the material decomposed and the stability of the material.

2.2.4 Ultra-violet visible (UV-vis) spectrometry

Absorption spectra of the particles were measured using a Perkin Elmer Lambda 20 UV-VIS Spectrophotometer. The samples were placed in quartz cuvettes (1 cm path length) with toluene as the solvent. The UV-vis spectra were used to determine the optical properties of the prepared nanoparticles.

2.2.5 Photoluminescence (PL) spectroscopy

Emission spectra of the particles were recorded on a Perkin Elmer LS 45 PL spectrometer with a xenon lamp at room temperature. The samples were placed in glass cuvettes (1 cm) with toluene as solvent. The PL spectra were also used to determine the optical properties of the nanoparticles.

2.2.6 X-ray diffraction (XRD) analysis

X-ray diffraction (XRD) patterns on powdered samples were carried out in 2θ degree on a Bruker axsD8 advance diffractometer. Samples were placed in silicon zero background sample holder. Measurements were taken using a glancing angle of incidence detector at an angle of 2° using a

CuK α 1 source, for 2θ values over $20^\circ - 80^\circ$ in steps of 0.05° with a scan speed of $0.01^\circ 2\theta.s^{-1}$. XRD data was used to reveal the crystalline nature of the nanoparticles.

2.2.7 Transmission electron microscopy (TEM)

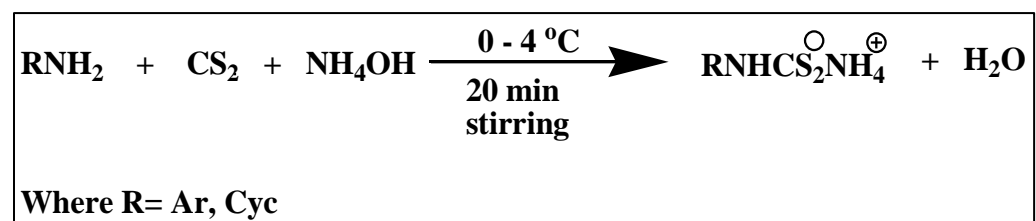
TEM analyses were done on a LEO JEM 912 electron microscope with an acceleration voltage of 120 KW and a tungsten wire filament. The samples were prepared by placing a drop of dilute solution of sample in toluene on to a copper grid. The sample was allowed to dry completely at room temperature. TEM images were used to determine the morphology of the particles.

2.3 Experimental procedure

2.3.1 Preparation of cyclohexylamine-N-dithiocarbamate ligand (Ligand 1)

The method followed was the modification of the method reported by (Onwudiwe & Strydom, 2015). Cyclohexylamine (0.1 mol) was reacted with 16 ml concentrated ammonia solution (32%) in an ice water bath. The reaction was stirred for 10 minutes to attain a temperature of 0°C , then after 10 minutes 6 ml of ice cold carbon disulfide was added drop wise to the mixture. The reaction mixture immediately precipitated a yellowish-white solid upon addition of carbon disulfide. The precipitated mixture was further stirred for 10 minutes to ensure homogeneity in the mixture, the precipitate was then washed with 60 ml methanol and dried by suction drying.

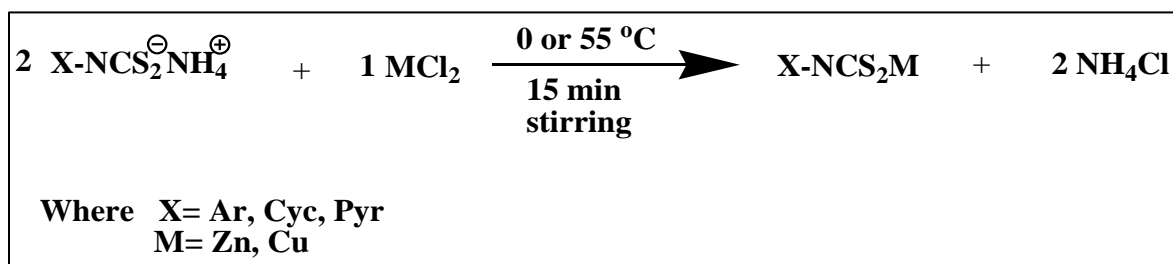
The same procedure was followed for the preparation of phenyl-N-dithiocarbamate ligand (Ligand 2) while ammonium pyrrolidine dithiocarbamate (Ligand 3) was purchased. The summarized synthetic procedure can be observed in **Scheme 2.1**.



Scheme 2.1: Synthetic pathway to make the ligands

2.3.2 Preparation of transition metal complexes

The metal complexes of all samples were all prepared by direct ligand addition to the metal salts in a 2:1 mole ratio (Manav et al., 2006) and (Manav et al., 2004). For ligand 1 hot aqueous solutions of the metal salts (1 g) or hot methanolic solutions of the metal salts were added dropwise to methanolic solutions of the cyclohexylamine-N-dithiocarbamate ligand. For ligand 2 and ligand 3 an ice temperature was used. The synthetic pathway of all the prepared complexes is schematically shown in **Scheme 2.2**.



Scheme 2.2: Synthetic pathway to make the complexes

2.3.2.1 Preparation of bis (cyclohexylamine-N-dithiocarbamato) copper (II)/zinc (II)

The prepared ligand (2 g) was dissolved by reflux in hot methanol at 55°C in a two-neck flask, then after the ligand has dissolved a hot methanolic solution of metal salt either CuCl₂ (1 g) was added drop wise and upon addition the solution precipitated immediately. The precipitate was further stirred for 15 minutes to ensure homogeneity, then the resulting precipitate was washed three times with de-ionized water and methanol and then it was dried in open air.

2.3.2.2 Preparation of bis (pyrrolidine-N-dithiocarbamato) copper (II)/zinc (II)

The ammonium pyrrolidine dithiocarbamate ligand (2 g) was dissolved in methanol at 0°C in a two-neck flask. After the ligand has dissolved a methanolic solution of metal salt either CuCl₂ or ZnCl₂ (1 g) was added drop wise. Upon addition the solution precipitated immediately. The precipitate was further stirred for 15 minutes to ensure homogeneity, then the resulting precipitate was washed three times with de-ionized water and methanol and then it was dried in open air.

The same procedure was followed for the preparation of bis (phenyl-N-dithiocarbamato) copper (II)/zinc (II).

2.3.3 Synthesis of metal sulfide nanoparticles

The synthesis of metal sulfide nanoparticles were prepared using the similar procedure for all the metal complexes. Capping molecules that were used, they were hexadecylamine (HDA) and tri-octyl-n-phosphinoxide (TOPO), to produce HDA-capped and TOPO-capped metal sulfide nanoparticles. Typically a complex (0.5 g) was weighed and dissolved in 6 ml oleylamine, while HDA was heated to 120°C. Then after complete dissolution of the complex the solution was syringed and injected into hot HDA, and the solution was stabilized at 120°C for 1h. After 1 h the solution was then cooled to 70°C and the mixture was then flocculated using methanol. The flocculent was washed 3 times using methanol under centrifugation, and the precipitate was dried at room temperature overnight.

2.4 References

MANAV, N., MISHRA, A.K. & KAUSHIK, N.K.. 2004. Triphenyl phosphine adducts of platinum(IV) and palladium(II) dithiocarbamates complexes: A spectral and in vitro study. *Spectrochim. Acta - Part A Mol. Biomol. Spectrosc.* **60** (13) pp. 3087–3092.

MANAV, N., MISHRA, A. K. & KAUSHIK, N.K.. 2006. In vitro antitumour and antibacterial studies

of some Pt(IV) dithiocarbamate complexes. *Spectrochim. Acta - Part A Mol. Biomol. Spectrosc.* **65** (1) pp. 32–35.

ONWUDIWE, D.C. & STRYDOM, C. A.. 2015. The bipyridine adducts of N-phenyldithiocarbamate complexes of Zn(II) and Cd(II); synthesis, spectral, thermal decomposition studies and use as precursors for ZnS and CdS nanoparticles. *Spectrochim. Acta Part A Mol. Biomol. Spectrosc.* **135** pp. 1080–1089.

Chapter 3

Characterization of dithiocarbamate (DTC) ligands and complexes

3.1 Introduction and spectral analysis of the ligands and complexes

A dithiocarbamate is an organic molecule with a structure that contains two sulfur atoms that can both be involved in bonding with a metal ion. The formation of the dithiocarbamate ligand is highly dependent on the nucleophile (a strong base) that attacks and deprotonates the amine group. Then the critical step is the attack of the deprotonated amine group on the CS_2 in the reaction medium to form a DTC compound. The choice of the ligands used in this study is based on their structural effect on the formation of nanoparticles. Ligand 1 and 2 have the same number of carbon atoms but the difference lies in the fact that ligand 1 contains cyclohexylamine that is more basic than ligand 2 that contains aniline that has a phenyl ring. The lower basicity is due to the electron withdrawing aryl group, while the cyclohexylamine consists of the aliphatic group which is an electron donating groups. Then in ligand 3 the pyrrolidine choice is based on the fact that it is a secondary amine and it is also because pyrrolidine is distinctive because of its compactness, which is a consequence of its cyclic structure. Therefore the interactions of the three ligands with metal ions will be different and also their affinities will be slightly different upon complexation.

Spectroscopic studies gives an insight on the proposed mechanism of the reaction, thus leading to the use of the most important peaks to study the ligand and complexes. The FTIR and NMR

spectroscopic techniques are the powerful analytical instruments for studying the structure of a particular molecule or compound.

In the ^{13}C NMR spectra, the CS_2 moiety appeared with a chemical shift of above ± 200 ppm for low oxidation state transition metals (such as divalent Zn atom) (Van Gaal et al., 1979), of which had a very low-intensity signal for the Zn complexes. Then NMR spectra of the copper complexes could not be recorded since they showed paramagnetic behavior.

The IR spectrum of the CS_2 appeared as an intermediate peak between the single and the double bond of the DTC ligands. The intermediate peak was the signal of the bidentate bonding with the metal ion. The exception was the cyclohexylamine ligand (complex 1) which showed a doublet in the CS_2 vibration that had a splitting distance that is $> 20 \text{ cm}^{-1}$, thus indicating a monodentate type of the bonding (Gandhi et al., 1996). The IR for all complexes were shifted from the ligand and except that from the cyclohexylamine DTC Zn complex (complex 1) and N-phenyldithiocarbamate Zn complex (complex 3), they all showed bidentate coordination fashion. Complex 1 also showed double peaks in N-H stretch range which was similar to the pristine cyclohexylamine which was attributed to the instability of the prepared complex at elevated temperatures. **Table 2** summarizes the important FTIR spectral peaks of prepared DTC compounds. The NMR spectrum did not show the presence of the NCS_2 group as seen from the FTIR spectroscopy for complex 1. This can be attributed to the unstable nature of the complex and the presence of impurities in the pristine cyclohexylamine. The important NMR spectral signals are summarized in **Table 4**. The thermal analysis of the metal complexes all gave a metal sulfide final residue except for complex 3 which gave a final residue of Zn atom.

Table 2: Diagnostic IR bands of all ligands and their complexes

Compounds	Wavenumber (cm ⁻¹)			
	N-H	C-----N	^{sym} C-----S	^{asym} C-S
Ligand 1	3312	1458	981	–
Ligand 2	3457	1441	995	–
Ligand 3	–	1414	992	–
Complex 1	3308	1499	982	952
Complex 2	3325	1405	1027	–
Complex 3	3401	1446	995	975
Complex 4	3251	1490	958	–
Complex 5	–	1479	1006	–
Complex 6	–	1489	1004	–

Ligand **1** (cyclohexylamine-N-dithiocarbamate), **2** (N-phenyldithiocarbamate) & **3** (ammonium pyrrolidine dithiocarbamate) and complexes **1** (bis(cyclohexylamine-N-dithiocarbamato)Zn(II)), **2** (bis(cyclohexylamine-N-dithiocarbamato)Cu(II)), **3** (bis(N-phenyldithiocarbamato)Zn(II)), **4** (bis(N-phenyldithiocarbamato)Cu(II)), **5** (bis(N-pyrrolidinedithiocarbamato)Zn(II)) & **6** (N-pyrrolidinedithiocarbamato)Cu(II)).

Infrared spectra is a useful technique to determine the type of bonding in organic molecules and their coordination compounds. One of the most important feature to confirm the formation of the metal sulfide complexes is the presence and the formation of the metal-sulfide bond.

The IR spectra of the pristine ligands and the prepared DTC's ligands were assigned. The IR spectra of the DTC ligands (cyclohexylamine-N-dithiocarbamates, N-phenyldithiocarbamate, and N-pyrrolidinedithiocarbamates ligands (Ligands 1, 2 and 3 respectively)) and their respective complexes were recorded. The DTC ligands have three distinct band ranges that should be taken into consideration. The band ranges are as follows; 3300-3100, 1550-1400, and 1050-950 cm^{-1} which are attributed to $\nu(\text{N-H})$, $\nu(\text{C=N})$ and $\nu(\text{C=S})$ stretching modes respectively. In a symmetrical DTC complex $\nu(\text{N} \text{---} \text{C})$ become intermediate between the single and the double bond of the $\nu(\text{C-N})$ and $\nu(\text{C=S})$ appearing in the region of 1250-1350 and 1450-1680 cm^{-1} respectively. The thioureide band is the most important peak used to predict the movement of the electron cloud of the $-\text{NCS}_2$ group after binding to the metal center (Mohammad et al., 2009).

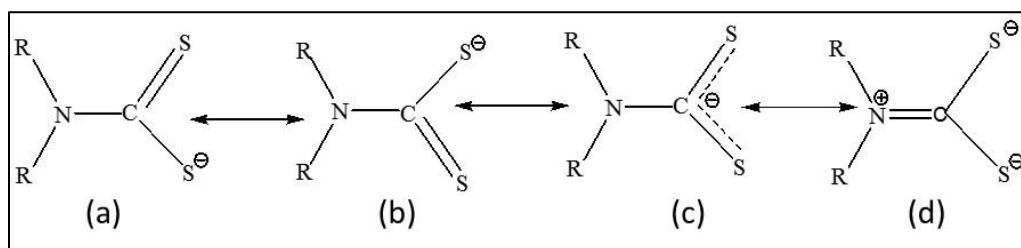


Figure 3.1: Resonance forms of dithiocarbamic- NCS_2^- moiety (Alverdi et al., 2004)

The importance of the resonance structure (d) in Figure 3.1 is a result of the strong electron-releasing property of the $-\text{NR}_2$ and the ability of the sulfur atom to accept electrons into its d-orbitals (Halls, 1969). While the presence of a negative charge on the sulfur atom has an effect on the bond order of the DTC's compound, because it can decrease the $-\text{N}-\text{C}$ bond order due to weakened movement of the electrons towards the sulfur atoms. The $\nu(\text{N} \text{---} \text{C})$ can appear outside the region proposed at lower frequencies, especially when the group attached to the N atom is an aryl or H (Kaul & Pandeya, 1979). This is caused by the electron-withdrawing aryl group which can lead to a decrease in the electron-releasing ability of the $-\text{N} \text{---} \text{C}$ group (Kaul & Pandeya,

1979). The other important peak is the CS peak, which can be used to indicate the type of bonding between the metal ion and the ligand. A strong single band absorption in the region of 950-1050 cm^{-1} is an indication of symmetrical bidentate binding (Fig. 3.1 (c) and (d)), of a metal ion bonding via the CSS moiety of the ligand (Kaul & Pandeya, 1979) and (Halls, 1969). The asymmetrical compound consists of the $\nu(\text{C}=\text{S})$ and $\nu(\text{C}-\text{S})$ of which the later appears as a weak band in the range of 860-820 cm^{-1} , Fig. 3.1 (a) and (b) is the typical resonance structure associated with an asymmetrical monodentate bonding.

The pristine cyclohexylamine data was used to identify the binding site of the CS_2 moiety in the cyclohexylamine structure.

3.1.1 Cyclohexylamine-N-dithiocarbamate ligand (Ligand 1) and its zinc complex, 1

IR spectroscopy was used to check the binding mode of the ligand and its bonding with a metal ion, and also for the indication of functional groups present in the prepared materials. Therefore the Fig. 3.2 spectra shows the peaks of interest from the cyclohexylamine-N-dithiocarbamate ligand and its corresponding bis(cyclohexylamine-N-dithiocarbamate)Zn(II) complex (complex 1). There were three regions of interest which are attributed to, the $\nu\text{-N-H}$ stretch, $\nu\text{-NCS}_2$, and $\nu\text{-CS}$ modes in the ligand. The $\nu(\text{N-H})$ peak was the single peak on the ligand as opposed to the double peaks on the pristine cyclohexylamine sample. This therefore indicates the bonding of dithiocarbamate moiety on the nitrogen atom, converting it from primary to a secondary amine, the $\nu(\text{N-H})$ stretch occurred at $\nu\text{-3312 cm}^{-1}$.

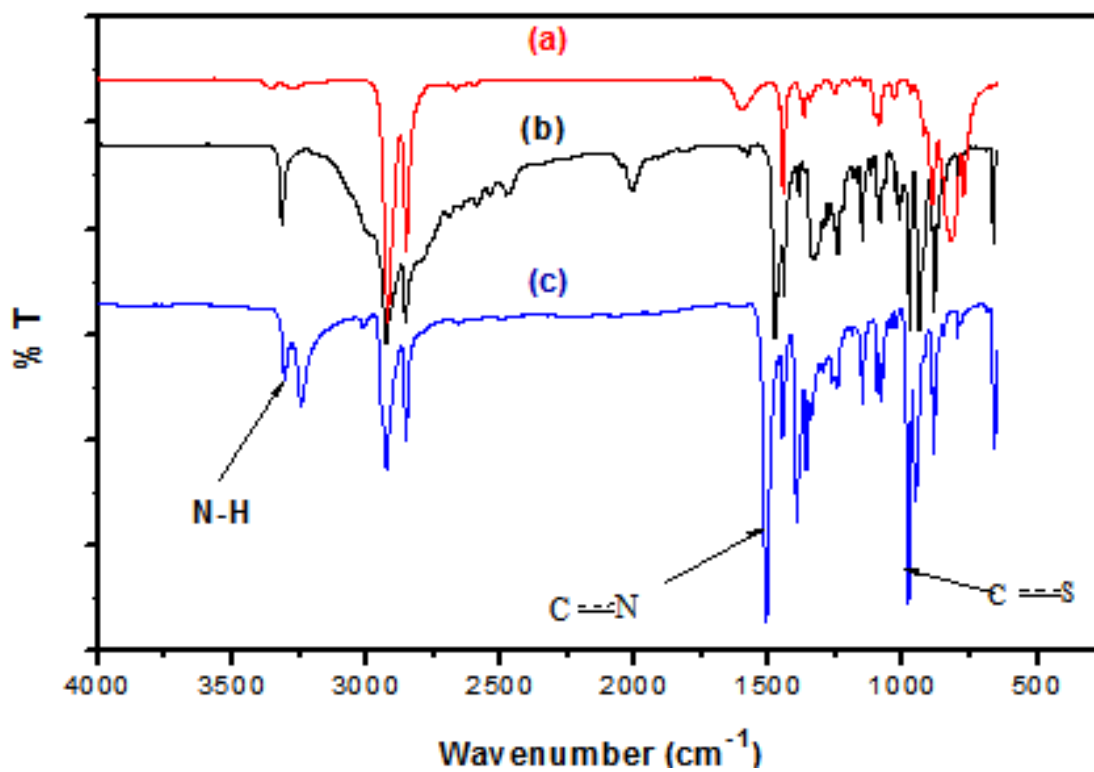
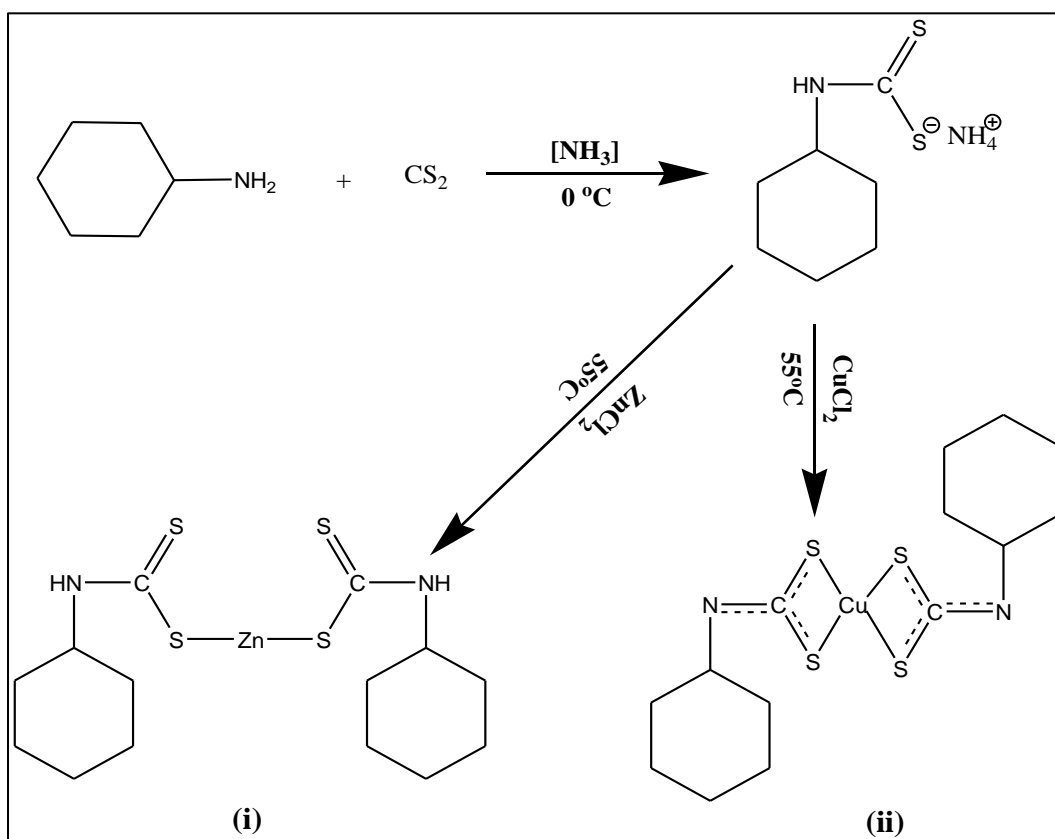


Figure 3.2: FTIR spectra of (a) Pristine cyclohexylamine, (b) Ligand 1, and (c) Complex 1

The $\nu(\text{NCS}_2)$ peak was observed at 1458 cm^{-1} . This band was intermediate between a single bond and the double bond of the CN bands (Manav et al., 2006) and (Chatt et al., 1956). The other peak of interest was the $\nu(\text{C-S})$ band which occurred at 981 cm^{-1} which was also intermediate between a single and double bond of the CS bands. In the spectrum of a complex it is predicted that there should be a shift of particular bands to higher or lower frequencies upon complexation due to electron density change due to the metal atom. In this case there was a shift of $\nu(\text{N-H})$ to lower frequency by $\pm 4 \text{ cm}^{-1}$ from 3312 cm^{-1} for the ligand to 3308 cm^{-1} for the complex and there was a splitting of the complex band which was not expected, but this could be due to impurities (albeit the peak position suggests otherwise) of un-reacted cyclohexylamine which were triggered by heating the ligand when preparing the complex. The peak at 1458 cm^{-1} is attributed to the partial

double (intermediate of single and double bond of CS and CN peaks) of $\nu(\text{C-N})$ of the ligand shifted to higher frequency in the complex 1499 cm^{-1} by $\pm 41\text{ cm}^{-1}$ from the ligand. This shift in this band is said to confirm an increase in the C-N double bond character due to mesomeric effect of an electron cloud of the $-\text{NCS}_2$ moiety toward the metal ion suggesting a strong contribution of the thioureide resonance form to the structure of dithiocarbamate (Mamba et al., 2010), (Manav et al., 2004) and (Mohammad et al., 2009). The partial double bond of $\nu(\text{C-S})$ appeared at a slightly higher frequency of 982 cm^{-1} and 952 cm^{-1} with a strong doublet splitting which indicates monodentate binding of the dithiocarbamate ligand as shown in **scheme 3.1 (i)** for the Zn complex (Mohammad et al., 2009). This suggests the bonding via CS moiety with the metal ion.



Scheme 3. 1: Reaction for the formation of ligand, and complexes via (i) monodentate and (ii) bidentate bonding

3.1.2. Cyclohexylamine-N-dithiocarbamate ligand 1 and its copper complex, 2

Figure 3.3 shows a spectrum of cyclohexylamine DTC ligand and its corresponding complex, bis(cyclohexylamine-N-dithiocarbamato)Cu(II) complex (complex 2). There was a shift in bands in the complex in comparison to the ligand spectrum. The ν -N-H band was broad as compared to the ligand ν -N-H peak, this could be due to the coordinated solvent (methanol) in the prepared complex.

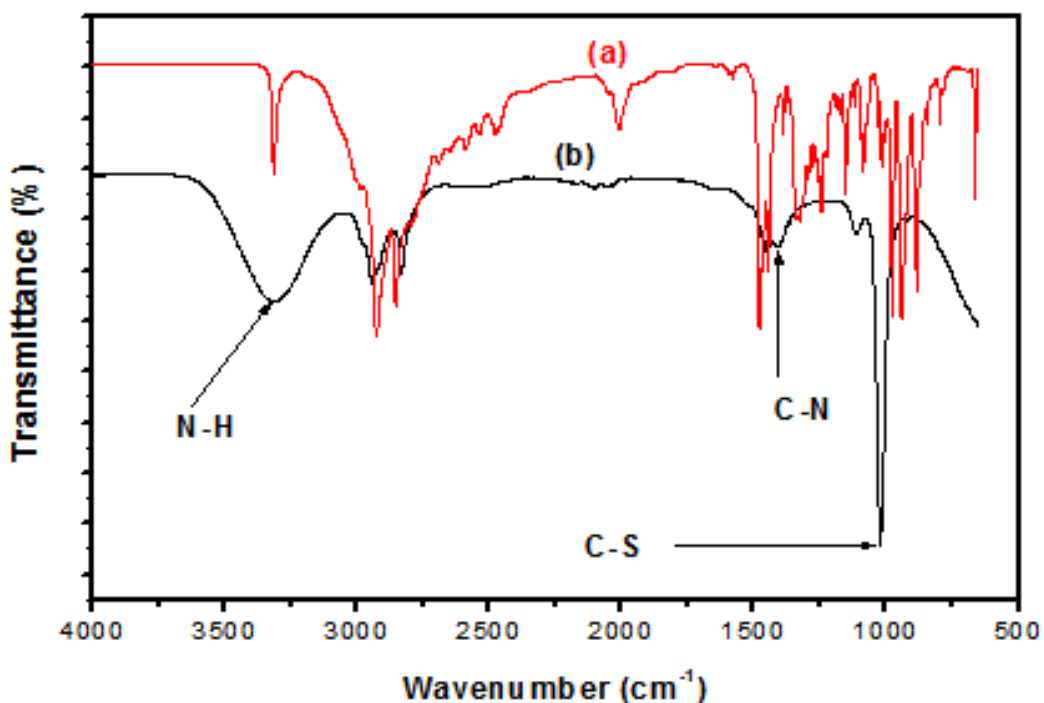


Figure 3.3: FTIR spectra of (a) Ligand 1 and (b) complex 2.

The complex ν -N-H peak had shifted slightly to higher frequencies by ± 14 cm⁻¹ to 3325 cm⁻¹ from 3312 cm⁻¹ of the ligand, due to the strengthening of N-H bond in the complex compared to the free

ligand, as a result of electron donation from sulfur (Ray & Sathyanarayana, 1973) and (Al-Maythality et al., 2013). The other shift was observed in the complex were in the region of 1405 cm^{-1} for the thioureide band and there was also a decrease in the intensity of the peak, due to π -system (refer to **scheme 3.1 (ii)**, the resonance of π -electrons from the nitrogen atom to the CS_2 moiety) in the thioureide moiety. The CS_2 moiety absorption occurred at 1027 cm^{-1} with a very strong intense single peak without any splitting. This suggested a bidentate bonding of the dithiocarbamate ligand with the metal ion (**scheme 3.1 (ii)** is a typical example of bidentate bonding). The shift in the thione peak to higher vibrational frequency upon complexation is due to the electron donation from sulfur to the metal center that promotes π -back donation to a thione π^* orbital, this causes weakening of the C-S bond, thus forming a strong chelating bond with the metal ion (Al-Maythality et al., 2013) and (Wang & Guo, 2008). Complex 1 and complex 2 showed different shifts from the ligand due to their difference in the central metal atom atomic radius, the copper on the other hand has a vacant d-orbital that causes distortion on the axial position (Jahn-Teller distortion) (Janes & Moore, 2004). Complex 2, $\nu(\text{N-H})$ and $\nu(\text{C-S})$ stretches appeared at higher frequencies, while the $\nu(\text{NCS}_2)$ was observed at lower frequencies than complex 1. The other difference in the two complexes was in the type of bonding; complex 1 showed a monodentate type of bonding as shown in **scheme 3.1 (i)** while complex 2 showed a bidentate bonding as shown in **scheme 3.1 (ii)**.

3.1.3. N-Phenyldithiocarbamate ligand (ligand 2) and its zinc complex, 3

Aniline is a liquid primary amine which has an IR spectrum with a shoulder band next to the doublet peak of N-H stretch, which is due to the overtone of the N-H bend of primary amine which occurred at ν -1618 cm^{-1} (Workman & Weyer, 2007) and (Bellamy, 1980). Three bands were of

interest for the ligand which are the N-H, N-CSS, and C=S stretching modes. Therefore, as the ligand showed only one absorption peak at ν -3457 cm^{-1} suggesting that the primary amine (aniline) had converted to a secondary amine (Ajibade & Botha, 2016). For the bis(N-phenyldithiocarbamato)Zn(II) complex (complex 3) the N-H stretching vibration shifted to 3401 cm^{-1} and the ν (C-N) stretching mode of the ligand shifted from ν -1441 cm^{-1} (pure ligand) to ν -1446 cm^{-1} . The vibration shifted due to the electronegative moiety of CSS that was bonded to the N-H moiety and also because of the increased electron density around the metal ion. New bands were observed at 995 and 975 cm^{-1} which can be attributed to C=S and C-S for both ligand and complex. The former only showed a peak at 995 cm^{-1} which was split upon complexation (Ajibade & Botha, 2016; Mamba et al., 2010). The asymmetric peak of the complex suggests monodentate type of bonding. **Scheme 3.2** shows the type of bonding for complex 3.

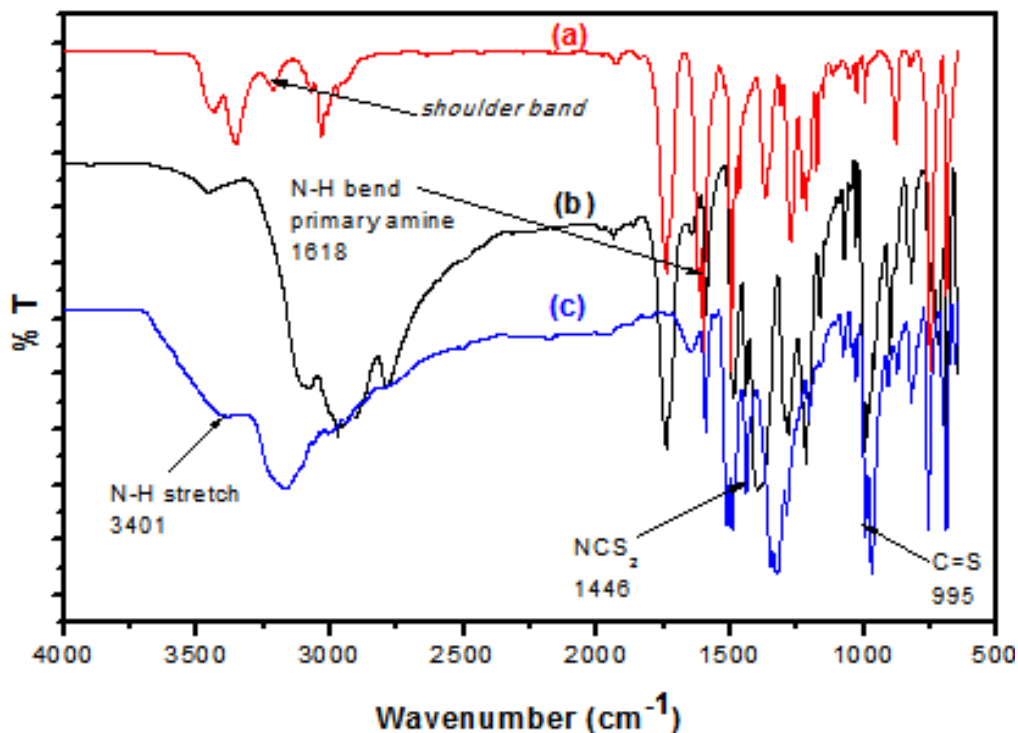
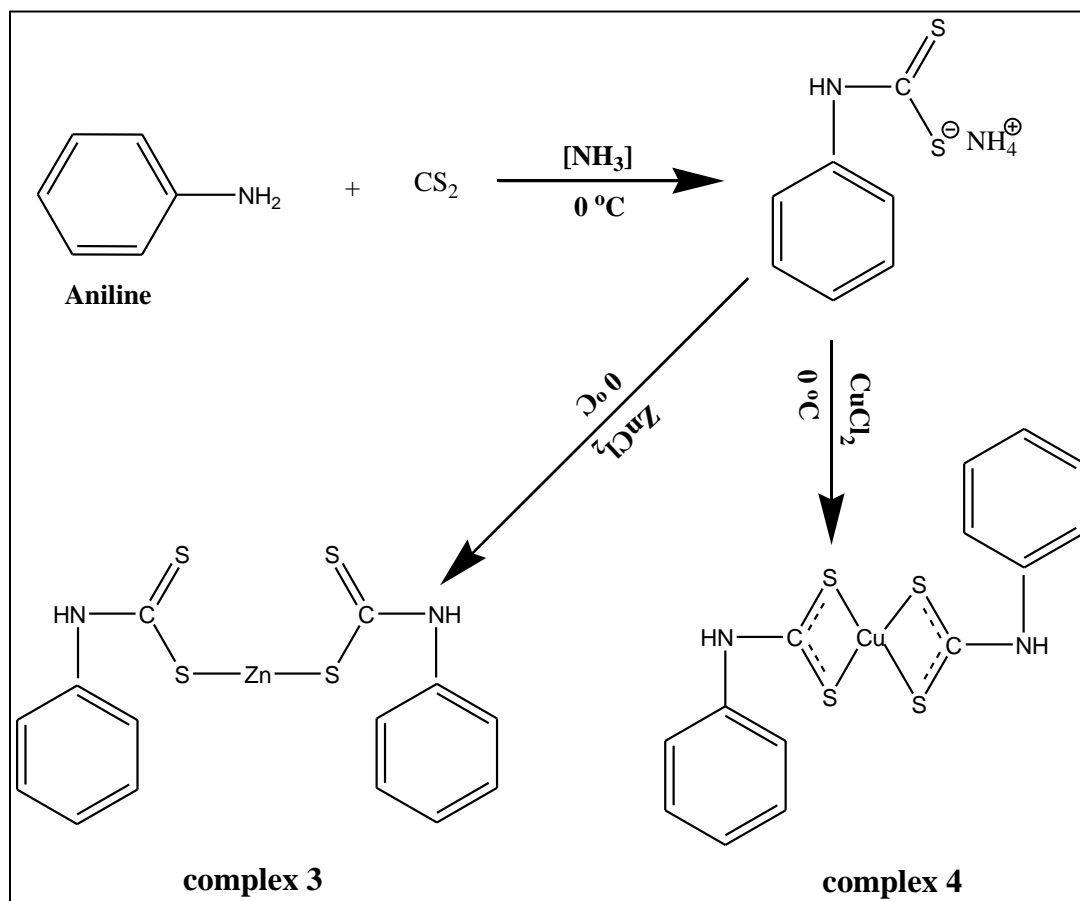


Figure 3.4: FTIR spectra of (a) Pristine Aniline, (b) Ligand 2, and (c) Complex 3

3.1.4. N-Phenyldithiocarbamate ligand **2** and its copper complex, **4**

The interaction of the DTC ligand with copper(II) chloride to form bis(N-phenyldithiocarbamato)Cu(II) adduct, was studied by FTIR spectroscopy (**Fig. 3.5**). The N-H vibration in figure 3.5 (a) and (b) were observed at 3251 and 3457 cm^{-1} respectively, the shift in complex to lower frequencies is due to the electron donation of the nitrogen atom to the sulfur atom (Al-Maythality et al., 2013). On the other hand, the distinctive thioureide band, $\nu(\text{C-N})$ was detected at 1490 cm^{-1} in the complex. Since these frequency modes lie in between those associated with single C-N and double C=N bonds, then this peak represent a partial double bond character of the 'thioureide' bond of dithiocarbamates (Manav et al., 2006) and (Jian et al., 1999). The presence of the 'thioureide' band between 1545–1430 cm^{-1} suggest a considerable double bond character in the C \cdots N bond vibration of the $\text{S}_2\text{C-NR}_2$ group (Jayaraju et al., 2012), (Manav et al., 2006) and (Altaf et al., 2015). The shift to higher frequency is attributed to increased electron density in the Cu ion upon complexation. The symmetrical band at 958 cm^{-1} range of the complex is attributed to the prevailing contribution of C \cdots S (Jayaraju et al., 2012). Vibrations in these ranges have been used to indicate the type of bonding that prevails, either the monodentate or the bidentate bonding as seen in **scheme 3.2**. In this case the appearance of one peak without any splitting is an indication of the bidentate type of bonding in the prepared complex **4** (in **scheme 3.2**). In comparison to complex **3**, there were significant shifts in $\nu(\text{N-H})$, $\nu(\text{C-N})$ and $\nu(\text{C-S})$ bands. Complex **3** showed higher frequencies in $\nu(\text{N-H})$ and $\nu(\text{C-S})$, while the $\nu(\text{C-N})$ appeared in lower frequencies. The zinc complex showed a monodentate bonding while the copper complex showed a bidentate bonding. These results followed a similar trend of the results obtained from the cyclohexylamine ligand. **Scheme 3.2** summarizes the type of bonding that occurred in the

preparation of the ligand and the complexes. The bonding of the metal ion with the ligand is also shown.



Scheme 3. 2: Reaction for the formation of aniline ligand and its corresponding complexes

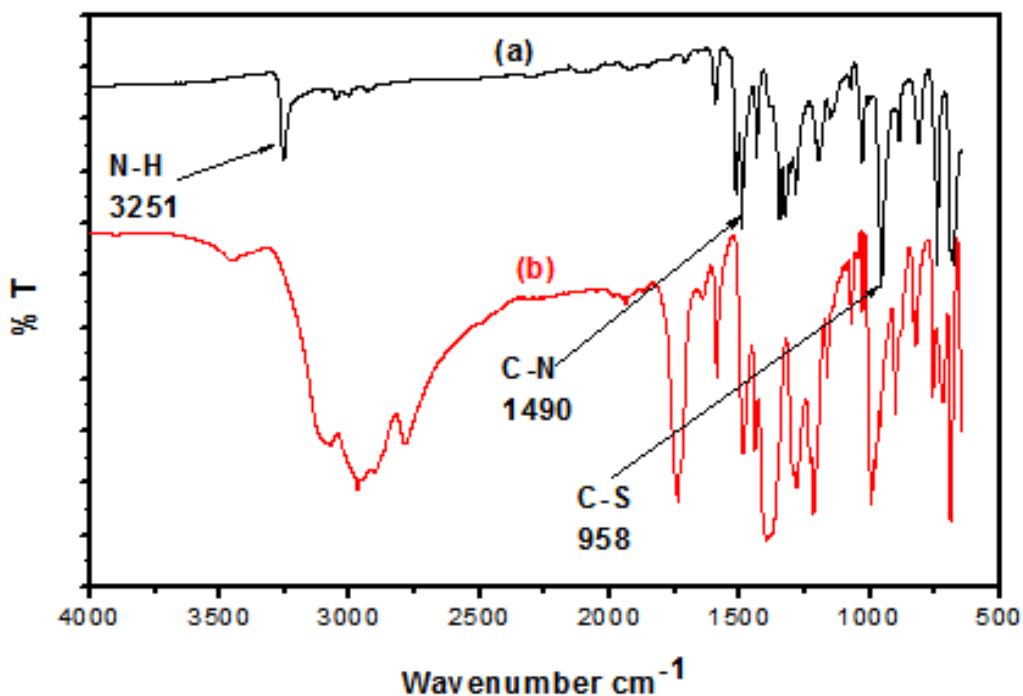


Figure 3.5: FTIR spectra of (a) Complex 4 and (b) Ligand 2

3.1.5 Ammonium pyrrolidinedithiocarbamate ligand and their complexes

In the spectra of a complex it is always predicted that there should be a shifting of particular bands to higher or lower frequencies upon complexation due to electron density around the metal atom. In this case there was no N-H peak as anticipated since pyrrolidine is a secondary amine, so the bonding occurred via the nitrogen. The peak at 1414 cm⁻¹ is attributed to partial (C-N) double bond of the ligand, it had shifted to a higher frequency 1479 cm⁻¹ which increased by ± 65 cm⁻¹ from the ligand. The shift in this band confirms an increase in the C-N double bond character due to mesomeric drift of an electron cloud of the -NCS₂ moiety toward the metal ion. Suggesting a strong contribution of the thioureide resonance form to the structure of dithiocarbamate (Mamba et al., 2010) and (Faraglia et al., 2005). The partial double bond of ν -(C=S) appeared at a slightly

higher frequency of 1006 cm^{-1} from 992 cm^{-1} without any split of bands which indicates a bidentate bonding of the dithiocarbamate ligand. Complex **6** showed that the $\nu(\text{C-N})$ band had also shifted to higher frequency 1489 cm^{-1} , owing to the increased double bond character in the CN group, caused by electron delocalization toward the metal center (Faraglia et al., 2005). The other shift was on the $\nu(\text{C-S})$ band which was a symmetrical peak at 1004 cm^{-1} was intermediate of the single and double bond of the CS_2 moiety (Casas et al., 1989). There was no split on the $\nu(\text{C-S})$ peak which indicates the bidentate bonding of the dithiocarbamate ligand. This thus suggests the bonding via CSS moiety in a bidentate fashion.

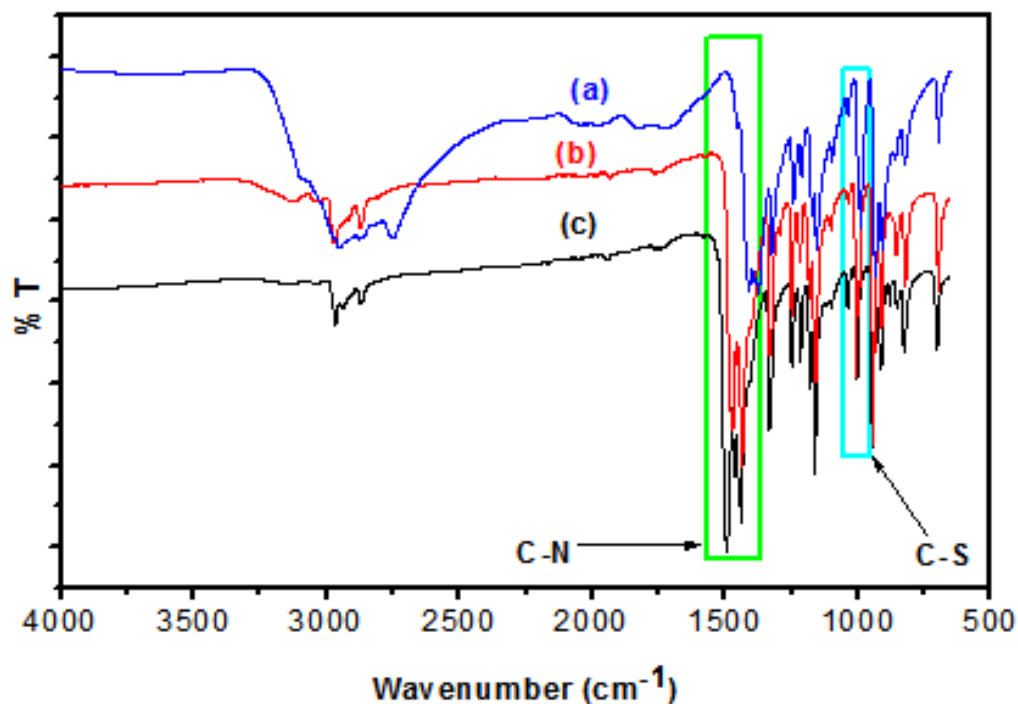


Figure 3.6: FTIR spectra of (a) Ligand 2, (b) Complex 5 and (c) Complex 6

In all the prepared samples the coordination was clearly shown from the FTIR spectroscopy and the results were well comparable to results obtained from the literature (**Table 3**). **Table 3** shows that cyclohexylamine and aniline DTC ligands (ligand 1 and 2 respectively) FTIR frequencies were very close to the same ligands that were previously reported. This thus confirm that the reaction of CS₂ took place. The pyrrolidine DTC ligand was compared to the piperidine DTC ligand since they are both heterocyclic amines similar in structure. The difference being that piperidine is a six-membered ring, while the former being the five-membered ring.

Table 3: Comparison of selected peaks from FTIR spectra with literature

Compound	Band	Frequency (cm ⁻¹)	Reference
Ligand 1	N-H	3312	This study
	C-N	1458	
	C-S	981	
Ligand C	N-H	3318	Mamba et al. (2010)
	C-N	1482	
	C-S	974	
Ligand 2	N-H	3457	This study
	C-N	1441	
	C-S	995	
Ligand A	N-H	3416	Ajibade and Botha, (2016)
	C-N	1476	
	C-S	994	
Ligand E	N-H	3407	Ajibade and Botha, (2016)
	C-N	1448	
	C-S	990	
Ligand 3	N-H	No peak	This study
	C-N	1414	
	C-S	992	
Ligand P	N-H	No peak	Nabipour et al. (2011)
	C-N	1470	
	C-S	976	

Ligand C: cyclohexylamine-N-dithiocarbamate, Ligand A: N-phenyldithiocarbamate, Ligand E: N-ethylphenyldithiocarbamate, and Ligand P: N-piperidinedithiocarbamate

In this study, the ligand spectra showed an interesting trend as seen in **Table 2**, whereby **Ligand 1** showed a NCS_2 vibration at higher frequencies compared to **Ligand 2** and **Ligand 3**. This higher frequency vibration could be due to the fact that ligand 1 consist of cycling ring which consists of electron donating CH_2 , while **Ligand 2** consists of an aryl group that is electron withdrawing and **Ligand 3** is electron withdrawing as well since the nitrogen atom is substituted directly in the ring.

3.2. ^{13}C nuclear magnetic resonance (NMR) spectra studies of the ligands

^{13}C NMR spectroscopy is an important analytical technique used for the determination of the structures of organometallic and coordination compounds. NMR spectroscopy helps in determining the structure of the synthesized samples by use of a magnetic field (internal magnetic fields within a molecule differ distinctly at each chemical site), causing nuclei to be shielded/deshielded. The extent of shielding is influenced by many structural features within the molecule, hence the name chemical shift. In the past, NMR spectroscopy has been used to study the structure of various dithiocarbamates. (Van Gaal et al., 1979) observed that the chemical shift of the carbon atom in the NCS_2 fragment of the dithiocarbamate ligand varies with the coordinated atom and with changes in the molecular framework. While NMR studies of ligand exchange in some metal dithiocarbamates were done by (Beinrohr & Garaj, 1980). Their ligand-exchanged rate was affected by the metal center's magnetic properties (diamagnetic, ferromagnetic or

paramagnetic). **Table 4** summarizes the CS₂ moiety NMR spectrum results, while Table 5 summarizes the whole NMR spectrum results. From **Table 4** it is apparent that the CS₂ in most cases appeared in the region above ca. 200 ppm.

Table 4: ¹³C NMR spectral data of NCS₂ moiety for the ligands and complexes

Compounds	δ NCS ₂ (ppm)
Ligand 1	206.9
Ligand 2	206.3
Ligand 3	202.7
Complex 1	–
Complex 3	206.1
Complex 5	199

3.2.1 Cyclohexylamine-N-dithiocarbamate ligand (Ligand 1)

Figure 3.7 shows five signals for the synthesized ligand as theoretically anticipated. The furthest downfield carbon signal was a very weak signal observed at a chemical shift (δ) of 206.9 ppm which was assigned to C in the thioureide moiety (NCS₂) (Arul Prakasam et al., 2007) and (Van Gaal et al., 1979). ¹³C NMR spectrum shows low intensity signals when carbon is not attached to a hydrogen atom. The nonequivalent signal at δ 55.8 ppm was assigned to a C atom that is directly bonded to the electronegative nitrogen atom, this was consistent with the values reported by (Mamba et al., 2010). The other signals were attributed to CH₂ groups in the cyclohexyl ring. The equivalent α -CH₂ appeared in the chemical shift number of δ 52.9 ppm (not clearly defined). The other equivalent β -CH₂ appeared in the chemical shift of δ 25.3 ppm (not clearly defined), which

was the most up-field carbon atom. While the other nonequivalent γ -CH₂ group occurred at δ 31.7 ppm.

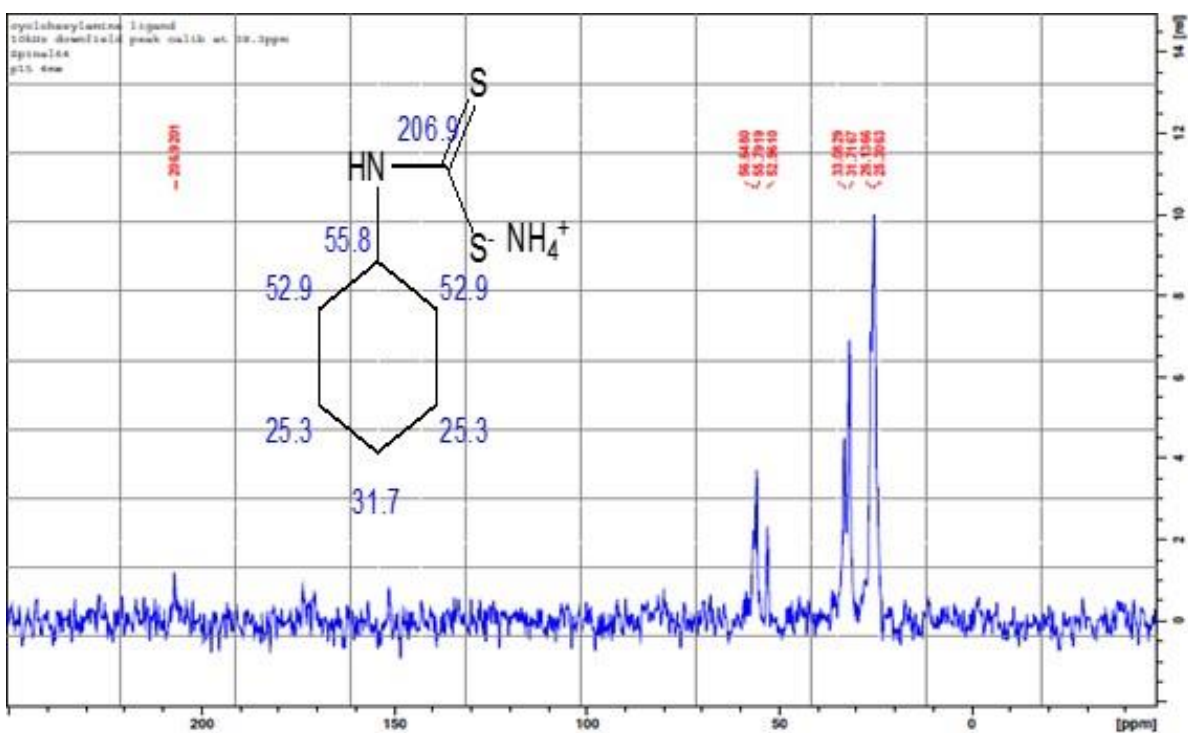


Figure 3.7: NMR spectrum of cyclohexylamine-N-dithiocarbamate ligand

3.2.2 bis(cyclohexylamine-N-dithiocarbamato)Zn(II) [complex 1]

Figure 3.8 shows NMR spectrum of complex **1**. There were three visible signals in the spectrum from the five theoretical predicted signals. The NCS₂ carbon atom was not observed on the spectrum due to weak signal of the NCS₂. The signal due to C atom bonded directly to the nitrogen atom shifted slightly downfield by 2 ppm from that is seen in the ligand (Fig. 3.7). While the β -CH₂ was slightly shifted in comparison with the ligand spectrum. The equivalent methylene groups bonded to the β -CH₂ group had a slight shift of 0.4 ppm upfield. The other nonequivalent γ -CH₂

group had a slight shift of 0.6 ppm downfield. The shifts in signals confirm coordination of the ligand with the metal ion. **Table 5** shows a detailed summary of the NMR results obtained.

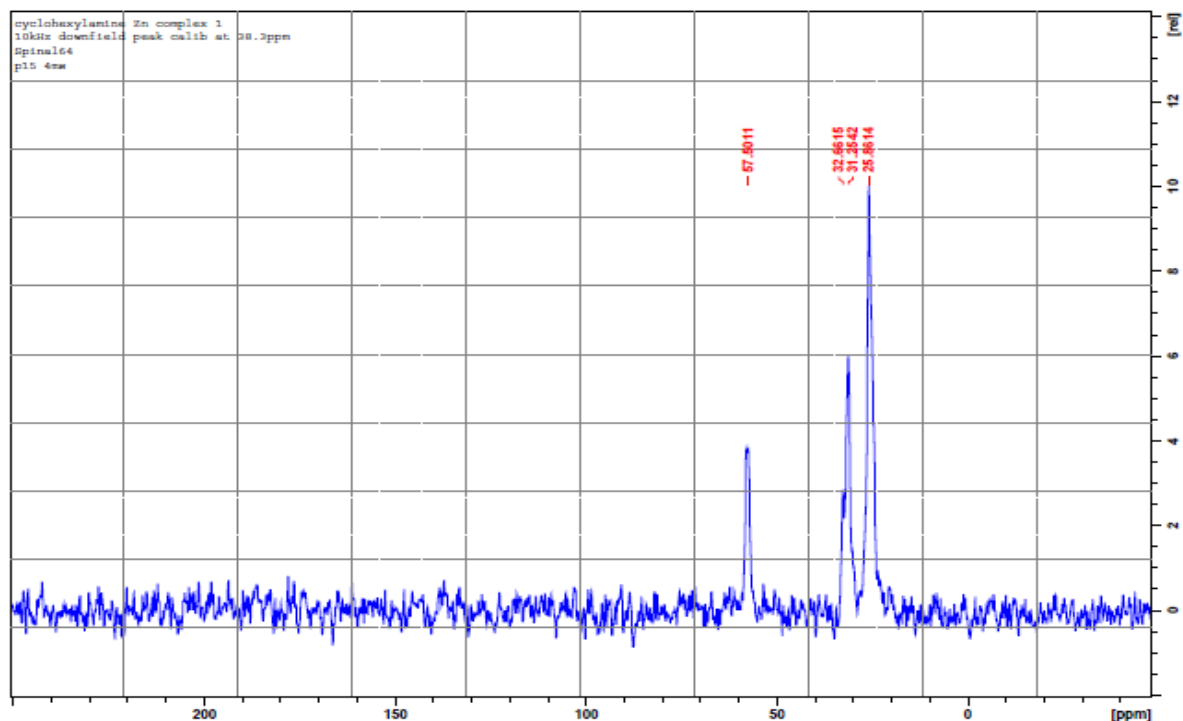


Figure 3.8: NMR spectrum of bis(cyclohexylamine-N-dithiocarbamato)Zn(II) complex.

3.2.3 N-Phenyldithiocarbamate ligand (Ligand 2)

N-phenyldithiocarbamate ligand spectrum is presented in Fig. 3.9. The structure showed four detected signals, while the fifth signal can also be observed. The fifth signal is hard to detect due to that the NCS_2 carbon is not attached to any hydrogen atom. The nonequivalent CH carbon attached directly to the nitrogen was observed at δ 139.4 ppm, the equivalent α - CH_2 bonded to the carbon that is directly bonded to the nitrogen appeared at δ 126.5 ppm. The other equivalent β - CH_2 occurred at δ 130.8 ppm. While the further upfield nonequivalent γ - CH_2 carbon occurred at δ 124.5 ppm.

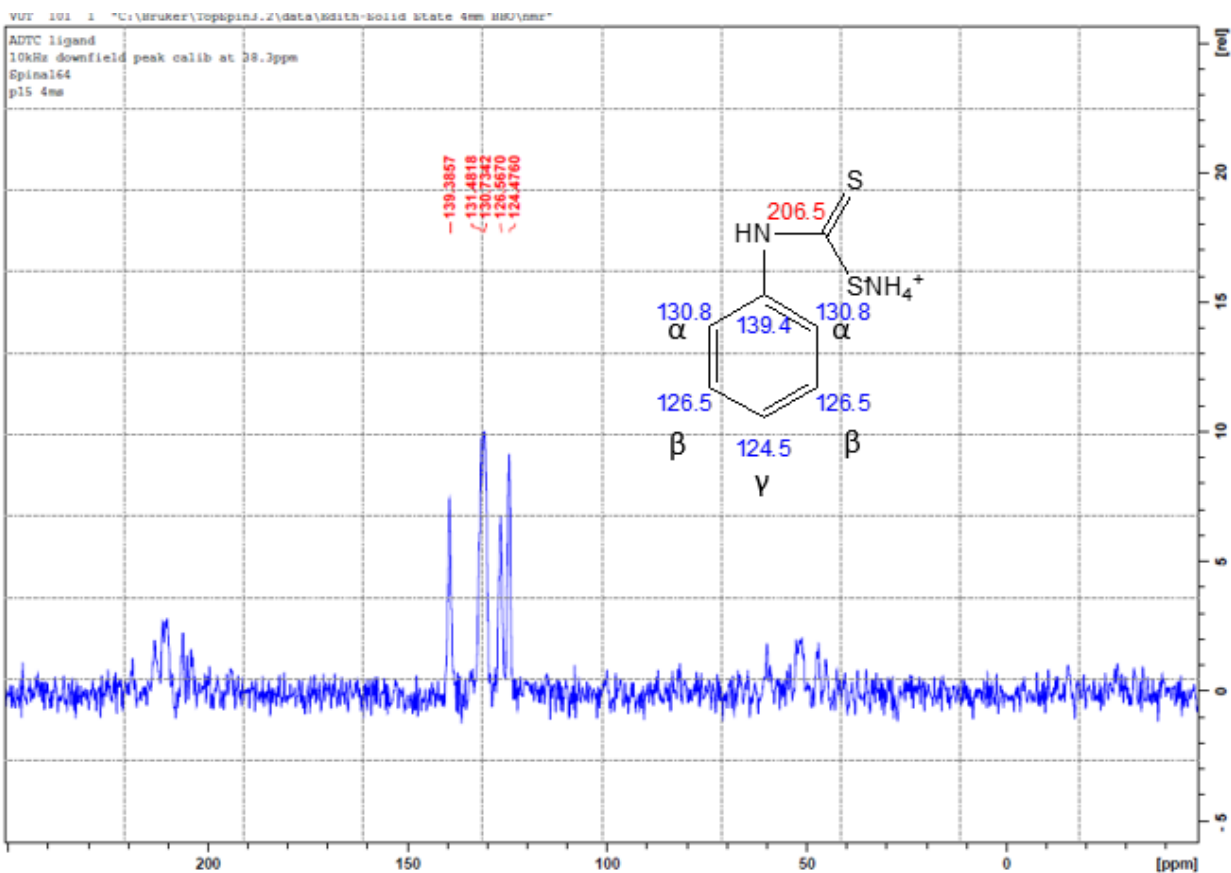


Figure 3.9: NMR spectrum of N-phenyldithiocarbamate ligand.

3.2.4. bis(N-phenyldithiocarbamato)Zn(II) [complex 3]

The spectrum of complex showed a similar number of signals as the ligand, but the δ $N^{13}CS_2$ was much more intense than that of the ligand, but it was still not detected by the instrument which was surprising considering its intensity. Nevertheless after some calculations of trying to assign the signal, the signal that was calculated gave a signal number of δ 206.1 ppm which was a slight upfield shift from the parent ligand. This further supports the coordination via CS_2^- moiety (Manav et al., 2006). On the other hand the non-equivalent CH carbon attached directly to the nitrogen was observed downfield at δ 137.1 ppm, which was also a slight upfield shift from the parent ligand. While the equivalent α -CH₂ bonded to the carbon that is directly bonded to the nitrogen appeared

upfield at δ 126.2 ppm which was upfield as well, all the signals were upfield in comparison to the parent ligand, thus confirming the metal-ligand coordination.

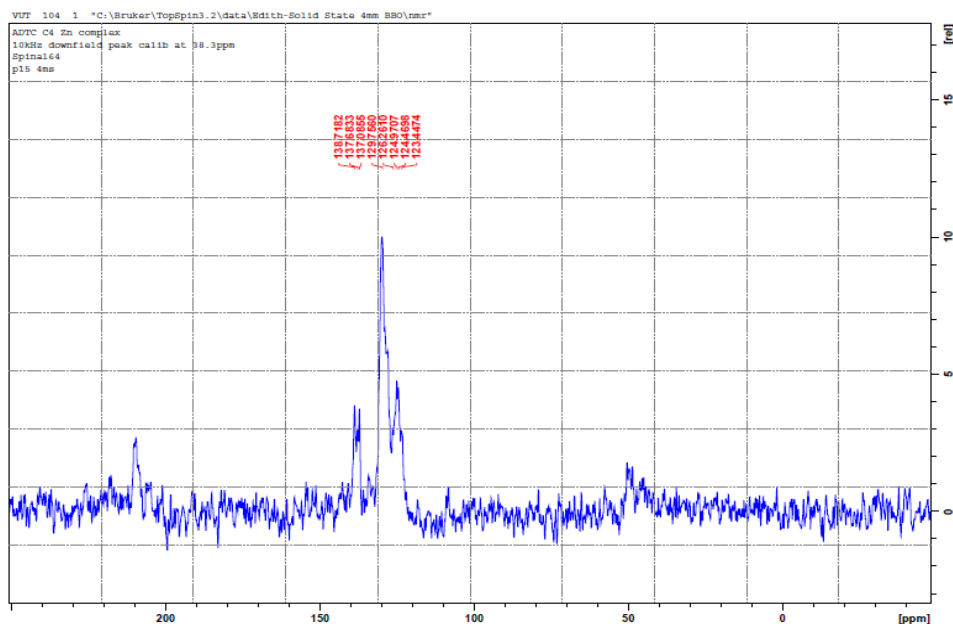


Figure 3.10: NMR spectrum of bis(N-phenyldithiocarbamato)Zn(II) complex (complex 3).

3.2.5 Ammonium pyrrolidine dithiocarbamate ligand (Ligand 3)

The NMR spectrum of APDTC showed distinct signal showing purity. The ligand has three clear signals. The C in the thioureide δ N¹³CS₂ moiety occurred at chemical shift (δ) 202.7 ppm, while the signal of equivalent carbons of the α -CH₂ group bonded directly to nitrogen, these C atoms are deshielded and are downfield relative to the other methylene group at (55.8 ppm). While the upfield β -CH₂ equivalent carbons occurred at 26.0 ppm. This is in agreement with the predicted structure of the ligand and the FTIR spectrum. The summarized results are shown in **Table 5**.

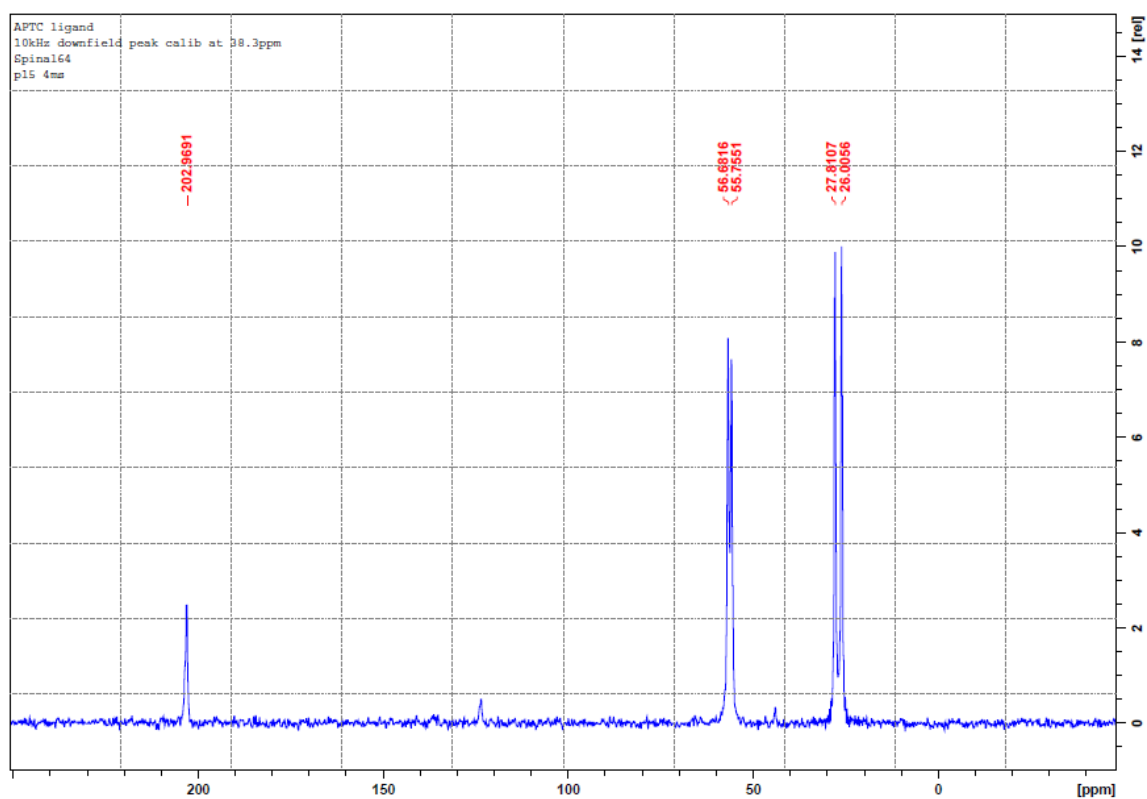


Figure 3.11: NMR spectrum of ammonium pyrrolidine dithiocarbamate (APDTC) ligand

3.2.6. bis(N-pyrrolidinedithiocarbamato)Zn(II) complex (complex 5)

The spectrum in figure 4 reveals the type of bonding in the pyrrolidine-N-dithiocarbamate Zn complex. The carbon in the thioureide ($\delta \text{N}^{13}\text{CS}_2$) moiety signal appeared δ 199 ppm, which had shifted upfield compared to the APDTC ligand and the decrease in intensity relative to the ligand ($\delta \text{N}^{13}\text{CS}_2$) moiety signal. This is due to electron donating ability of the thioureide moiety to the metal ion upon complexation. The equivalent CH_2 group bonded directly to the nitrogen appeared in a range of 55.9-57.6 ppm which was a slight shift from the ligand. The other equivalent CH_2 group occurred at the range of 26.6-27.7 ppm.

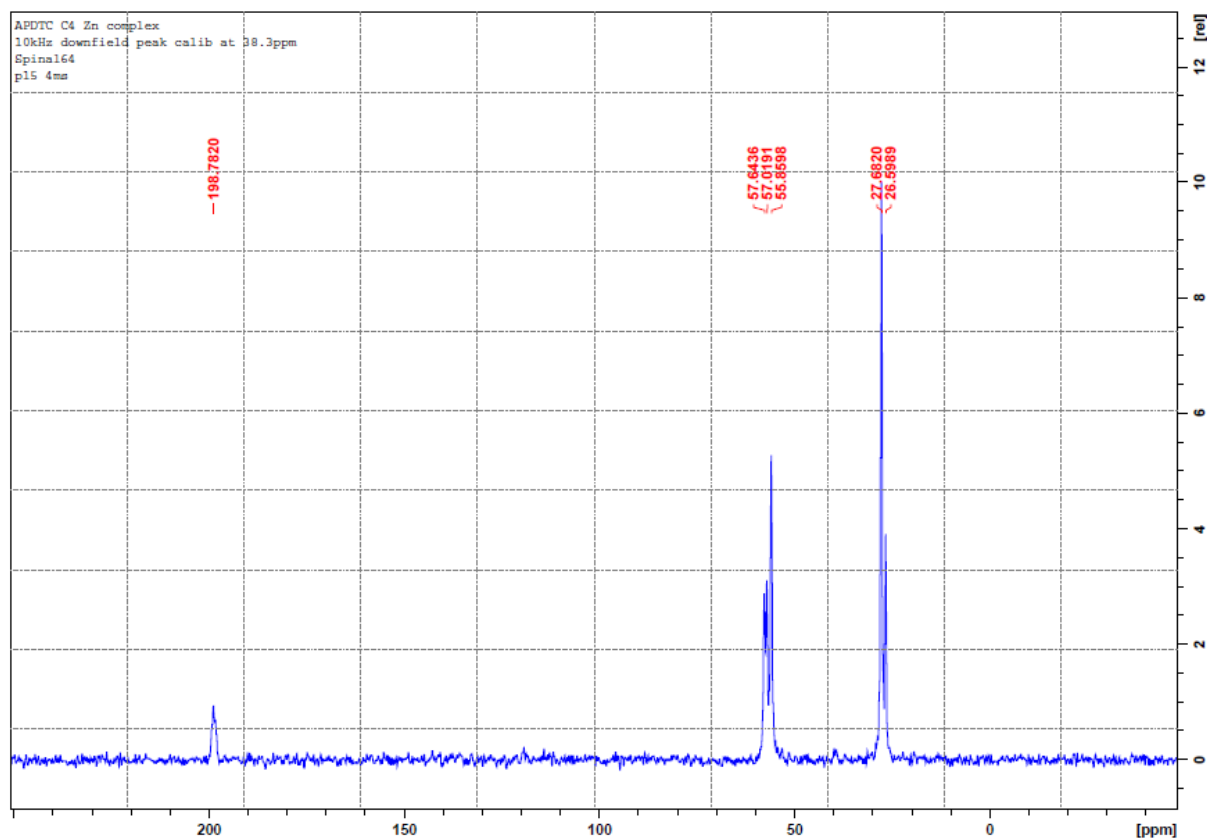


Figure 3.12: NMR spectrum of bis(N-pyrrolidinedithiocarbamato)Zn(II) complex (complex 5).

Table 5: Summarized NMR spectrum signals of ligands and complexes

Compound	Chemical shift δ (ppm)				
	C-N	α -CH ₂	β -CH ₂	γ -CH ₂	CS ₂
Ligand 1	55.8	52.9	25.8	31.7	206.9
Ligand 2	139.4	130.8	126.5	124.5	206.3
Ligand 3		55.8	26		202.7
Complex 1	57.5		25.6	31.3	
Complex 3	137.1	129.7	126.2	123.4	206.1
Complex 5		55.9	26.6		199

The spectroscopic studies of all the prepared samples were in agreement with in terms of coordination of the ligands and complexes via the NCSS moiety. Like the FTIR spectroscopy the trend of the ligands was similar for the NMR spectrum, whereby the ligand with electron donating

properties showed a higher chemical shift value compared to the ligands with electron withdrawing ability (see summarized values in **Table 5**). This shows that the different functional groups attached to the nitrogen atom has an effect on the NCS_2 therefore affecting the complexation as well. There were no specific trends on the complexes on FTIR spectra, but the NMR spectra showed that upon complexation the signals were shifting upfield compared to the downfield ligand chemical shifts.

3.4 Thermal studies of complexes

The thermal behavior of the complexes was studied under a nitrogen atmosphere from 34°C to 900°C. A substantial amount of reports has been based on the thermal analysis of transition metal dithiocarbamates compounds, for both stability and their ability to produce metal sulfide products for the synthesis of nanoparticles (Mamba et al., 2010). It was reported that the metal dithiocarbamates obtained from aliphatic amines decompose to respective metal sulfides involving metal thiocyanate (SCN^-) as the main intermediate while those generated from cyclic amines decomposes in a direct manner without involving the thiocyanate intermediate (Mohammad et al., 2009) and (Yilmaz et al., 2003). In this study the metal center showed an effect on the stability of complexes. While all the final residue of the complexes was metal sulfide except that of complex **3** that gave the final residue that was corresponding to the Zn metal rather than the ZnS that was anticipated. The residues of this compound could be used as precursors for metal sulfide nanoparticles.

3.4.1 Cyclohexylamine complexes

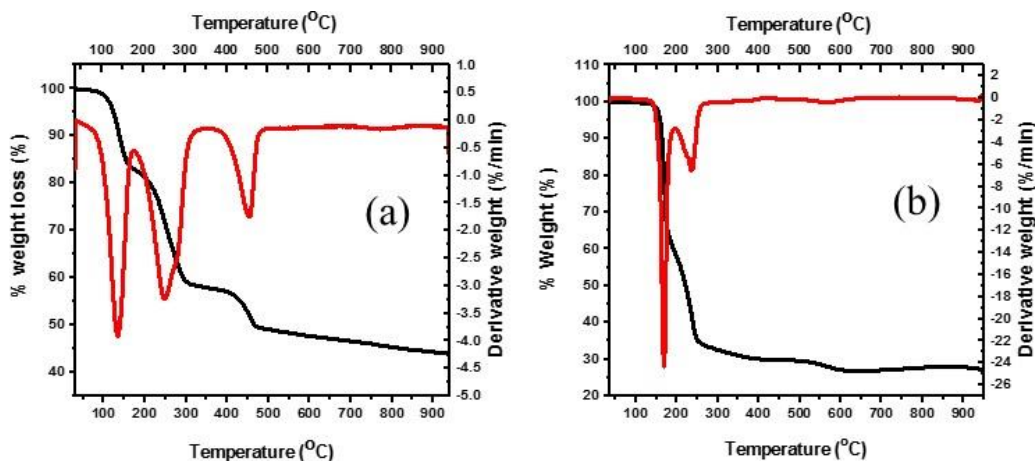


Figure 3.13: TGA and DTA curves of (a) complex 2 and (b) complex 1.

The Figure 3.13 shows degradation of cyclohexylamine DTC Cu complex (complex 2) and cyclohexylamine Zn complex (complex 1). The complex 2 has three decomposition steps, while that of complex 1 has two decomposition steps as seen from the DTA curves. Complex 2 degradation commences with the loss of moisture at the temperature of 100°C. The first decomposition after the loss of moisture was the degradation of thiourea group (SCN) and 1 hydrogen atom as reported previously by (Yilmaz et al., 2003), (Mohammad et al., 2009) and (Mamba et al., 2010) at the temperature range of 100°C-155°C with a % loss of (found: 14.7%, calcd: 14.3%). Then the second decomposition was found at 155°C-296°C which could be attributed to a cyclohexylaminyl group (C₆H₁₂N) (found: 25.01%, calcd: 23.8%). The third and last decomposition started at the temperature range of 296°C-450°C which is attributed to the loss of 1 sulfur (found: 8.9%, calcd: 7.8%). On the other on complex 1, TGA/DTA curve shows that there is no evidence of solvent in the sample since the degradation starts at a higher temperature. The curves show two decomposition steps for this complex, the first decomposition having the greatest % weight loss of 64.4% which starts from 143°C to 252°C. This % weight loss is assigned

to loss of two cyclohexylaminy group and one dithiocarbamate (CS₂) moiety (found: 64.4%, calcd: 65.8%). The final residue is ZnS (found: 27.3%, calcd: 23.1%).

3.4.2 N-phenyldithiocarbamate complexes

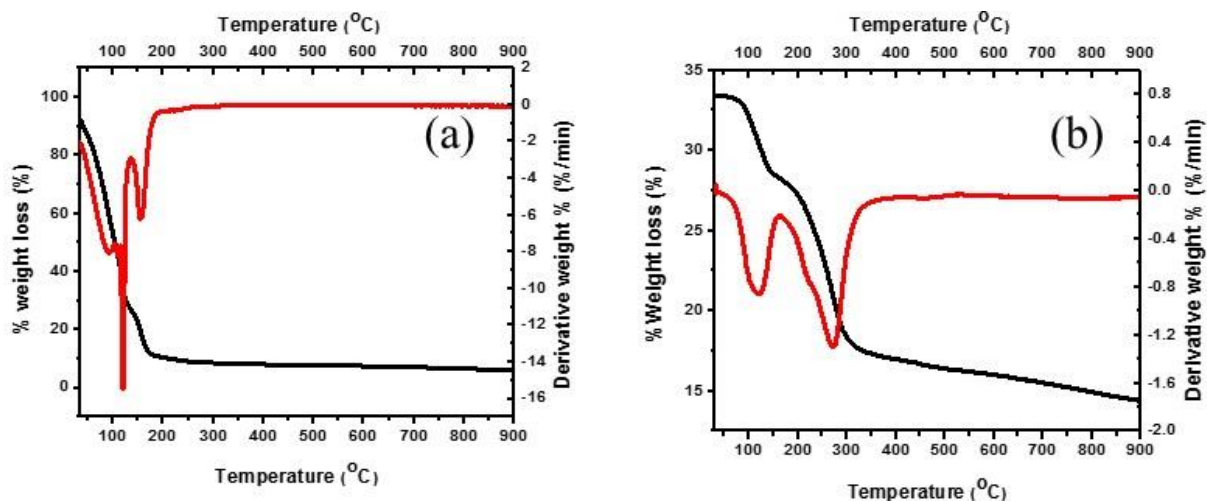


Figure 3.14: TGA and DTA curves of (a) complex 3 and (b) complex 4.

The thermal behavior of the synthesized complex (Zn(adtc)₂) has been studied by thermogravimetric analysis (TGA) and differential thermal analysis (DTA) under a nitrogen atmosphere. The TGA and DTA traces of the Zn(adtc)₂ and Cu(adtc)₂ are shown in Fig.3.14. The TGA shows three decomposition steps; the first decomposition step is the loss of moisture at the temperature of 50°C-100°C. Then the second and third decomposition steps are due to the loss of organic moieties that are present in the complex. The temperatures of those degradations steps are 130°C-150 °C and 150°C-200°C respectively. Then the final residue was calculated to be around 11% which does not correspond with the calculations of ZnS residue since the percentage of ZnS was expected to be around 20.6% as final residue. The final percentage of this complex was close to Zn alone percentage which is 15.8%. On the other hand for the Cu complex the unusual finding

was the very low percentage weight loss, which started at around 34%. The speculation could be that the complex was starting the nucleation process of nanoparticles (showed a black powdered precipitate, which is the same as the nanoparticles), while other organic moieties desorbed from the metal center. The TGA curve in Fig. 3.14 (b) showed that the sample was stable until 100°C then it started to decompose. The complex had two decomposition steps; the first step is due to the loss of moisture from the temperature of 100°C, then the second step is due to the loss of organic moiety such as $[C_6H_5]$ moiety. The temperature of the decomposition ranged from 145°C-287°C. The percentage loss of each step was calculated; the first step had a loss of 6% then the major loss was 10.2% to leave the final residue with 16.8% which corresponded with the theoretical value of 20.3% for CuS (covellite). The stoichiometry of the residue would be further confirmed by the XRD analysis (chapter 4).

3.4.3 N-pyrrolidinedithiocarbamate complexes

The degradation of N-pyrrolidinedithiocarbamate Zn complex and N-pyrrolidinedithiocarbamate Cu complexes in Fig.3.15 (a) and (b) respectively are shown above. The pyrrolidine complexes were the most stable complexes in comparison to the above-described complexes. Both complexes do not show any traces of moisture. Complex **5** showed two decomposition steps, the first decomposition step was the loss of 1 sulfur atom (calcd: 5.5%, found: 8.95%) in the temperature range of 143-187.8°C. The intermediate was the major weight percentage loss 57.6%. The decomposition was the loss of $[C_{10}H_{16}N_2S]$ (calcd: 54.8%, found: 57.6%). Then the final residue was ZnS (calcd: 23.3%, found: 27.2%). While on the other hand complex **6** showed two degradation steps, the first having highest % weight loss. The first decomposition was the loss of $[C_5H_8NS_2]$ (calcd: 41.1%, found: 41.8%). The second decomposition ranged from 297°C -331°C

which was the loss of $[C_5H_8NS]$ (calcd: 32.1%, found: 27.9%). The final residue was found to be CuS (calcd: 23.5%, found: 26.9%).

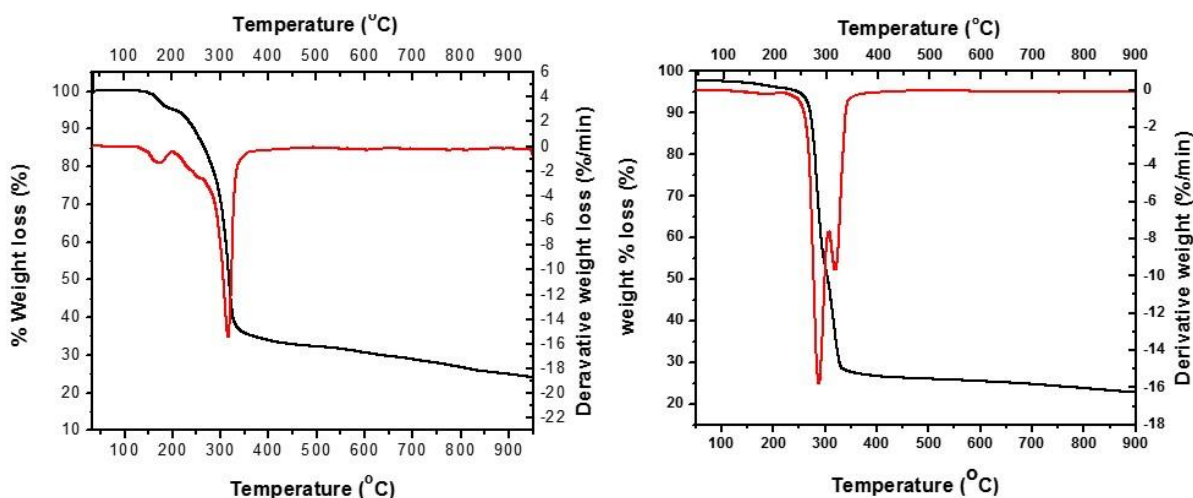


Figure 3.15: TGA and DTA curves of (a) complex 5 and (b) complex 6.

3.5 Conclusion

Spectroscopic studies of the prepared ligands gave an insight on the binding site of the ligand. The IR spectra of all ligands (ligand 1, 2 and 3) showed that the CS_2 moiety bonded through the nitrogen atom of the amine group. The ligands showed C-N and C-S as symmetrical that were intermediates of the single and the double bond of the NCS_2 moiety. Upon complexation these bands were shifting to higher or lower frequency as a result of an increased electron density around the metal ion. The NMR spectra of ligand 2 and complex 3 had the NCS_2 carbon that was so small, that was also not detected by the instrument this was attributed to the resonating electrons between the nitrogen and the carbon of the NCS_2 moiety. And also the fact that the carbon that is not bonded to the hydrogen atom usually has a very small intensity signal that could even not be detected by the instrument in ^{13}C NMR spectral analysis. The FTIR spectra and NMR spectra showed important peaks and signals that were in agreement with the formation of ligands and complexes.

The thermal analysis of all complexes had a final residue that corresponds to metal sulfide product except complex 3 that gave a final residue as the Zn atom instead of ZnS.

3.6 References

- AJIBADE, P.A. & BOTHA, N.L.. 2016. Synthesis and structural studies of copper sulfide nanocrystals. *Results Phys.* 6 pp. 581–589.
- AL-MAYTHALONY, B.A., MONIM-UL-MEHBOOB, M., ALTAF, M., WAZEER, M.I.M., ISAB, A.A., ALTUWAIJRI, S., AHMED, A., DHUNA, V., BHATIA, G., DHUNA, K., ET AL.. 2013. Some new [(thione)₂Au(diamine)]Cl₃ complexes: Synthesis, spectroscopic characterization, computational and in vitro cytotoxic studies. *Spectrochim. Acta - Part A Mol. Biomol. Spectrosc.* **115** pp. 641–647.
- ALTAF, M., MONIM-UL-MEHBOOB, M., ISAB, A. A., DHUNA, V., BHATIA, G., DHUNA, K. & ALTUWAIJRI, S.. 2015. The synthesis, spectroscopic characterization and anticancer activity of new mono and binuclear phosphane-gold(I) dithiocarbamate complexes. *New J. Chem.* **39** (1) pp. 377–385.
- ALVERDI, V., GIOVAGNINI, L., MARZANO, C., SERAGLIA, R., BETTIO, F., SITRAN, S., GRAZIANI, R. & FREGONA, D.. 2004. Characterization studies and cytotoxicity assays of Pt(II) and Pd(II) dithiocarbamate complexes by means of FT-IR, NMR spectroscopy and mass spectrometry. *J. Inorg. Biochem.* **98** (6) pp. 1117–1128.
- ARUL PRAKASAM, B., RAMALINGAM, K., BOCELLI, G. & CANTONI, A.. 2007. NMR and fluorescence spectral studies on bisdithiocarbamates of divalent Zn, Cd and their

- nitrogenous adducts: Single crystal X-ray structure of (1,10-phenanthroline)bis(4-methylpiperazinecarbodithioato) zinc(II). *Polyhedron* **26** (15) pp. 4489–4493.
- BEINROHR, E. & GARAJ, J.. 1980. NMR STUDY OF LIGAND EXCHANGE IN SOME METAL. *Collect. Czechoslov Chem. Commun.* **45** (II) pp. 1785–1792.
- BELLAMY, L.J.. 1980. *The Infrared Spectra of Complex Molecules*. 2ND ED. 11 New Fetter Lane, London EC4P 4EE: Chapman and Hall Ltd.
- CASAS, J.S., SÁNCHEZ, A., BRAVO, J., GARCÍA-FONTÁN, S., CASTELLANO, E.E. & JONES, M.M.. 1989. Cadmium coordination chemistry related to chelate therapy. *Inorganica Chim. Acta* **158** (1) pp. 119–126.
- CHATT, J., DUNCANSON, L.A. & VENANZI, L.M.. 1956. Electronic Structures of Dithiocarbamates and Xanthates. *Nature* **177** pp. 1042–1043.
- FARAGLIA, G., SITRAN, S. & MONTAGNER, D.. 2005. Pyrrolidine dithiocarbamates of Pd(II). *Inorganica Chim. Acta* **358** (4) pp. 971–980.
- VAN GAAL, H.L.M., DIESVELD, J.W., PIJERS, F.W. & VAN DER LINDEN, J.G.M.. 1979. ¹³C NMR Spectra of Dithiocarbamates. Chemical Shifts, Carbon-Nitrogen Stretching Vibration Frequencies, and P Bonding in the NCS₂ Fragment. *Inorg. Chem.* **18** (11) pp. 3251–3260.
- GANDHI, N., JAIN, R. & KAUSHIK, N.K.. 1996. thermochimica acta Thermal studies on germanium (IV) complexes of dithiocarbamates '. *Thermochim. Acta* **283** pp. 501–508.
- HALLS, D.J.. 1969. The properties of dithiocarbamates A Review. *Mikrochim. Acta* **57** (1) pp. 62–77.
- JANES, R. & MOORE, E.. 2004. *Metal-Ligand Bonding*. 1st ed. Janes, R. & E. Moore, eds. Milton

Keynes MK7 6ZS, United Kingdom: The Open University.

JAYARAJU, A, MUSTHAK AHAMAD, M., MALLIKARJUNA RAO, R. & SREERAMULU, J.. 2012.

Synthesis, characterization and biological evaluation of novel dithiocarbamate metal complexes. *Der Pharma Chem.* **4** (3) pp. 1191–1194.

JIAN, F., WANG, Z., BAI, Z., YOU, X., FUN, H., CHINNAKALI, K. & RAZAK, I.A.. 1999. The crystal

structure, equilibrium and spectroscopic studies of bis(dialkyldithiocarbamate) copper(II) complexes $[\text{Cu}_2(\text{R}_2\text{dtc})_4]$ (dtc=dithiocarbamate). *Polyhedron* **18** (26) pp. 3401–3406.

KAUL, B.B. & PANDEYA, K.B.. 1979. N-Monoaryldithiocarbamate Cobalt (III) Complexes (a).

Transition. Met. Chem. **4** pp. 112–114.

MAMBA, S.M., MISHRA, A.K., MAMBA, B.B., NJOBEH, P.B., DUTTON, M.F. & FOSSO-KANKEU, E..

2010. Spectrochimica Acta Part A : Molecular and Biomolecular Spectroscopy Spectral, thermal and in vitro antimicrobial studies of cyclohexylamine- N -dithiocarbamate transition metal complexes. *Spectrochim. Acta Part A Mol. Biomol. Spectrosc.* **77** (3) pp. 579–587.

MANAV, N., MISHRA, A.K. & KAUSHIK, N.K.. 2004. Triphenylphosphine adducts of platinum(IV)

and palladium(II) dithiocarbamates complexes: A spectral and in vitro study. *Spectrochim. Acta - Part A Mol. Biomol. Spectrosc.* **60** (13) pp. 3087–3092.

MANAV, N., MISHRA, A. K. & KAUSHIK, N.K.. 2006. In vitro antitumor and antibacterial studies

of some Pt(IV) dithiocarbamate complexes. *Spectrochim. Acta - Part A Mol. Biomol. Spectrosc.* **65** (1) pp. 32–35.

MOHAMMAD, A., VARSHNEY, C. & NAMI, S.A.A.. 2009. Synthesis, characterization and

- antifungal activities of 3d-transition metal complexes of 1-acetylpiperazinyldithiocarbamate, $M(acpdtc)_2$. *Spectrochim. Acta - Part A Mol. Biomol. Spectrosc.* **73** (1) pp. 20–24.
- NABIPOUR, H., GHAMMAMY, S. & RAHMANI, A.. 2011. Synthesis of a new dithiocarbamate cobalt complex and its nanoparticles with the study of their biological properties. *Int. J. Nano Dimens.* **6** (3) p. 217.
- RAY, A. & SATHYANARAYANA, D.N.. 1973. Spectroscopic and coordination behavior of α -cyanothioacetamide. *Bull. Chem. Soc. Jpn.* **46** pp. 1969–1972.
- WANG, X. & GUO, Z.. 2008. Towards the rational design of platinum(II) and gold(III) complexes as antitumor agents. *Dalt. Trans.* (12) pp. 1521–1532.
- WORKMAN, J. & WEYER, L.. 2007. *Practical Guide to Interpretive Near-Infrared Spectroscopy*.
WORKMAN, J. & L. WEYER, EDS. 6000 Broken Sound Parkway NW, Suite 300 Boca Raton, FL 33487, USA: © 2008 by Taylor & Francis Group, LLC.
- YILMAZ, V.T., YAZICILAR, T.K., CESUR, H., OZKANCA, R. & MARAS, F.Z.. 2003. Metal complexes of phenylpiperazine-based dithiocarbamate ligands. Synthesis, characterization, spectroscopic, thermal, and antimicrobial activity studies. *Synth. React. Inorg. Met. Chem.* **33** (4) pp. 589–605.

Chapter 4

Characterization of metal sulfide (capped) nanoparticles

4.1 Introduction

The use of dithiocarbamate complexes as a precursor for the synthesis of metal sulfide nanoparticles has grown substantial interest over the years (Ajibade & Osuntokun, 2014). The growth of this precursor is mainly due to a two sulfur atom, and also the nitrogen backbone in its structure which make the DTC's versatile for stabilizing different oxidation states (Hogarth, 2012; Coffey et al., 1993; Knight et al., 2009). The stability of the metal complexes could be manipulated by thermolysis of the precursor compound to form stable and high-quality metal sulfide nanoparticles. The quality of the synthesized nanoparticles not only depends on the type of precursor used but also the capping agent (surfactant) used and other parameters such as time, and temperature (Oluwafemi et al., 2016). Surfactants also are known as capping agents are mainly used for two purposes, the first being its main purpose, which is to solubilize and disperse the nanocrystals and the reactants involved in the growth. The second is to control the speed of the reaction. In order for that, the solvent molecules need to bind and unbind dynamically on the surface of the growing crystals. Once a molecule detaches from the surface of the nanocrystal, monomers can be incorporated into the nanocrystal, making the crystal grow. Therefore surfactants can be used to control the shape and size of the nanocrystals, by variation of the alkyl group attached and also the polar and non-polar heads that are on the surfactant. The polar head group affects the binding efficiency of the material (binding on the surface of the nanocrystal), while the non-polar part affects the diffusion properties of the material (Sanghamitra & Mazumdar, 2008).

In this work DTC complexes, capping agents and amount/concentration of the capping molecule were investigated in the formation of metal sulfide nanoparticles. The capping agents used in this study are hexadecylamine (HDA) and tri-octyl-n-phosphine oxide (TOPO). They affect the formation of nanoparticles in different ways, since they contain different binding sites to bind to the surface of the nanoparticles. HDA contains amine group of which uses the nitrogen atom to adsorb on the nanocrystal, while TOPO binds via its phosphorus-oxygen bond. Depending on the head group of the ligand molecule they can have different types of bindings. They can bind via attractive interactions, such as chemisorption, electrostatic attraction or hydrophobic interaction (Sperling & Parak, 2010). The capping agents help to reduce the surface energy by blocking dangling bonds on the surface of the nanoparticles and by doing that, they decrease aggregation of the particles (Sanjay & Pandey, 2016). They also affect the optical properties, by either enhancing or altering the optical properties by creating surface defects (trap states) that alter the optical properties causing red-shifted particles.

Then the choice of the Zn and Cu metals in the synthesis of this metal sulphide nanoparticles, is based on their non-toxic nature in comparison to Pb, Cd and other metal sulphide nanoparticles. Further a specific reason for the synthesis of CuS nanoparticles is that they possess plasmonic behaviour that are superior to those of the noble metal nanoparticles as reported on literature, thus making them an ideal nanoparticles for more advanced applications in diverse fields of science (Luther et al., 2011).

4.2 Results and discussion

The characterization techniques show that the CuS nanoparticles synthesized were well passivated with an increase in concentration of capping agent favoring a decrease in particles/polydispersity

as seen from the TEM micrographs. The XRD patterns revealed the synthesis of hexagonal phase covellite CuS particles. On the other hand the absorption spectra of all the synthesized copper sulfide particles showed plasmonic behavior by showing an emergence of a peak in the near-IR region. The emission spectra were in agreement with the TEM micrographs showing that a decrease in particle dispersity was improved with an increase in capping concentration for samples prepared in HDA. The opposite was obtained for the TOPO-capped CuS nanoparticles. The ZnS nanoparticles showed crystal fringes in most of the samples except that of the sample prepared from complex **1**. The crystal phase obtained was confirmed by XRD analysis with the Miller indices corresponding to ZnS blend sphalerite phase for most of the TOPO-capped ZnS particles. Most of the HDA-capped ZnS gave the hexagonal phase (wurtzite). The TEM image results did not show any trend in the formation of the lattice fringes, but HDA-capped ZnS prepared from complex **3**, showed a trend that as the capping concentration was increased sudden change in shape from the concentric spherical shape to rod-like elongated fringes occurred. The fringes were connected with very small nanoparticles that were aligned in the direction of the fringes.

4.2.1 Copper sulfide nanoparticles

4.2.1.1 Optical properties

Copper sulfide is a semiconductor with two types of band gaps depending on the stoichiometry of the quantum dots synthesized. The bandgap variation of copper sulfide makes this material very unique due to variation in stoichiometries associated with the bandgap type for different applications across different fields of study. Most of the application of nanomaterials are based on their optical properties, thus making a study of optical properties very fundamental in understanding the behavior of nanomaterials. The change in the size of the nanoparticles can be observed by the

optical properties via a shift towards higher energy (blue-shift) or lower energy (red-shift) in the absorption spectra. A blue-shift is associated with the decrease in particle size due to a quantum size effect, while the red-shift is associated with the increase in particles size which could be caused by aggregation of particles or the large size of the synthesized material. The principle behind the blue-shift comes from the “quantum mechanics particle in a box” (Revaprasadu & Mlondo, 2006).

In bulk semiconductors the valence band and conduction band are separated by a band gap; the gap is very small in the bulk material. The excitation of electron results in the promotion of electrons from the valence to the conduction band, and holes are created in the valence band. The charge carriers (electrons and holes) are separated by a distance that is known as the Bohr radius that normally has dimensions on the nanometer scale (Kent & Riegel, 2012). When the size of the semiconductor material itself becomes similar to the Bohr radius or smaller, it leads to a situation in which the electrons and hole (excitons) have a restricted space or volume to move and thus their motion is confined in all three dimensions (Kent & Riegel, 2012) and (Revaprasadu & Mlondo, 2006). Like the “electron in a box” phenomena, the kinetic energy and the excitation energy of the electron increase as the size of the box decreases. Similarly, the band gap of the semiconductor increases as the size of the particles becomes smaller than their Bohr radius, leading to the blue-shift in the absorption spectra (Kent & Riegel, 2012). The decrease in particle size does not only affect the absorption spectra. The emission spectra is also affected because a change in the band gap means the change in color and emission of the nanoparticles. In this study the interesting or phenomena other than the quantum size effect on the copper sulfide nanoparticles is the emergence of the near-IR band which is the characteristic of the electron deficient Cu_{2-x}S nanoparticles (Luther et al., 2011; Dorfs et al., 2011). The emergence of the near-IR band shows the plasmonic

behavior of the synthesized materials. The SPR was fully explained in chapter 1. The results of CuS nanoparticles are summarized in **Table 6**, while **Table 7** summarized the ZnS nanoparticle results

4.2.1.1.1 Cu_{2-x}S nanoparticles from Complex 2

4.2.1.1.1 (I) UV-vis spectral analyses of HDA-capped nanoparticles

UV-vis absorption spectra of the Cu_{2-x}S nanoparticles synthesized in 3 g and 6 g HDA are shown in Fig. 4.1 (a) and (b) respectively. The absorption and the Tauc plot spectra of the synthesized materials gave the short-wavelength localized surface plasmon resonance (SWLSPR) absorption edge of 2.32 eV (534 nm) and 2.29 eV (541 nm) for copper sulfide nanoparticles synthesized with 3 g and 6 g HDA respectively. The absorption edges were both blue shifted from bulk CuS (1022 nm) which indicates a quantum confinement effect for both samples. The spectra also suggested that there was an increase in particle size with an increase in capping concentration. The CuS spectra for both samples shows two absorption peaks in the visible region and the emergence of another peak in the near-infrared region which is characteristic of copper sulfide nanoparticles. These two absorption peaks are due to a surface plasmon resonance in the transverse (SWLSPR) and longitudinal (LWSPR) regions. These surface plasmon resonances are due to free carrier charges in the Cu²⁺ metal due to self-doping of the electron deficient Cu_{2-x}S nanoparticles (Luther et al., 2011; Dorfs et al., 2011; Chen et al., 2015).

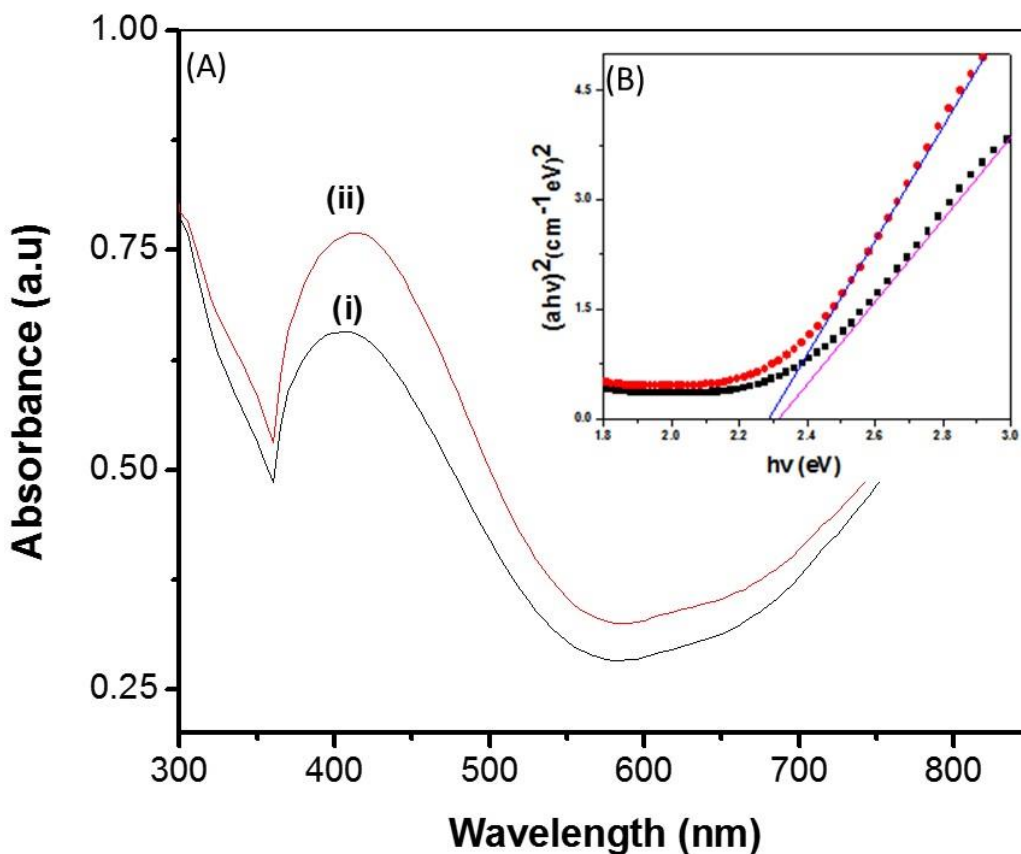


Figure 4.2: Absorption spectra of Cu_{2-x}S nanoparticles in [A] (i) 3 g-HDA and (ii) 6 g-HDA, [B] (inset Tauc plot)

4.2.1.1.1 (II) Photoluminescence spectral analyses of HDA-capped nanoparticles

The emission spectra of Cu_{2-x}S is presented in Fig 4.2 (a) and (b) for nanoparticles prepared in 3 g and 6 g HDA respectively. The sample prepared in 3 g HDA had an emission maximum at 400 nm and that prepared with 6 g HDA at 378 nm as shown in Fig. 4.2 (a) and 4.2 (b) respectively. The spectrum of the nanoparticles prepared with 3 g HDA was more red shifted and broader compared to that of the nanoparticles prepared with 6 g HDA indicating a larger particle size distribution.

The nanoparticles prepared in 6 g HDA has a narrow emission spectrum which indicates narrower particles distribution or monodispersity. These results were further confirmed by TEM images (see **Table 6** for summarized results).

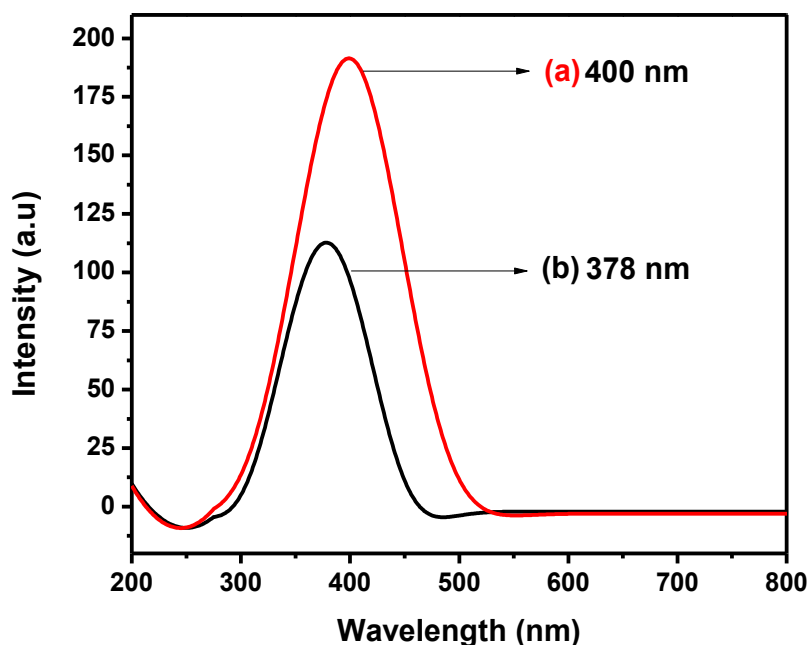


Figure 4.3: Emission spectra of Cu_{2-x}S nanoparticles in (a) 3 g-HDA and (b) 6 g-HDA.

4.2.1.1.1 (III) UV-vis spectral analyses of TOPO-capped nanoparticles

The absorption spectra of Cu_{2-x}S nanoparticles prepared in 3 g and 6 g TOPO are presented in Fig. 4.3. The absorption spectra of the TOPO-capped samples were almost similar to those of the HDA-capped samples. They both showed quantum size effect by showing blue-shifted spectra of 2.38 eV (521 nm) and 2.47 eV (502 nm) for Fig. 4.3 (i) and 4.3 (ii) respectively. The blue-shift indicates the formation of smaller particles. The other similar property between the two spectra was the

localized surface plasmon resonance behavior which is the most noticeable function of electron deficient Cu_{2-x}S nanoparticles due to free charge carriers in the valence band of the Cu_{2-x}S nanoparticles (Luther et al., 2011; Hsu et al., 2011; Liu et al., 2013; Faucheaux et al., 2014; Niezgoda & Rosenthal, 2016). In comparison to the absorption of the HDA-capped nanoparticles, the absorption spectra of the TOPO-capped Cu complex were revealed an excitonic peak of the SWLSPR, which might possibly arise from a charge transfer of the surface ligand (TOPO) on plasmon a resonance (Kim et al., 2013). This was further confirmed by the XRD analysis which showed an amorphous peak in some diffraction peaks due to the charge transfer in the surface of the nanoparticles.

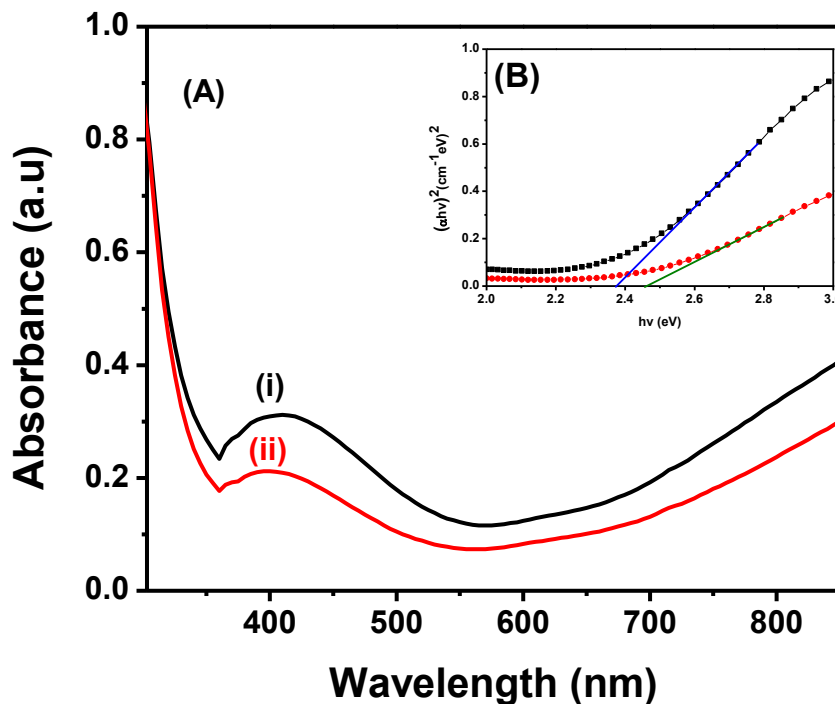


Figure 4.4: Absorption spectra of Cu_{2-x}S nanoparticles in [A] (i) 3 g-TOPO and (ii) 6 g-TOPO, [B] Inset Tauc plot of the prepared nanoparticles.

4.2.1.1.1 (IV) Photoluminescence spectral analyses of TOPO-capped nanoparticles

The emission spectra of the prepared nanoparticles are shown in Fig. 4.4 (a) and 4.4 (b) for samples prepared in 3 g and 6 g TOPO respectively. The broader emission peak in Fig. 4.4 (a) indicates polydispersity and the narrower peak in Fig. 4.4 (b) indicates monodispersity in the prepared nanomaterial. The emission maximum slightly increased with an increase in capping concentration from 411 nm in Fig. 4.4 (a) to 413 nm in Fig. 4.4 (b) which is an inverse for the samples prepared in HDA. **Table 6** summarizes the obtained results.

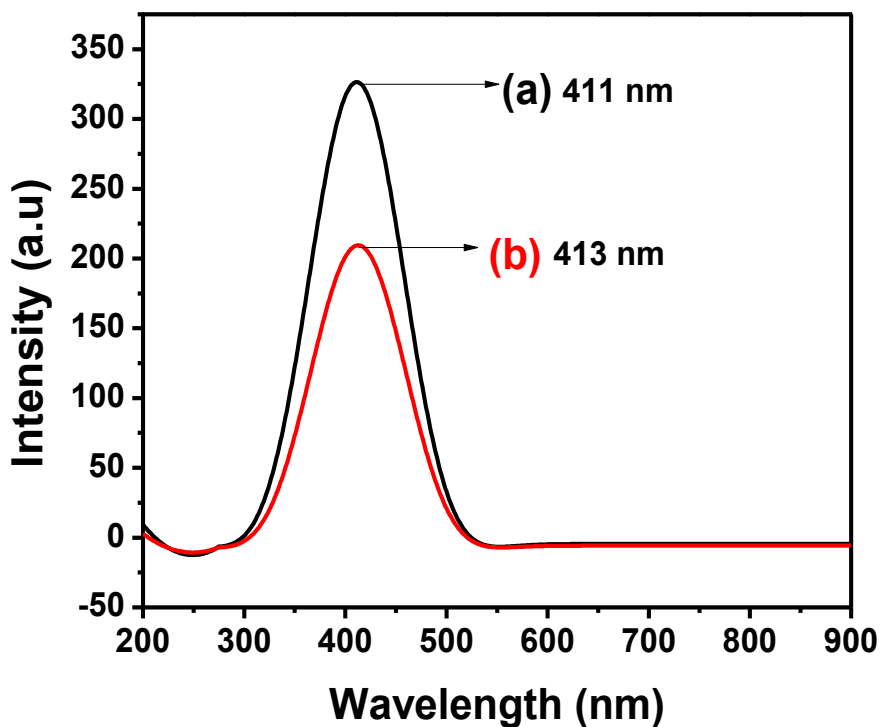


Figure 4.5: Emission spectra of Cu_{2-x}S nanoparticles in (a) 3g-TOPO and (b) 6g-TOPO.

4.2.1.2 Powder X-ray diffraction analysis

The XRD pattern is important in understanding the crystallinity of the prepared nanoparticles and the phase that is formed. The analysis can also help in revealing the impurities present in a sample. XRD is also used to determine the dimension of the nanoparticle using the Debye Scherrer equation. The broadening of the crystal peaks is associated with a decrease in particle size, while the narrowing of the peaks is associated with an increase in particles size. In this study, the XRD showed that all the prepared samples were indexed to the electron deficient hexagonal phase CuS (covellite) nanoparticles. The obtained stoichiometry (or phase) was in good agreement with TGA analysis that gave CuS as final residue for all the prepared copper sulfide complexes.

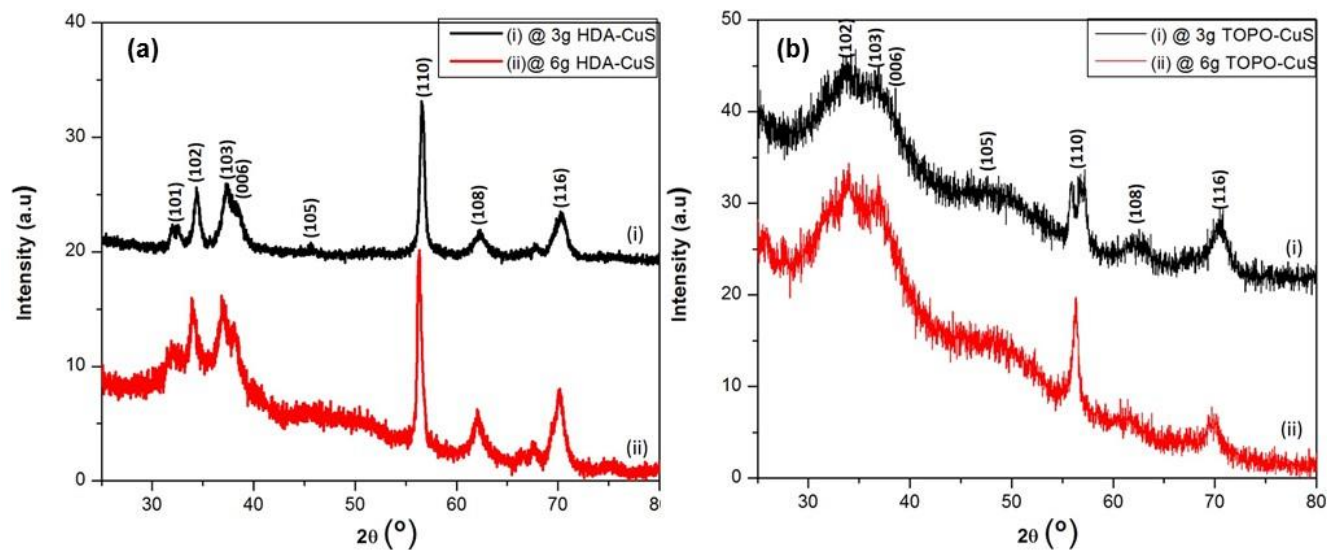


Figure 4.6: XRD patterns of CuS nanoparticles synthesized in (a) HDA and (b) TOPO.

The XRD patterns of the synthesized particles are shown in Fig. 4.5(a) and (b) for CuS nanoparticles prepared in HDA and TOPO. The samples synthesized in HDA in Fig. 4(a) showed

a pure CuS (covellite). The diffraction peaks were indexed to hexagonal phase CuS (JCPD card no. 03-065-3561). The prepared samples showed that as the capping concentration was increased there was a broadening of the peaks which suggest a decrease in particle size (**Table 6** for crystal sizes). The TOPO-capped particles Fig. 4(b) were also indexed to hexagonal phase CuS. TOPO-capped nanoparticles reveal an amorphous-like pattern which is an indication of lower crystallinity that was also observed from the absorption spectra by the unraveling of the SWLSPR that was ascribed to charge transfer of the ligand to the surface of the nanoparticles. An increase in capping concentration, showed a little increase in crystallinity as observed by the appearance of the sharp peak corresponding to 110 in Fig. 4(b) (ii).

4.2.1.3 Transmission electron microscopy (TEM) images

The TEM images of CuS nanoparticles synthesized in different concentrations of HDA and TOPO from the copper complex are shown in Fig. 4.6. The nanoparticles prepared in 3 g HDA (Fig. 4.6(a)) had different shapes and sizes. This is in agreement with the results obtained from the emission spectra which showed a broad peak indicating polydispersity. Fig. 4.6(a) did not only show polydispersity but it also showed a high degree of agglomeration which might be due to a high surface energy due to the lack of good passivation from the capping molecule, thus resulting in dangling bonds on the surface of the nanoparticles. Fig. 4.6(b) was in good agreement with the narrower emission spectra in the PL results, the TEM images showed a lower degree of polydispersity of synthesized nanoparticles compared to Fig. 4.6(a). The size also decreased with an increase in capping agent concentration and there were no signs of aggregation. These well-passivated particles were mainly dominated by sphere-like particles, with few triangular and hexagonal shaped particles and the average size was 14.1 nm. The TOPO-capped particles were

well passivated in both samples but an increase in capping concentration in Fig. 4.6(c) brought about an increase in polydispersity and an emergence of a few rod-like shape and triangular-like shape (indicated by arrow) particles as shown in Fig. 4.6(d). This was opposite to samples prepared in HDA. The average particles sizes for the prepared TOPO-capped samples was found to be 12.1 and 13.2 nm for Fig. 4.6(c) and (d) respectively.

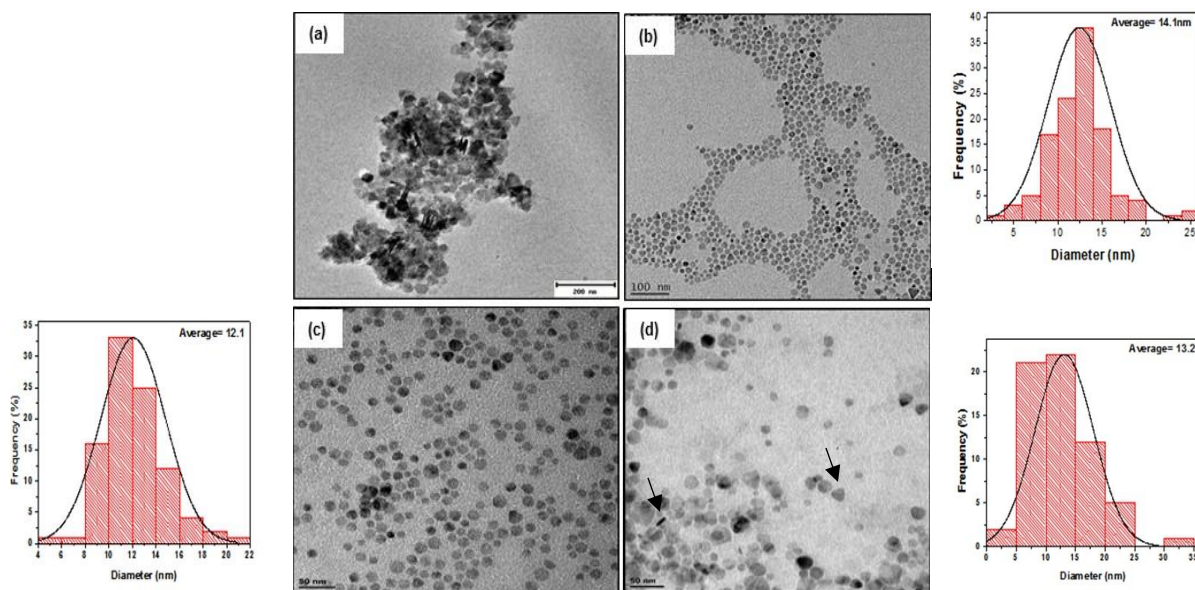


Figure 4.7: TEM images and histograms of CuS nanoparticles prepared in (a) 3 g HDA, (b) 6 g HDA, (c) 3 g TOPO and (d) 6 g TOPO.

4.2.1.1.2 Cu_{2-x}S nanoparticles prepared from Complex 4

4.2.1.1.2.1 (I) UV-vis spectral analyses of HDA-capped nanoparticles

The HDA-capped Cu_{2-x}S absorption spectrum synthesized from bis(N-phenyldithiocarbamato) Cu(II) complex is shown in Fig. 4.7. The same trend for the nanoparticles prepared from the cyclohexylamine Cu complex (complex 2) was observed showing the plasmonic behavior of the

prepared particles. The plasmonic behavior indicates an electron deficient (since copper has copper poor and copper rich stoichiometries) copper sulfide stoichiometry that was confirmed by XRD analysis, while the blue-shifted band edge energy observed from the Tauc plot suggests a formation of small size nanoparticles due to quantum size effects of the prepared nanoparticles. Fig. 4.7(a) gave a band edge energy of 2.19 eV corresponding to the wavelength of 566 nm, while the blue-shift from the higher concentration was observed in Fig. 4.7(b) with band edge energy of 2.30 eV correspond to the 539 nm peak. The increase in capping concentration resulted in an increase in band edge energy, indicating a decrease in particle size. This is also evident from the TEM images. (See below)

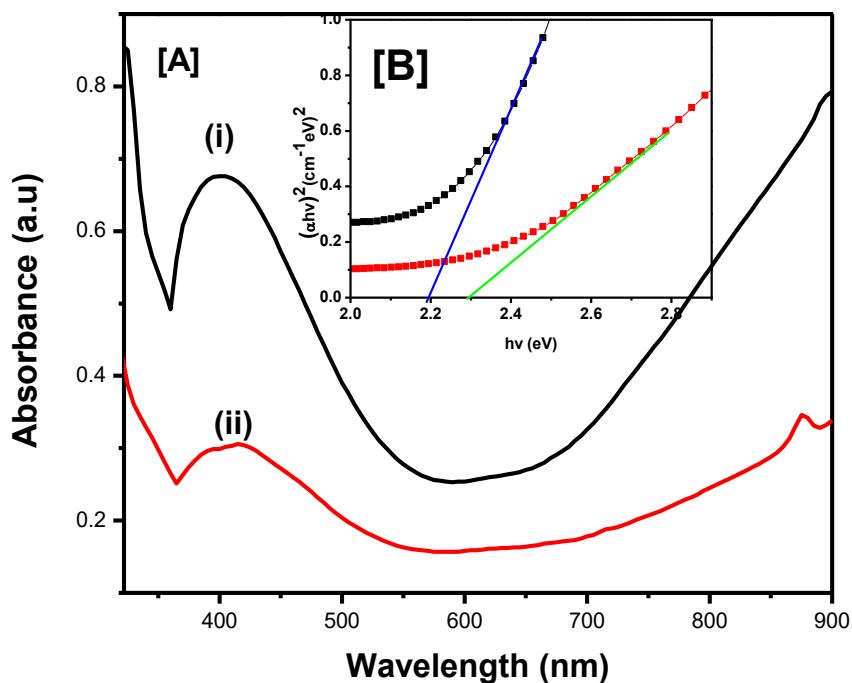


Figure 4.8: Absorption spectra of Cu_{2-x}S nanoparticles in [A] (i) 3 g-HDA and (ii) 6 g-HDA, [B] (inset Tauc plot)

4.2.1.1.2.1 (II) PL spectral analyses of HDA-capped nanoparticles

The emission spectra of copper sulfide nanoparticles prepared with different concentrations of HDA is presented in Fig. 4.8. The broadness of the emission spectra was almost identical but in comparison to the samples from cyclohexylamine DTC complex (complex **2**), suggesting they were polydispersed. The increase in capping concentration resulted in a decrease in wavelength, which was in good agreement with the absorption spectra. The decrease in wavelength suggests a reduction in particle size with an increase in capping concentration. The emission maximum were found to be at 413 and 396 nm respectively for Fig. 4.8(a) and (b).

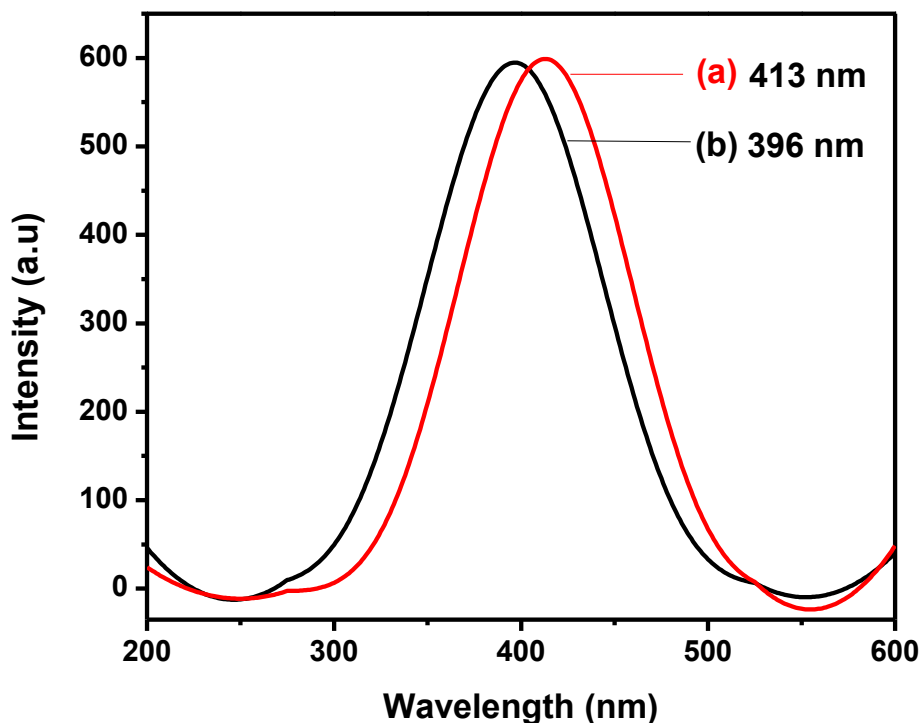


Figure 4.9: Emission spectra of Cu_{2-x}S nanoparticles in (a) 3 g-HDA and (b) 6 g-HDA.

4.2.1.1.2.1 (III) UV-vis spectral analyses of TOPO-capped nanoparticles

The excitonic peaks observed in both samples showed that the increase in capping molecule concentration had an effect on the band edge as observed in the Tauc plot inset, since the band edge energy increased with an increase in capping concentration. This thus suggests a decrease in particle size. The band edge energy was found to be 1.96 eV (633 nm) and 2.37 eV (523 nm) for Fig. 4.9 (a) and (b) respectively. Both samples were blue-shifted from bulk copper sulfide 1022 nm, due to a quantum size effect associated with the prepared nanoparticles. The spectrum was red-shifted in comparison to the TOPO-capped nanoparticles synthesized from complex **2**. (See **Table 6** for summarized results)

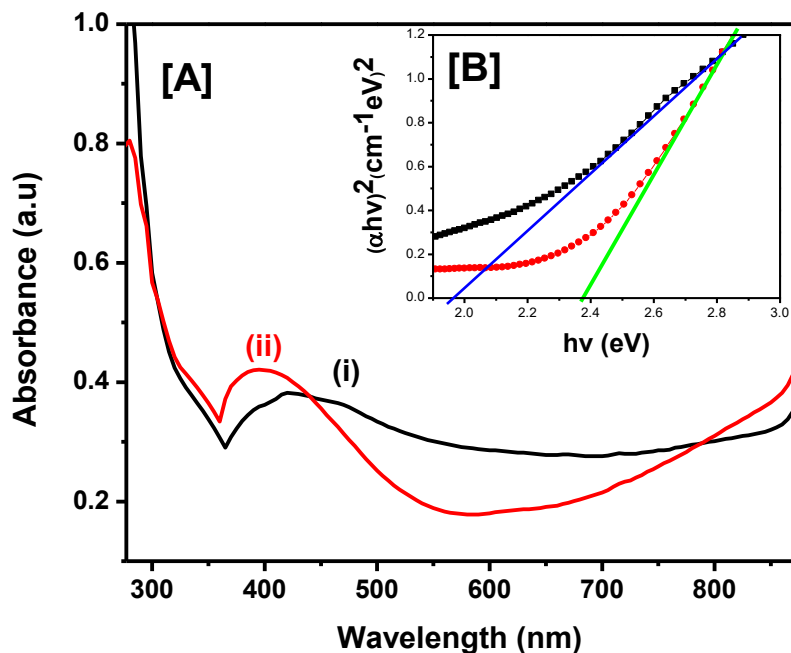


Figure 4.10: Absorption spectra of Cu_{2-x}S nanoparticles in [A] (i) 3g-TOPO and (ii) 6g-TOPO, [B] (inset Tauc plot)

4.2.1.1.2.1 (IV) PL spectral analyses of TOPO-capped nanoparticles

The emission spectra of the samples prepared at two TOPO concentrations are given in Fig. 4.10(a-b). Their FWHM of the emission peaks were 96.5 and 100.8 for samples prepared with 3 g and 6 g TOPO respectively. Suggesting increase in polydispersity with increase in capping concentration. Unlike the HDA-capped nanoparticles emission spectra, the TOPO-capped nanoparticles showed a slight increase in emission maximum with an increase in capping concentration. The emission data are in contrast to the absorption findings which suggested a decrease in wavelength number with an increase in capping concentration. This could be due to surface irregularities or surface defects. The emission maximum was found to be at 398 and 401 nm for samples prepared in Fig. 4.10(a) and (b) respectively.

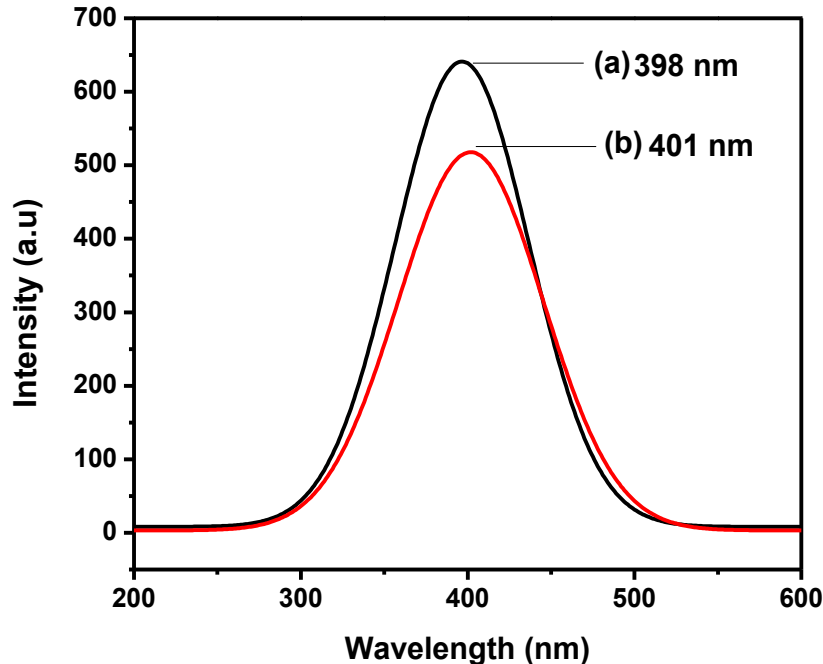


Figure 4.11: Emission spectra of Cu_{2-x}S nanoparticles in (a) 3g-TOPO and (b) 6g-TOPO

4.2.1.1.2.2 Powder X-ray diffraction

The crystal structure of HDA and TOPO capped copper sulfide nanoparticles was studied (Fig. 4.11). Fig. 4.11 (a) presents the HDA capped nanoparticles, while Fig. 4.11 (b) shows that are capped in TOPO. HDA-capped nanoparticles were indexed to pure hexagonal phase CuS (covellite) stoichiometry with JCPDS card no. of 03-065-3556. The broadness of the peaks were almost identical but with Fig. 4.11(a) (ii) showing broader peaks compared to Fig. 4.11(a) (i) (see **Table 6** for crystal sizes). The broadness of the peaks is indirectly proportional to the size/diameter of the particles from the Scherrer's equation, thus indicating smaller particle size in the prepared nanoparticles. The crystallinity of the HDA capped nanoparticles was increased with an increase in capping concentration.

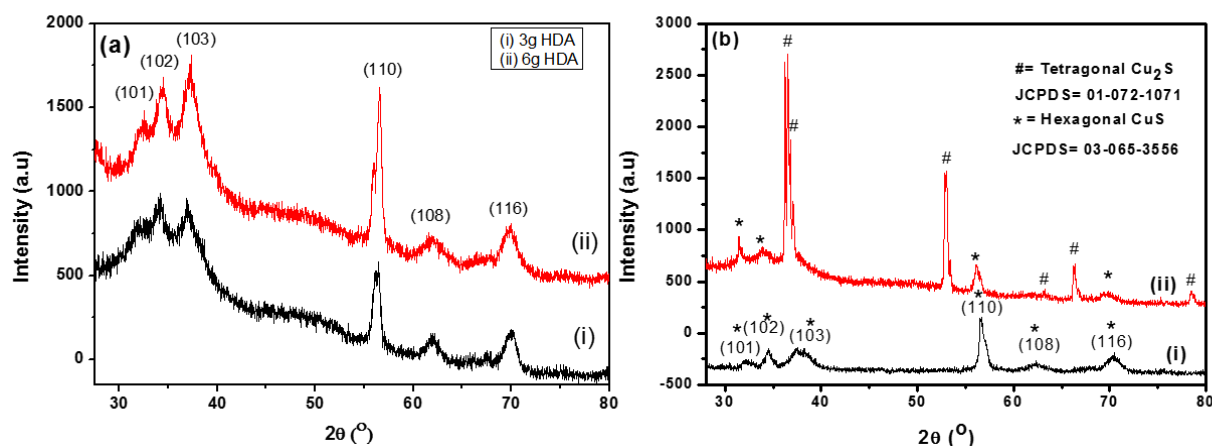


Figure 4.12: XRD patterns of CuS nanoparticles synthesized in (a) (i) 3 g HDA, (ii) 6 g HDA and (b) (i) 3 g TOPO, (ii) 6 g TOPO.

The TOPO capped nanoparticles had similar stoichiometry and phase (hexagonal phase CuS covellite) as found for the HDA-capped nanoparticles at a lower capping concentration. The increase in concentration of the TOPO capping agent saw an evolution of copper sulfide chalcocite (Cu_2S) stoichiometry, with other peaks correlating to the hexagonal phase CuS. The sudden rise of chalcocite could be attributed to the orientation of the capping molecule to the surface of the nanoparticles as the capping was increased to a higher concentration, which could thus lead to the morphology evolution of the prepared nanoparticles (Lee et al., 2005; Li et al., 2011). The stoichiometry showed narrower peaks while the covellite peaks were broader. This means that as predicted from the emission spectra, the polydispersity could be observed in the nanoparticles prepared in Fig. 4.11(b) (ii). (See TEM images for confirmation)

4.2.1.1.2.3 Transmission electron microscopy (TEM images)

HDA and TOPO capped copper sulfide nanoparticles are presented in Fig. 4.12. The HDA-capped nanoparticles prepared in Fig. 4.12(a) were very well dispersed showing good passivation at lower concentrations. The particles had few big particles that are shown by TEM images ranging from 70-80 nm with hexagonal and triangular shaped particles. Spherical shaped gave an average particle size of 19.4 nm. The increase in HDA concentration gave nanoparticle with a mixed morphologies, with the spherical shape being the dominant shape as well. This spherical shape was embedded in bigger triangular and almost hexagonal shaped nanoparticles. On the other hand the TOPO-capped particles showed a similar trend as the particles prepared from HDA. The TOPO capped particles at lower concentration were better passivated than their higher concentration counterpart. The average particle size of Fig. 4.12(c) was found to be 14.5 nm (in 50 nm scale bar). An increase in capping agent showed big mix shaped particles (which were also agglomerated).

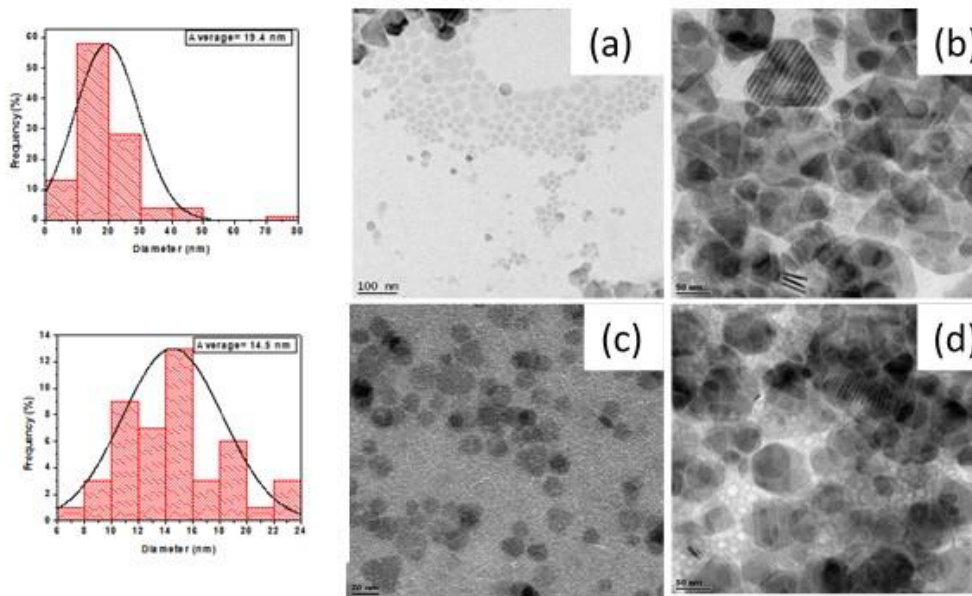


Figure 4.13: TEM images and histograms of CuS nanoparticles prepared in (a) 3 g HDA, (b) 6 g HDA, (c) 3 g TOPO and (d) 6 g TOPO.

4.2.1.1.3 Cu_{2-x}S nanoparticles from Complex 6

4.2.1.1.3.1 (I) UV-vis spectral analyses of HDA-capped nanoparticles

Electron deficient stoichiometric copper sulfide nanoparticles made with HDA and TOPO are presented in Fig. 4.13. The spectra in Fig. 4.13[A] (i) showed that with an increase in capping concentration there was a disappearance of the LSPR peak, this could be due to charge transfer as previously reported by (Kim et al., 2013). This might be possibly caused by charge transfer when the capping agent concentration was increased. It was difficult to determine the short wavelength surface plasmon resonance (SWSPR) appearing in the visible region/wavelength had shifted or stationary with an increase in capping molecule. The sample prepared in 3 g HDA had a blue shifted SWSPR since its absorption maximum ranged from 400-450 nm. This indicates quantum confinement effect in the synthesized sample. The Tauc plot confirmed the blue-shift in the prepared samples, with an increase in particle size with an increase in capping concentration. The lower concentration of HDA gave a spectrum that had a band edge energy of 2.02 eV corresponding to 613 nm, while an increase in capping gave the band edge energy of 1.88 eV that corresponds to 660 nm.

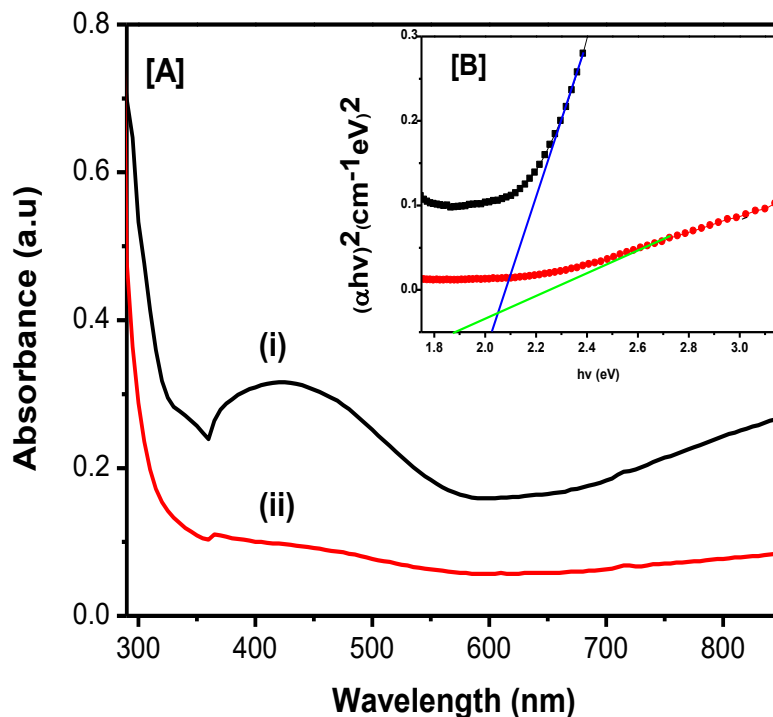


Figure 4.14: Absorption spectra of Cu_{2-x}S nanoparticles in [A] (i) 3 g-HDA and (ii) 6 g-HDA, [B] (inset Tauc plot)

4.2.1.1.3.1 (II) Emission spectral analyses of HDA-capped nanoparticles

The emission spectra of the capped copper sulfide nanoparticles are shown in Fig. 4.14. There were two almost identical peaks for the synthesized particles in both broadness and intensity. The emission maxima of the sample prepared in 3 g HDA was found to be 399 nm and the one synthesized with 6 g HDA had emission maxima of 408 nm slightly redshifted from the sample prepared with 3 g HDA meaning it might contain slightly larger size and morphology distribution than its 3 g counterpart. Their broad spectra also further reveal the larger size distribution or

polydispersity of the synthesized materials but this will be confirmed by TEM images. The trend was in agreement with the absorption spectra.

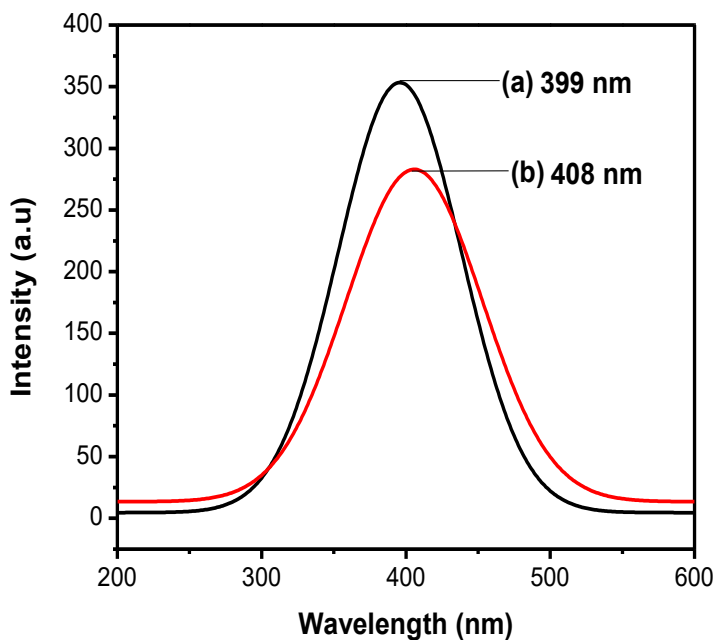


Figure 4.15: Emission spectra of Cu_{2-x}S nanoparticles in (a) 3 g-HDA and (b) 6 g-HDA

4.2.1.1.3.1 (III) UV-Vis spectral analyses of TOPO-capped nanoparticles

The absorption spectra of TOPO-capped copper sulfide nanoparticles is shown in Fig. 4.15. From the excitonic peaks it can be clearly seen that the SWLSPR from the higher concentration of TOPO shifted towards lower wavelengths, indicating a decrease in particle size with an increase in capping agent concentration. The band edges were confirmed in Fig. 4.15[B] by means of extrapolation. Fig. 4.15[A] (i) had a band edge value of 1.94 eV (639 nm) while an increase in concentration gave a band edge value of 2.44 eV (508 nm). The plasmonic behavior was clearly

seen from both samples, thus indicating electron deficient stoichiometry further confirmed by the XRD analysis.

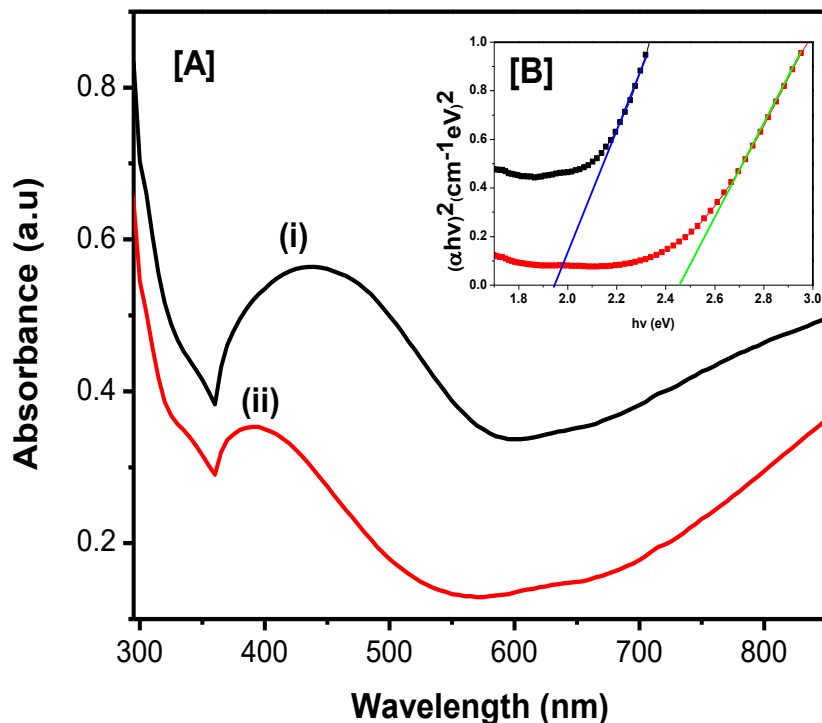


Figure 4.16: Absorption spectra of Cu_{2-x}S nanoparticles in [A] (i) 3g-TOPO and (ii) 6g-TOPO, [B] (inset Tauc plot)

4.2.1.1.3.1 (IV) Emission spectral analyses of TOPO-capped nanoparticles

Fig. 4.16 showed copper sulfide nanoparticles synthesized in TOPO. The sample in Fig. 4.16(a) showed a narrow emission peak indicating a narrow particle distribution, with emission maxima of 380 nm. While sample prepared in Fig. 4.16(b) showed a broad peak indicating larger particle distribution, with emission maxima of 405 nm. The nanoparticles in Fig. 4.16(b) were slightly red-shifted from the nanoparticles in Fig. 4.16(a) indicating bigger nanoparticle formation in the later. The TOPO capped nanoparticles had a lower wavelength emission as compared to the HDA

capped nanoparticles which might mean that samples prepared in TOPO were better passivated than the samples prepared in HDA.

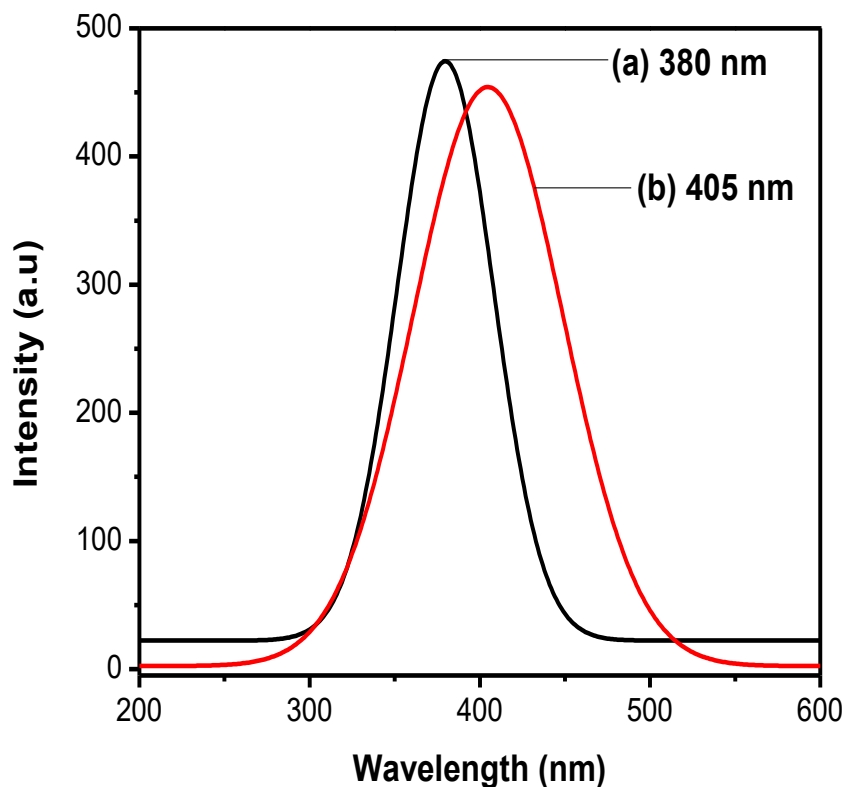


Figure 4.17: Emission spectra of Cu_{2-x}S in (a) 3g-TOPO and (b) 6g-TOPO

4.2.1.1.3.2 Powder X-ray diffraction analysis

X-ray diffraction (XRD) patterns for the nanocrystals prepared using bis(N-pyrrolidinedithiocarbamato)Cu(II) as the precursor are shown in Fig. 4.17. The diffraction pattern showed six peaks for the HDA-capped nanoparticles while the TOPO-capped nanoparticles showed seven peaks. Both spectra were indexed to pure hexagonal phase copper sulfide (CuS) with the JCPDS No. of 03-065-3556. The HDA-capped spectra were similar in crystallinity and

the broadness of the peaks were almost identical. The TOPO-capped nanoparticles showed the same trend as the HDA-capped nanoparticles. However a (006) crystal plane was more pronounced on the TOPO capped nanoparticles compared to the HDA capped nanoparticles. The sharpness of the peaks reveals the crystallinity of the prepared samples. The broadness in those sharp peaks indicates the formation of particles in the nano size regime. The TEM will further confirm the formation of nanoparticles.

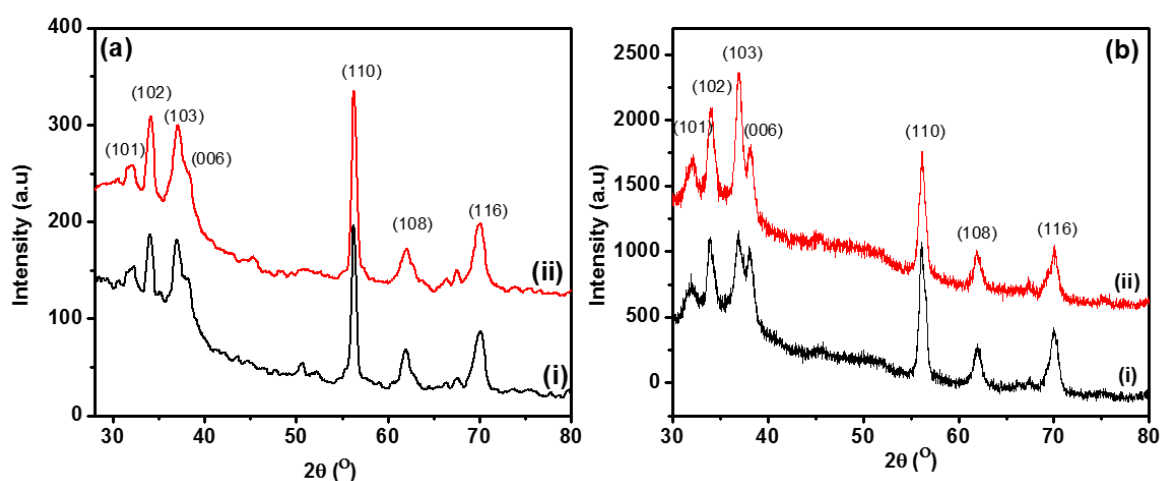


Figure 4.18: XRD patterns of CuS nanoparticles synthesized in (a) (i) 3g, (ii) 6g HDA and (b) (i) 3g, (ii) 6g TOPO.

4.2.1.1.3.3 Transmission electron microscopy (TEM images)

Anisotropic and isotropic copper sulfide nanoparticles were obtained (Fig. 4.18). The particles in Fig. 4.18 (a) and (b) for samples prepared in HDA both showed anisotropic particles. Figure 4.18(a) gave mostly big hexagonal shaped particles and some distorted hexagonal-like shaped particles growing on top of each other, a sign of agglomeration of the as-prepared particles. Figure 4.18(b) showed that an increase in HDA changed the morphology, from hexagonal shape to mixed

morphologies that include sphere-like and rod-like shape. Other than that, there was an agglomeration of particles. The anisotropic shape could be due to the oriented attachment of capping ligand on the surface of the nanoparticles that was also reported by (Lee et al., 2005). The observed trend in concentration was that Fig 4.18(a) gave only hexagonal shape while Fig 4.18(b) gave mixed morphologies with elongated particles present. These results are in agreement with the photoluminescence (PL) which gave broad emission spectra for the samples prepared in HDA than the ones prepared in TOPO. Unlike the HDA-capped nanoparticles, Fig. 4.18(c) for the TOPO-capped nanoparticles in lower concentrations gave well-dispersed nanoparticles with an average diameter of 11.1 nm. The good passivation of the particles by TOPO may be due to steric hindrance that TOPO possesses on the surface of the nanoparticles, confining particles into isotropic sphere-like morphology, of which is characteristic of TOPO-capped nanoparticles. As seen in the histogram that the dominating size were particles in the range of 10-12 nm. The dispersity of particles was in agreement with the PL spectra. While the particles prepared in a higher concentration of TOPO gave anisotropic CuS nanoparticles, their particle shapes included hexagonal, truncated rod-like shape and circular shaped like particles. As predicted from the emission spectra that as the capping concentration increased the particles distribution increased. The mixed morphology may be due to orientation attachment as we increase the capping concentration. The TOPO-capped particles were better passivated as they showed a lower degree of aggregation than their HDA counterparts.

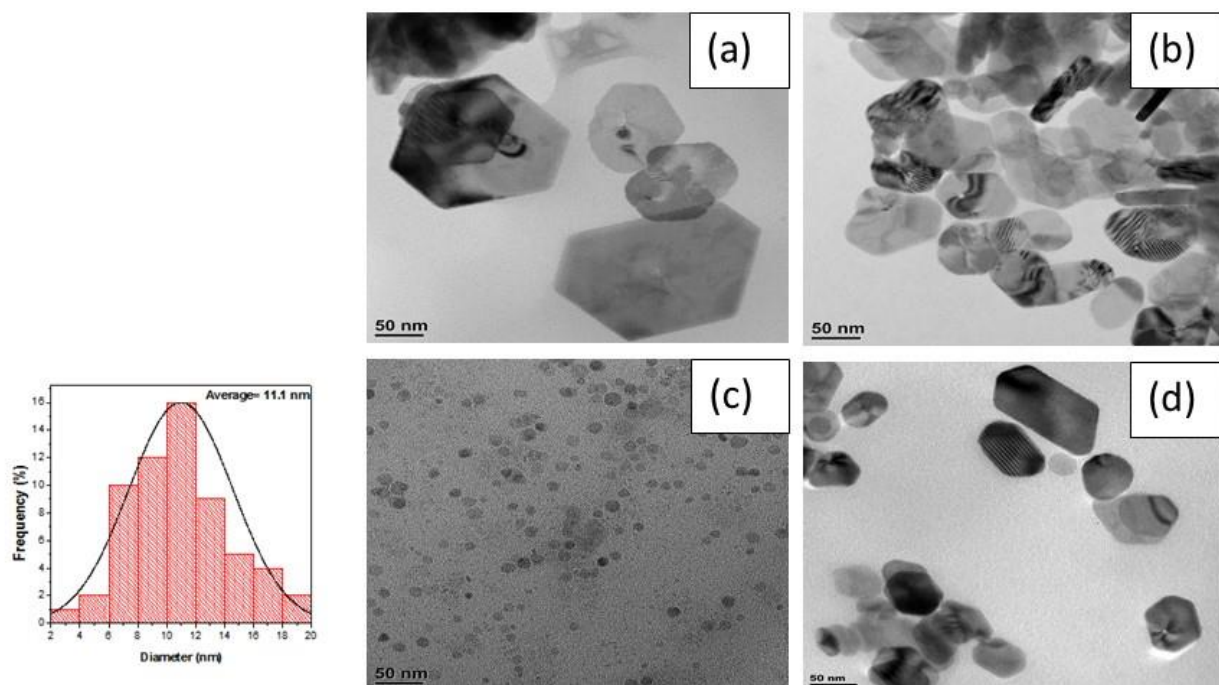


Figure 4.19: TEM images and histograms of CuS nanoparticles prepared in (a) 3g HDA, (b) 6g HDA, (c) 3g TOPO and (d) 6g TOPO.

Table 6 summarizes the obtained results from different complexes. Nanoparticles prepared from cyclohexylamine DTC Cu complex were well passivated in comparison to other ligands. This is apparent from the obtained TEM images that were small in size and well dispersed. Albeit the sizes of TEM and XRD were in contrast for this complex, the trend was also different. Nanoparticles prepared from pyrrolidine DTC Cu complexes gave the most mixed morphological nanoparticles than other complexes suggesting polydispersity. The polydispersity is in agreement with the PL (FWHM) and XRD crystal sizes which gave bigger particle sizes. The sample prepared in 3g TOPO (complex 6) was the only sample that was well passivated in this complex, as seen from its TEM image and the narrow FWHM.

Table 6: Summarized CuS nanoparticles results from the copper complexes

Compound name CuS from (complex)	Band edge (λ) (nm)	Emission (nm)	FWHM	XRD size (nm)	TEM size Or Morphology (nm)
3 g HDA (2)	534	400	103.8	23.2	Agglomerated
6 g HDA (2)	541	378	83	25.8	14.1
3 g TOPO (2)	521	411	103.8	20.3	12.1
6 g TOPO (2)	502	413	97.6	16.4	13.2
3 g HDA (4)	566	413	100.8	17.2	19.5
6 g HDA (4)	539	396	105.6	15.4	Mixed shapes
3 g TOPO (4)	633	398	96.2	18.4	14.5
6 g TOPO (4)	523	401	100.8	19.1	Mixed shapes
3 g HDA (6)	613	399	101.6	35.8	Mixed shapes
6 g HDA (6)	660	408	114	34.4	Mixed shapes
3 g TOPO (6)	639	380	71.2	25.6	11.1
6 g TOPO (6)	508	405	102	25.1	Mixed shapes

4.2.2 Zinc sulfide nanoparticles

4.2.2.1 Optical properties

ZnS is an important II-VI semiconductor with a large bandgap of 3.60 eV, and it is comparable to the most popular ZnO in terms of its versatility in the application in different fields (Fang et al., 2011). But because it has a wider bandgap than ZnO (3.4 eV) it has certain unique properties. It is more suitable for visible-blind ultraviolet (UV)-light based devices such as sensors/photodetectors

(Fang et al., 2011). Traditionally ZnS has two allotropes: one with a cubic phase, (zinc blend sphalerite structure) and another one with a hexagonal phase (wurtzite structure). The cubic phase form is stable at low temperatures, while it transforms to hexagonal phase wurtzite at high-temperature at around 1296 K (Yeh et al., 1992). The latter is more desirable than the cubic phase due to its optical properties. The limiting factor in the hexagonal phase wurtzite is the synthesis temperature required, which is extremely high.

The study of II-VI semiconductor has been extensive in the past few decades due to their quantum confinement effect. The properties of the particles are highly dependent on the size and shape of the particles. The size is mainly associated with the optical, electronic and catalytic properties since the decrease in particle size results in quantized discrete energy bands (Weller, 1993), (Pathak et al., 2012). The reduced particle size can be achieved by coating of the growing crystal with a capping molecule that will also reduce aggregation of the particles by means of Van der Waals interaction. The capping molecule can alter the optical properties in different ways, in that it can be very useful in enhancing the optical properties, but the strong adsorption of the capping molecule on the surface of the nanoparticles can also be very undesirable since the capping molecule can lead to surface irregularities causing trap states. The trap states are the intermediate states inside the band gap. They affect the relaxation radiation, and facilitate the non-radiative relaxation that is undesirable because they emit phonons rather than the photons emitted in the radiative relaxation.

4.2.2.1.1 ZnS nanoparticles from Complex 1

4.2.2.1.1.1 (I) UV-vis spectral analyses of HDA-capped nanoparticles

UV–Vis absorption spectra of the synthesized ZnS nanoparticles are shown in Fig 8 (a) and (b) for 3 g and 6 g HDA respectively. By applying the Tauc plot to the absorption spectra, the absorption edges were found to be 358 nm and 400 nm for Fig. 4.19[A] (i) and (ii) respectively. The absorption for both samples are red shifted from the bulk ZnS (345 nm). This red shift could be due to the reasons mentioned above i.e. they can be attributed to intraband surface trap states formed by surfactant molecules of HDA chemically bound on the ZnS surface which can alter the optical properties of the synthesized particles. As observed from the spectrum (Fig. 4.19[B]) it would be expected that particles synthesized with 3 g HDA (Fig. 4.19[A] (i)) to be smaller compared to the particles synthesized with 6 g HDA (Fig. 4.19[A] (ii)) due to the difference in the absorption edges of both samples. This means that the particle size increases with the increase in capping concentration.

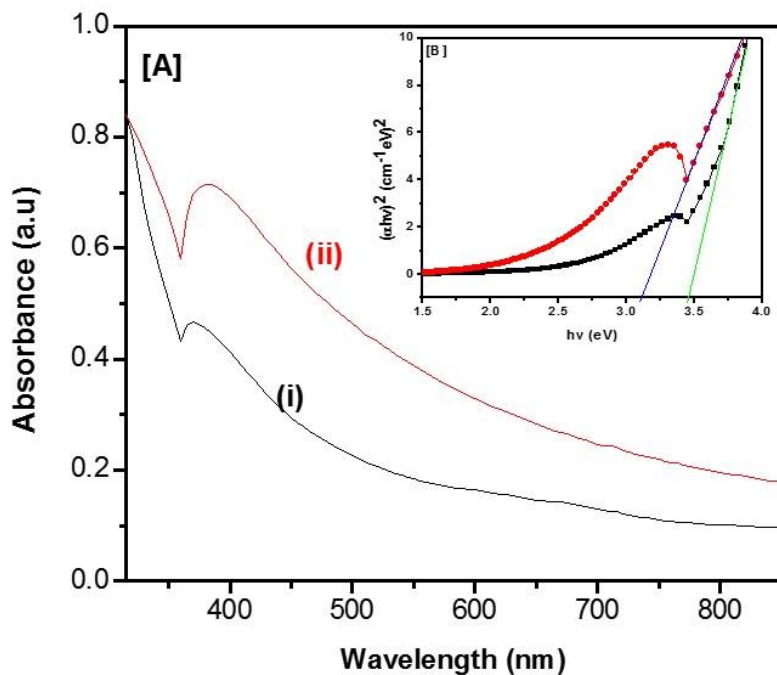


Figure 4.20: Absorption spectra of ZnS nanoparticles in [A] (i) 3 g-HDA and (ii) 6 g-HDA, [B] (inset Tauc plot)

4.2.2.1.1.1 (II) Emission spectral analyses of HDA-capped nanoparticles

The emission spectra of the as-prepared nanoparticles dispersed in toluene are shown in Fig 4.20. The spectra of both samples are red shifted in relation to their absorption spectra, but the sample in Fig. 4.20(a) shows a red shift increase in, with an emission maximum of 406 nm while the sample shown in Fig. 4.20(b) has an emission maximum of 386 nm. This indicates that the particle size increases with an increase in capping molecule concentration as seen from the absorption spectra. In terms of the broadness of the peak, the calculated full width at half maximum (FWHM) for the sample in Fig. 4.20(a) had a value of 97.8 nm, while for Fig. 4.20(b) the value was 108 nm. This suggests that the polydispersity was increasing with an increase in capping molecule.

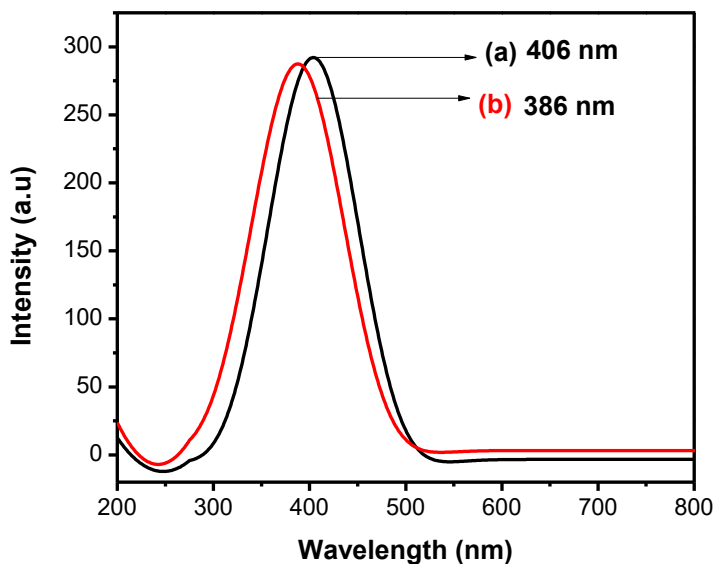


Figure 4.21: Emission spectra of ZnS nanoparticles in (a) 3 g-HDA and (b) 6 g-HDA

4.2.2.1.1.1 (III) UV-Vis spectral analyses of TOPO-capped nanoparticles

The absorption spectra of TOPO-capped ZnS nanoparticles is shown in Fig. 4.21[A] and the Tauc plot that was used to determine the band gap energy. The extrapolated values were red-shifted from the bulk ZnS (345 nm) with the values found to be 3.4 (365 nm) and 3.54 eV (350 nm) for Fig. 4.21[A] (i) and (ii) respectively. The increase in capping concentration suggested a decrease in particle size. In comparison to the HDA-capped nanoparticles, the trend was the total opposite, in HDA-capped particles the trend was an increase in particles size with an increase in capping concentration, while the TOPO-capped was vice versa. This is possibly due to different binding properties (different functional groups) of the capping molecule with the surface of the nanoparticles.

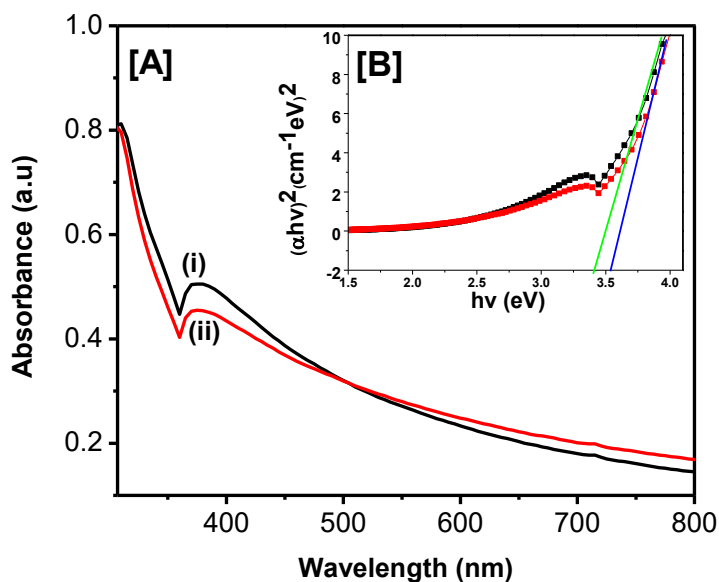


Figure 4.22: Absorption spectra of ZnS nanoparticles in [A] (i) 3 g-TOPO and (ii) 6 g-TOPO, [B] (inset Tauc plot)

4.2.2.1.1.1 (IV) Emission spectral analyses of TOPO-capped nanoparticles

The emission spectra of ZnS TOPO-capped nanoparticles is presented in Fig. 4.22(a) and (b) for nanoparticles capped with 3 g and 6 g TOPO respectively. Just like the HDA-capped nanoparticles they were red shifted from their absorption spectra with a near band edge emission. The obtained emission maxima were 411 nm for both Fig. 4.22(a) and (b). On the other hand the broadness of the prepared samples was identical with an FWHM value of 87.2 nm. The FWHM of the TOPO capped nanoparticles was narrow compared to that of the HDA-capped nanoparticles thus indicating small particle distribution in the TOPO-capped nanoparticles.

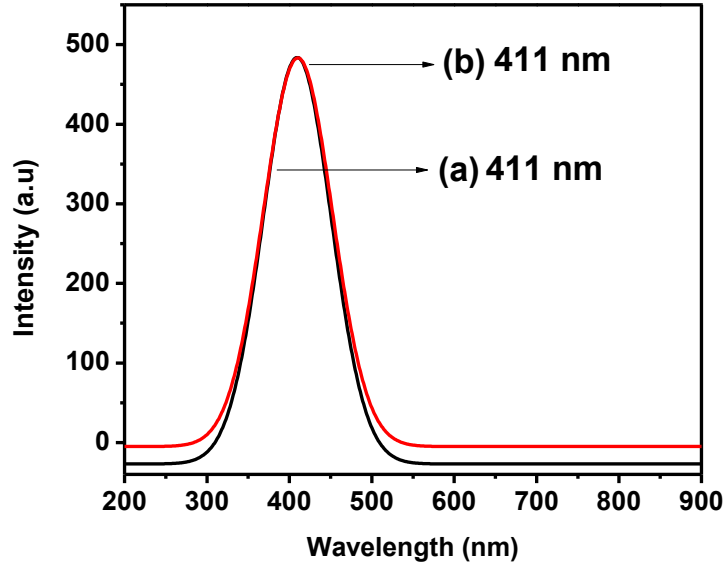


Figure 4.23: Emission spectra of ZnS nanoparticles in (a) 3 g-TOPO and (b) 6 g-TOPO

4.2.2.2 Powder X-ray diffraction analysis

The XRD patterns were used to determine the phases that were formed. In terms of phases the HDA-capped nanoparticles an interesting finding (hexagonal phase) in most of the samples. It is interesting because the synthetic conditions are unfavorable for this phase. It is reported only at high temperatures by annealing at elevated temperatures (Sekhar Tiwary et al., 2011), (Kole & Kumbhakar, 2012) and (Shanmugam et al., 2013), while few reports have managed to synthesize ZnS wurtzite structure (hexagonal phase) at low temperature (Zhao et al., 2004) and (Patel et al., 2013). The HDA samples gave sulfur impurities (which appeared in the 2θ range of $20-30^\circ$ mostly, peaks appearing above 30° were correlating with the phase formed) in most of the samples. The TOPO capped nanoparticles on the other hand showed less

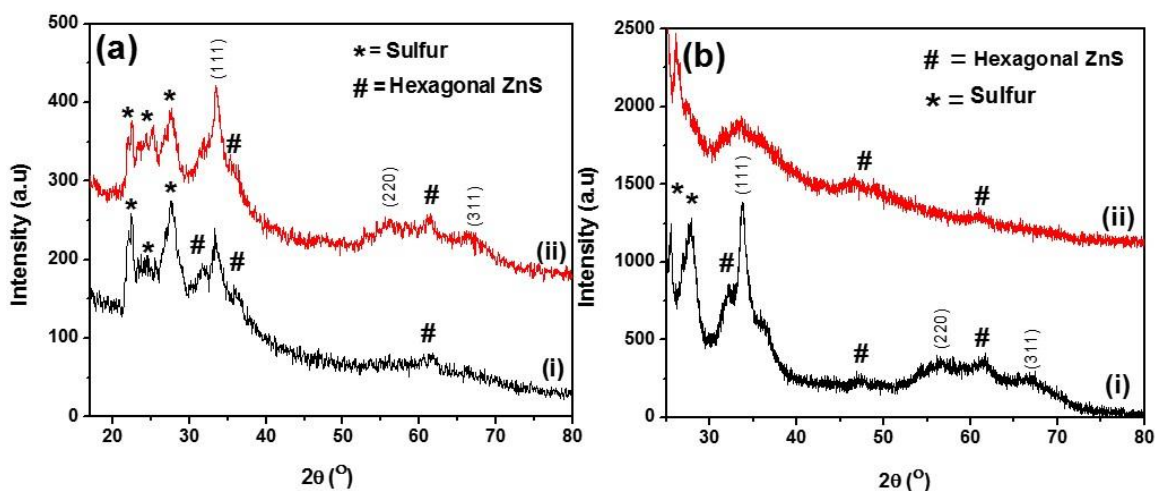


Figure 4.24: XRD patterns of ZnS nanoparticles synthesized in (a) (i) 3 g, (ii) 6 g HDA and (b) (i) 3 g, (ii) 6 g TOPO.

The crystal structure of ZnS nanoparticles prepared from bis(cyclohexylamine-N-dithiocarbamate)Zn(II) complex is shown in Fig. 4.24. The HDA capped nanoparticles gave a spectrum with mixed phases. There were sulfur peaks in the 2θ range of $20-30^\circ$ with a JCPDS card no. 01-089-6967. The peaks that occurred above 30° were carefully assigned to the hexagonal phase and cubic phase ZnS, with JCPDS card no. 01-072-9271 and 01-072-4841 for hexagonal and cubic phase respectively. Crystal planes that are indexed (111, 220, and 311) represent the cubic phase ZnS. The increase in capping agent concentration improved crystallinity, since the (220) and (311) planes were pronounced compared to the sample prepared in 3 g HDA. The TOPO capped nanoparticles showed an opposite of the results obtained from HDA, since in the later lower concentration of TOPO gave better crystalline peaks (220 and 311) than the former. The phases were mixed as well similar to the HDA capped nanoparticles. The broadness of the peaks in higher concentration of TOPO suggested a decrease in particle size with increase capping molecule concentration. Interestingly, the formation of hexagonal phase ZnS at lower temperature. It is mostly reported at temperatures higher than 1000°C (Kole & Kumbhakar, 2012).

4.2.2.3 Transmission electron microscopy (TEM images)

The TEM images in Fig. 4.24 represent the HDA and TOPO capped ZnS nanoparticles. Fig. 4.24(a) and (d) gave very small particles that had combined together forming sphere-like particles in the case of Fig. 4.24(d), while in Fig. 4.24(a) they were elongating by aligning close to each other, therefore it was extremely difficult to pinpoint and calculate each particle since their inter-particle distance were small. The particles in Fig. 4.24(d) were of different sizes ranging from 5-50 nm but mostly dominated by in the range of 20-30 nm in size. The sizes obtained were not the clear representative of the image since other sizes were very small that it was very hard to measure them. Then Fig. 4.24(b) and (c) gave the well-dispersed particles with the clear spherical shape, they were almost monodispersed thus confirming the narrower dispersity in the PL spectra. The average particle sizes were found to be 4.8 and 6.7 nm for Fig. 4.24(a) and (c) respectively. The small sizes were in good agreement with the broad diffraction peaks on the crystal structure analyses that indicates small particle sizes.

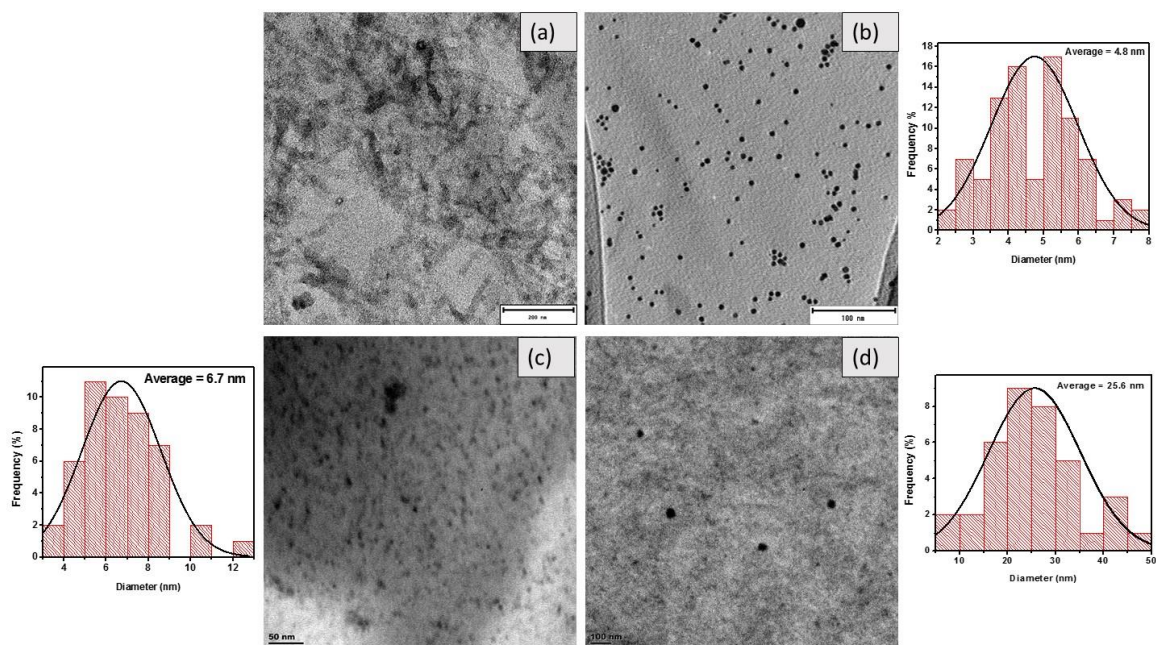


Figure 4.25: TEM images and histograms of ZnS nanoparticles prepared in (a) 3 g HDA, (b) 6 g HDA, (c) 3 g TOPO and (d) 6 g TOPO

4.2.2.1.2 ZnS nanoparticles from Complex 3

4.2.2.1.2.1 (I) UV-Vis spectral analyses of HDA-capped nanoparticles

The absorption spectra are shown in Fig. 4.25 reveals the optical absorption properties of ZnS nanoparticles synthesized from bis(N-phenyldithiocarbamato)Zn(II). The *inset* Tauc plot clearly shows the extrapolated band edges of the prepared samples. The calculated band edges were both blue-shifted from the bulk ZnS nanoparticles unlike the nanoparticles prepared from bis(cyclohexylamine-N-dithiocarbamato)Zn(II) complex which showed the surface defect absorption spectra that were red-shifted from the bulk. The blue shift in absorption spectra thus indicated the quantum confinement effect in the prepared nanoparticles. The extrapolated band edges were found to be 3.90 and 3.95 eV corresponding to 317 and 313 nm for Fig. 4.25[A] (i)

and (ii) respectively. The increase in capping agent concentration suggested a decrease in particle sizes.

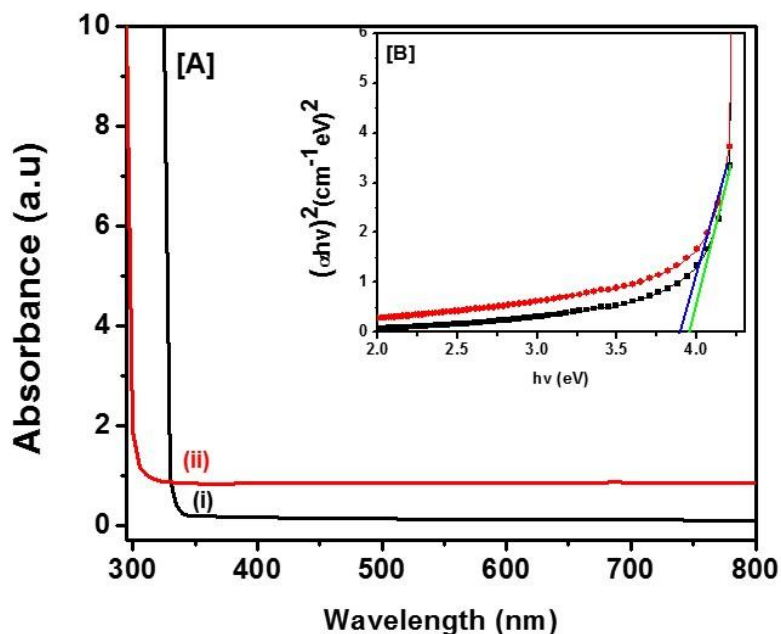


Figure 4.26: Absorption spectra of ZnS nanoparticles in [A] (i) 3 g-HDA and (ii) 6 g-HDA, [B] (inset Tauc plot)

4.2.2.1.1.1 (II) Emission spectral analyses of HDA-capped nanoparticles

To understand the emission optical properties of the ZnS nanoparticles prepared from bis(N-phenyldithiocarbamato)Zn(II) complex, the photoluminescence spectra was studied . The emission spectra showed a near band edge emission for both samples, with the emission maxima of 335 and 338 nm for the as-synthesized samples in Fig. 4.26(a) and (b) respectively. The emission maxima were both red shifted from their absorption spectra. The FWHM values were found to be 42.6 and 41 nm (which was a very small change) for Fig. 4.26(a) and (b) respectively. Their trend was a

decrease in FWHM with an increase in capping molecule concentration suggesting a decrease in particle distribution with an increase in capping molecule concentration.

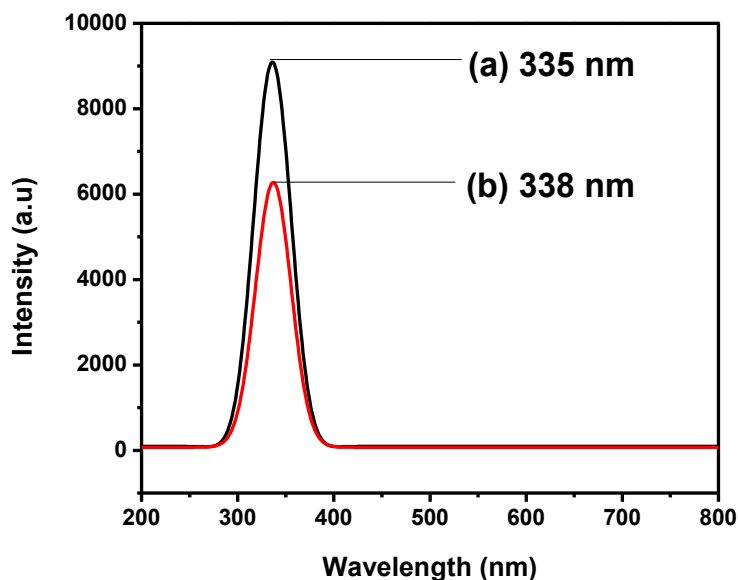


Figure 4.27: Emission spectra of ZnS nanoparticles in (a) 3 g-HDA and (b) 6 g-HDA

4.2.2.1.1.2 Powder X-ray diffraction analysis

The crystal structure of the as-synthesized nanoparticles was determined by X-ray diffraction. Fig. 4.27 shows the XRD pattern of the as-prepared TOPO-capped ZnS nanoparticles. In Fig. 4.27(a) the prepared nanoparticles showed hexagonal phased ZnS nanoparticles with a JCPDS card no. 01-072-9271 which was also observed in the previous HDA-capped ZnS nanoparticles, thus showing that HDA can be very useful in synthesizing hexagonal phase ZnS nanoparticles even at lower temperatures such as the one used in this study. The HDA was good in the formation of the hexagonal phase but it also showed some negatives, which were the consistent formation of sulfur impurity peaks (from excess DTC compound)). The ideal capping molecule should produce high

quality and defect free nanoparticles which were not the case for the as prepared HDA-capped nanoparticles. The sulfur impurities could be due to the unreacted or excess sulfur molecules during the synthesis of the nanoparticles. In terms of the broadness of the peaks they were less broad compared to the nanoparticles prepared in Fig. 4.27(b). The less broad peaks indicate the formation of bigger sized nanoparticles compared to the ones prepared in Fig. 4.27(b). The obtained crystal sizes were 3.2 and 5.5 nm for particles prepared in Fig. 4.27(a) (i) and (ii) respectively.

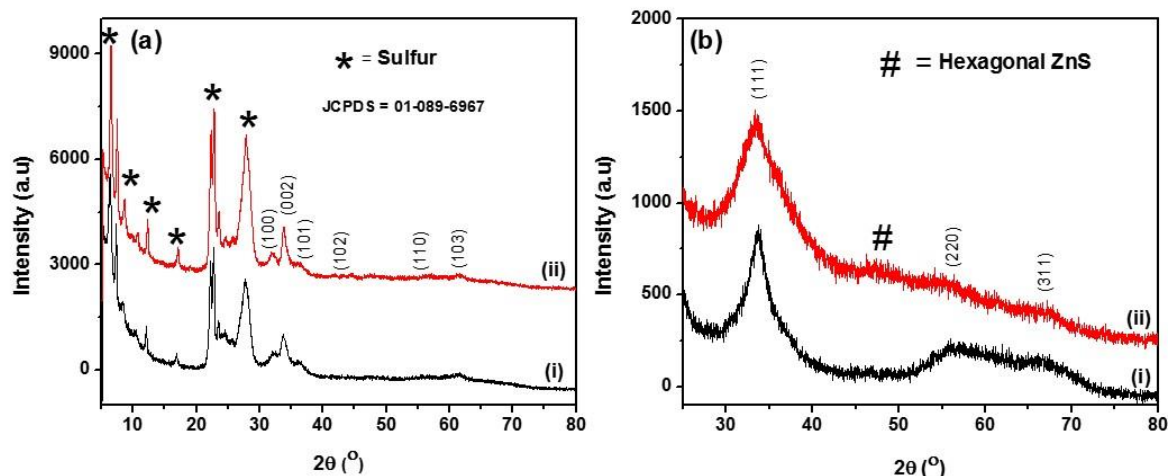


Figure 4.28: XRD patterns of ZnS nanoparticles synthesized in (a) (i) 3 g HDA, (ii) 6 g HDA and (b) (i) 3 g TOPO, (ii) 6g TOPO

The TOPO-capped nanoparticles on the other hand gave a ZnS cubic phase with a JCPDS card no. 01-072-4841. The increase in capping concentration in Fig. 4.26(b) (ii) showed an emergence of a (102) crystal plane of the hexagonal phase ZnS and there was an apparent decrease in other diffraction peaks which could be due to the excess capping molecule in the increased concentration. The broadness of the (111) crystal plane which was used to calculate the crystal size was increasing with an increase in capping agent concentration, thus indicating the formation

of smaller sized nanoparticles at a higher concentration of TOPO. The calculated crystal sizes were 1.9 and 1.0 nm for Fig. 4.27(b) (i) and (ii) respectively of which were smaller compared to the nanoparticles in Fig. 4.27(a).

4.2.2.1.1.3 Transmission electron microscopy (TEM images)

The morphologies and dimensions of the as-synthesized ZnS nanoparticles were studied by TEM measurements. The TEM images of the HDA-capped nanoparticles is shown in Fig. 4.28(a) and (b), while those of TOPO are shown in Fig. 4.28(c) and (d). The HDA-capped nanoparticles were very small spherical dot-like particles aligned in an elongated lattice fringe-like manner. The increase in capping molecule showed more visible fringe-like particles with the presence of agglomeration. On the other hand the nanoparticles passivated by TOPO were spherical monodispersed nanoparticle upon an increase in capping agent concentration, while the lower concentrations also showed narrow particle distribution with small aggregations thus confirming the broad emission peak in Fig. 4.26(a) that suggested large particle distribution compared to the higher concentrations of TOPO in Fig. 4.26(b). The average particle size of the TOPO-capped nanoparticles was found to 8.4 and 4.5 nm for particles prepared in Fig. 4.28(c) and (d) respectively.

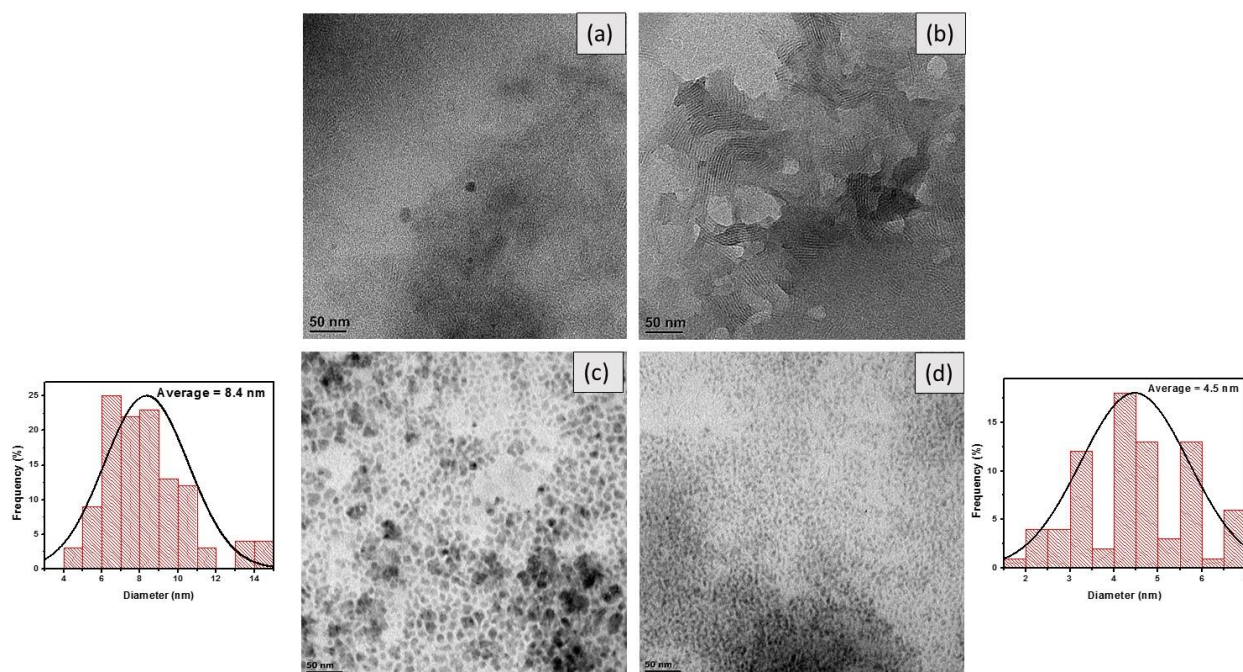


Figure 4.29: TEM images and histograms of ZnS nanoparticles prepared in (a) 3 g HDA, (b) 6g HDA, (c) 3 g TOPO and (d) 6 g TOPO.

4.2.2.1.1 ZnS nanoparticles from Complex 5

4.2.2.1.1.1 (I) UV-Vis spectral analyses of HDA-capped nanoparticles

The absorption spectra of ZnS nanoparticles prepared from bis(N-pyrrolidinedithiocarbamate) Zn(II) complex is presented in Fig. 4.29 [A] and the insert in Fig. 4.29 [B] is the Tauc plot of the corresponding HDA-capped ZnS. The Tauc plot gave the exact band edges of the prepared materials. The capping concentration had an effect on the size or shape of the nanoparticles, this was indicated by the Tauc plot band edges which showed a decrease in wavelength with an increase in capping concentration. The particles prepared in lower concentration were slightly red-shifted from the bulk ZnS (345 nm). The redshift might be due to the surrounding capping molecule on the surface of the nanoparticles, which could cause surface trap states that could alter the optical properties in various ways. The surface states could be the result of impurities from the capping

molecule but this could be seen from the XRD analysis. The band edge values were 3.58 and 3.73 eV that corresponds to 346 and 332 nm for the samples prepared in Fig. 4.29 [A] (i) and (ii) respectively.

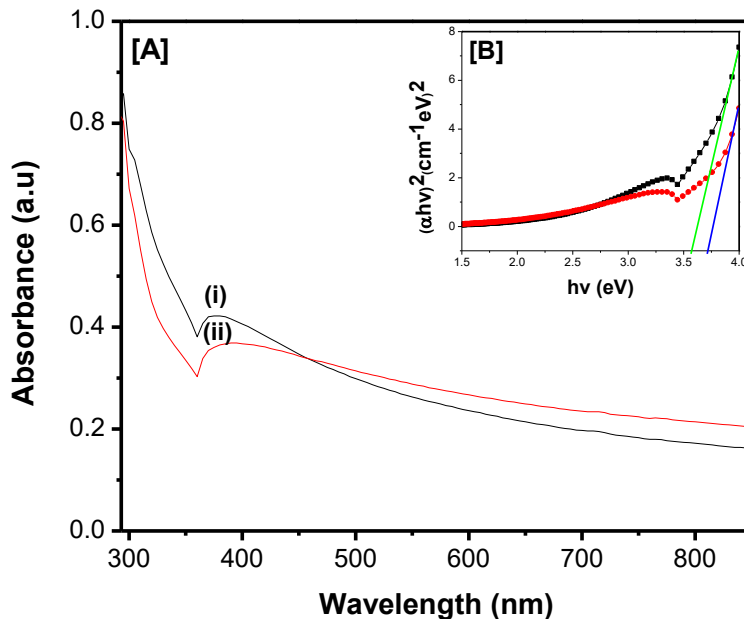


Figure 4.30: Absorption spectra of ZnS nanoparticles in [A] (i) 3g-HDA and (ii) 6g-HDA, [B] (inset Tauc plot)

4.2.2.1.1.1 (II) Emission spectral analyses of HDA-capped nanoparticles

The photoluminescence spectrum of HDA-capped and TOPO-capped ZnS nanoparticles reveal the optical luminescence of the synthesized ZnS nanocrystals. Fig. 4.30(a) showed a broad peak with a FWHM value of 128.8 nm for the sample prepared in 3 g HDA thus indicating polydispersity of the synthesized material compared to the sample prepared in Fig. 4.30(b). The narrow peak in Fig. 4.30(b) that has the FWHM value of 93.4 nm which indicates smaller particle distribution. The

increase in capping concentration resulted with a decrease in FWHM, suggesting that the capping agent has an effect on the shape or size of the prepared nanoparticles. The emission maxima obtained was 407 nm and 405 nm for the sample prepared in 3 g and 6 g HDA respectively, both samples were red shifted from their absorption spectra with a close to band edge emission. The emission wavelength and intensity decreased with an increase in capping molecule concentration indicating a strong adsorption of the capping molecule on the surface of the nanoparticles causing trap emissions.

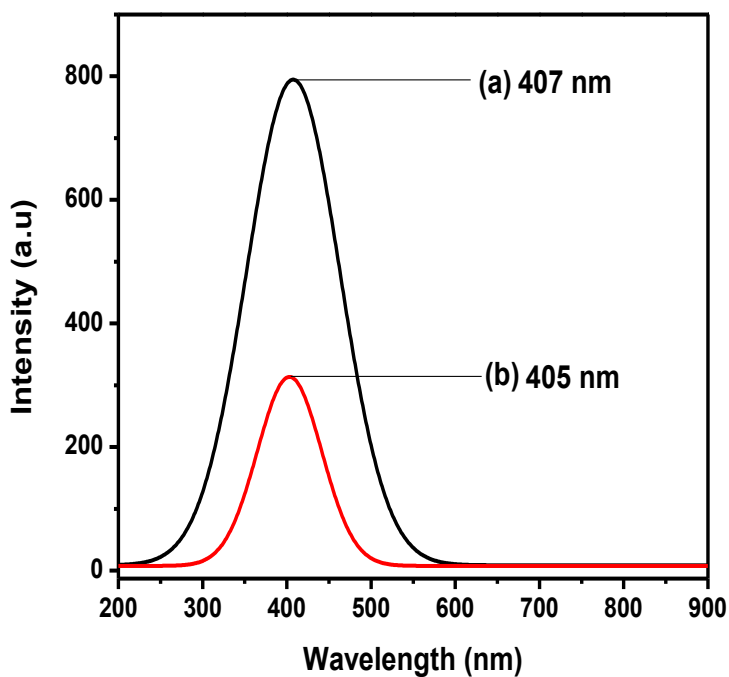


Figure 4.31: Emission spectra of ZnS nanoparticles in (a) 3g-HDA and (b) 6g-HDA

4.2.2.1.1.1 (III) UV-Vis spectral analyses of TOPO-capped nanoparticles

The absorption spectra of the prepared samples indicated the formation of the prepared samples in the nano-size or micro-size regime. Unlike the HDA-capped samples which showed blue and red-shifted particles, the TOPO-capped particles were both red-shifted from the bulk ZnS (345 nm). The red-shifted absorption as previously stated for the HDA-capped nanoparticles that it could be due to the impurities from the capping ligands on the surface of the nanoparticles causing surface irregularities that further results with the trap states that are intermediate of the valence and conduction band. The degree of red shift was very significant for the samples prepared in TOPO than the ones prepared in HDA. The obtained band edges were 3.54 and 3.34 eV that corresponds to 350 and 371 nm for samples shown in Fig. 4.31 [A](i) and (ii) respectively. Their trend was the opposite of the samples prepared in HDA, since they were increasing with an increase in capping concentration.

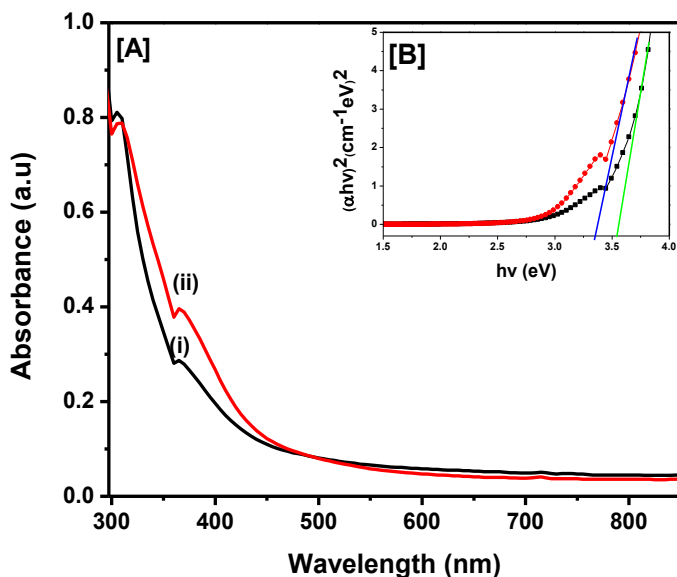


Figure 4.32: Absorption spectra of ZnS nanoparticles in [A] (i) 3g-TOPO and (ii) 6g-TOPO, [B] (inset Tauc plot)

4.2.2.1.1.1 (IV) Emission spectral analyses of TOPO-capped nanoparticles

The TOPO-capped ZnS nanoparticles are presented in Fig. 4.32(a) and (b). In comparison to the HDA-capped nanoparticles the emission spectra were total opposite to each other in terms of intensity. They were very much similar in another aspect despite their wavelength differences. They were similar in the trend, since the TOPO-capped particles also gave a narrow peak for a higher concentration of capping molecule and broad peak for the lower concentration of TOPO. The FWHM of the TOPO capped nanoparticle was very high for the sample in Fig 4.32(a) the obtained value was 176.4 nm, while the increase in capping agent gave the FWHM value of 112 nm. As observed previously the wavelength was decreasing with an increase in capping concentration suggesting a decrease in particle size with an increase in capping concentration. The decrease in particle size with an increase in capping concentration could be due to the formation of ZnS nuclei in higher concentration than in lower concentrations.

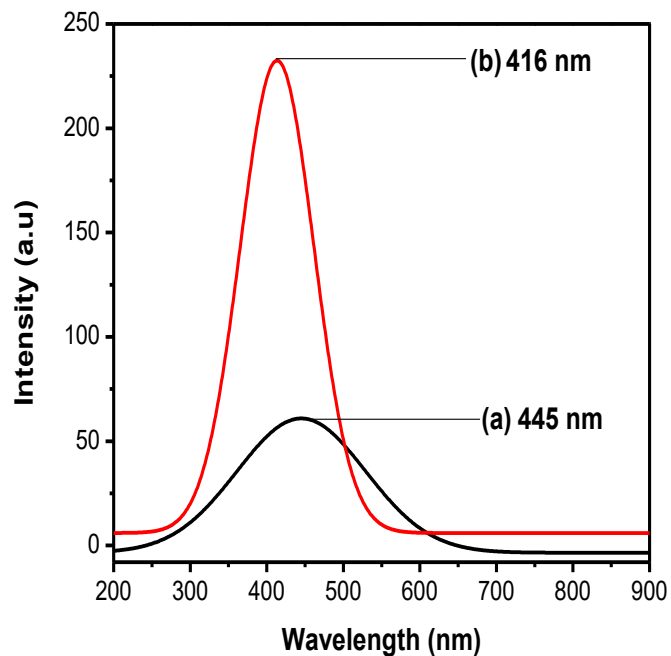


Figure 4.33: Emission spectra of ZnS nanoparticles in (a) 3g-TOPO and (b) 6g-TOPO

4.2.2.1.1.2 Powder X-ray diffraction

The crystal structure of HDA and TOPO capped zinc sulfide nanoparticles was studied in Fig. 4.33. The Fig. 4.33(a) presents the HDA capped nanoparticles, while Fig. 4.33(b) shows that are capped in TOPO. The HDA-capped nanoparticles showed some presence of impurities that were corresponded to the triclinic sulfur with the JCPDS card no. of 01-089-6764. The presence of impurities were predicted from the absorption spectra that gave red-shifted absorption for the lower concentration of HDA. Other than the impurities, the sample gave hexagonal phase that was also obtained in the previous sections for the preparation of HDA-capped ZnS nanoparticles.

(Patel et al., 2013) and (Zhao et al., 2004) reported the formation of hexagonal phase ZnS at 150 °C without the use of a capping molecule. Thus far the structural kinetics and chemistry of the formation of the high-temperature stable phase at lower temperatures are still unknown. The

diffraction peaks at $\sim 33.2^\circ$, 47.5° and 62.3° corresponding to (100)(002)(101), (110) and (103) crystal planes were carefully indexed. The diffraction peaks were indexed with the JCPDS card no. 01-072-9271. The diffraction peaks match very well with slight shifts in the positions of the various crystal planes of hexagonal phase of ZnS crystals but their intensity were very low. On the other hand for the TOPO-capped nanoparticles, the pure cubic phase ZnS was obtained in both concentrations but they showed poor crystallinity in other crystal planes (220 and 311). The diffraction peaks have been indexed with JCPDS card no. 01-072-4841. The broadness in the spectra for both samples indicates the formation of particles in the nano-sized regime. The particles were in good agreement with the absorption spectra trends of both the capping molecule. The particle sizes were 2.2 and 1.5 nm for Fig. 4.33(a) (i) and (ii) respectively, while particle size for TOPO-capped ZnS nanoparticles was found to be 1.4 and 1.5 nm for Fig. 4.33(b) (i) and (ii) respectively. The calculations were all based on one crystal plane, the (002) plane for HDA capped nanoparticles while (111) plane was used for TOPO capped nanoparticles.

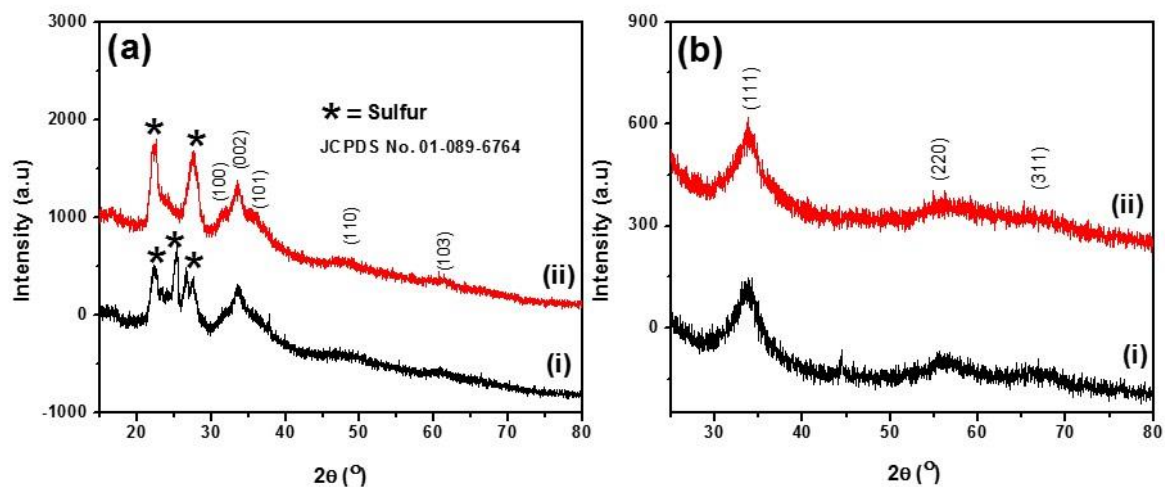


Figure 4.34: XRD patterns of ZnS nanoparticles synthesized in (a) (i) 3g, (ii) 6g HDA and (b) (i) 3g, (ii) 6g TOPO.

4.2.1.1.3.3 Transmission electron microscopy (TEM images)

Figure 4.34 shows the TEM images of HDA and TOPO capped ZnS nanoparticles. In Fig. 4.34(a) there was a support like material and on that surface of that support small sphere-like shaped particles were observed with an average particle size of 6.9 nm as seen from the histogram. The support like material could be due to the capping molecule. Then the increase in concentration in Fig. 4.34(b) showed very small particle size, the formation of very small nanoparticles is typical for ZnS nanoparticles. Then on the TOPO-capped nanoparticles, Fig. 4.34(c) showed agglomerated particles with no clear crystal edges, this was evident from the XRD crystal planes that were amorphous like. In those agglomerated particles there were smaller particles combined together with a very small inter-particle distance that makes it difficult to see the shapes present in the image. The increase in capping concentration in Fig. 4.34(d) was much more visible than the lower concentration this could be due to more binding sites in the higher concentrations. The shape formed in Fig. 4.34(d) was also a spherical shape with an average particle size of 2.5 nm. TEM complements the results obtained from the XRD crystal size.

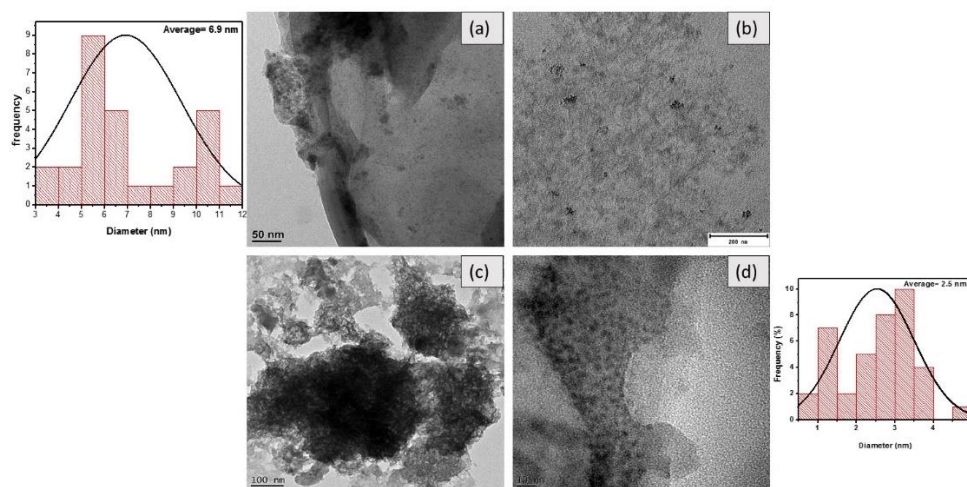


Figure 4.35: TEM images and histograms (a and d) of CuS nanoparticles prepared in (a) 3g HDA, (b) 6g HDA, (c) 3g TOPO and (d) 6g TOPO.

All the results obtained for ZnS nanoparticles are summarized in **Table 7**. From the summarized results it is clear that nanoparticles prepared from TOPO were better passivated than the ones prepared in HDA. It is also clear that the crystal sizes were not comparable with the TEM sizes, since the difference in sizes was very high. This might be due to the fact that one crystal plane was used to calculate the crystal size. The ligand that gave better results in nanoparticles (in terms of particle sizes) was the cyclohexylamine ligand. This ligand also gave better results in CuS nanoparticles, which makes it an ideal ligand for the synthesis of other semiconductor nanoparticles. This could be due to cyclic ring that has strong electron donating abilities compared to the aromatic ring that possess electron withdrawing properties. In terms of the optical properties nanoparticles prepared from aniline ligand were superior compared to the other ligands. Since they gave blue shifted absorption spectra for all samples and the narrow FWHM values compared to other ligands. In the optical properties nanoparticles prepared from cyclohexylamine all showed red-shifted absorption spectra. The red-shift was attributed to trap states caused by impurities, this was further confirmed by XRD spectra that gave extra peaks corresponding to triclinic sulfur. The sulfur peaks were consistent throughout the HDA capped nanoparticles.

Table 7: Summarized results of ZnS nanoparticles prepared from Zn complexes

Compound name ZnS from (complex)	Band edge (λ) (nm)	Emission (nm)	FWHM	XRD size (nm)	TEM size Or Morphology (nm)
3 g HDA (1)	358	406	98	3.2	Agglomerated
6 g HDA (1)	400	386	108	3.8	4.8
3 g TOPO (1)	365	411	87.2	1.0	6.7
6 g TOPO (1)	350	411	87.2	5.2	25.8
3 g HDA (3)	317	335	42.6	31.2	Very small
6 g HDA (3)	313	338	41.0	32.4	Mixed shapes
3 g TOPO (3)	341	356	55.1	1.9	8.4
6 g TOPO (3)	330	358	52.3	1.0	4.5
3 g HDA (5)	346	407	128.8	2.3	6.9
6 g HDA (5)	332	405	93.4	1.5	Agglomerated
3 g TOPO (5)	350	445	176.4	1.4	Agglomerated
6 g TOPO (5)	371	416	112	1.5	2.5

4.3 Conclusion

The synthesis of CuS and ZnS by single source precursor method proved to be an effective method for synthesis of small and narrow size distributed nanoparticles. This was confirmed by XRD and TEM images that gave small sized particles. However, most of the HDA-capped ZnS nanoparticles consistently showed the presence of impurities that were indexed to triclinic sulfur. The presence of the impurities could be attributed to the strong adsorption of the capping molecule to the surface

of the nanoparticles causing surface irregularities that leads to the trap states. The formation of the trap states was also observed on the absorption spectra by giving red shifted absorption in prepared samples, therefore suggesting that there were impurities that altered the absorption spectra since it was not in agreement with the TEM images that gave very small particles. Other than the impurities and trap states there were some interesting features on the prepared ZnS nanoparticles, which was the formation of hexagonal or wurtzite phase of which is the very difficult phase to obtain at lower temperature since it is only stable at higher temperatures above 1000 °C. The formation of hexagonal phase opens up opportunities for lot of applications. On the other hand, the copper sulfide nanoparticles were all blue-shifted from the bulk thus indicating quantum confinement effect on the prepared samples. Like the ZnS nanoparticles that showed interesting features, the copper sulfide also had some interesting properties which were the formation of localized surface plasmon resonances that was due to the electron deficient nature of the prepared copper sulfide nanoparticles. The electron deficient stoichiometry was also confirmed by XRD analysis, which gave copper sulfide covellite. In some there were slight formation of both covellite and chalcocite but their formation caused an unraveling of the surface plasmon resonances, but in some instances the disappearance of the plasmonic peak was caused by strong adhesion of the capping molecule on the surface of the nanoparticles.

4.4 References

AJIBADE, P.A. & OSUNTOKUN, J.. 2014. Synthesis and Characterization of Hexadecylamine Capped ZnS , CdS , and HgS Nanoparticles Using Heteroleptic Single Molecular Precursors. *J. Nanomater.* **2014** pp. 1–7.

- CHEN, L., SAKAMOTO, M., SATO, R. & TERANISHI, T.. 2015. Determination of a localized surface plasmon resonance mode of Cu₇S₄ nanodisks by plasmon coupling. *Faraday Discuss.* **0** pp. 1–10.
- COFFEY, T.A., FORSTER, G.D. & HOGARTH, G.. 1993. Double Sulfur-Carbon Bond Cleavage of a Dithiocarbamate Ligand at a Molybdenum(VI) Centre; Synthesis and X-Ray Structure of the Disulfur Complex [Mo(NPh)(S₂)(edtc)₂] (edtc = S₂CNEt₂). *J. Chem. Soc. Commun.* **511** (3) pp. 1524–1525.
- DORFS, D., HÄRTLING, T., MISZTA, K., BIGALL, N.C., KIM, M.R., GENOVESE, A., FALQUI, A., POVIA, M. & MANNA, L.. 2011. Reversible tunability of the near-infrared valence band plasmon resonance in Cu₂-xSe nanocrystals. *J. Am. Chem. Soc.* **133** (29) pp. 11175–11180.
- FANG, X., ZHAI, T., GAUTAM, U.K., LI, L., WU, L., BANDO, Y. & GOLBERG, D.. 2011. ZnS nanostructures: From synthesis to applications. *Prog. Mater. Sci.* **56** (2) pp. 175–287.
- FAUCHEAUX, J.A., STANTON, A.L.D. & JAIN, P.K.. 2014. Plasmon Resonances of Semiconductor Nanocrystals: Physical Principles and New Opportunities. *J. Phys. Chem. Lett.* **5** (6) pp. 976–985.
- HOGARTH, G.. 2012. Metal-dithiocarbamate complexes: chemistry and biological activity. *Mini Rev. Med. Chem.* **12** (12) pp. 1202–15.
- HSU, S.-W., ON, K. & TAO, A.R.. 2011. Localized surface plasmon resonances of anisotropic semiconductor nanocrystals. *J. Am. Chem. Soc.* **133** (47) pp. 19072–5.
- KENT, J.A. & RIEGEL. 2012. *Hand book of Industrial Chemistry and Biotechnology*. 11th ed. KENT, J. A., ED. Morgantown, West Virginia, USA: © 2007 Springer Science+Business Media,

LLC.

KIM, M.R., HAFEZ, H.A., CHAI, X., BESTEIRO, L. V., TAN, L., OZAKI, T., GOVOROV, A.O., IZQUIERDO, R. & MA, D.. 2013. Nanoscale. *Nanoscale* **0** pp. 1–3.

KNIGHT, E.R., COWLEY, A.R., HOGARTH, G. & WILTON-ELY, J.D.E.T.. 2009. Bifunctional dithiocarbamates: a bridge between coordination chemistry and nanoscale materials. *Dalton Trans.* **9226** (4) pp. 607–609.

KOLE, A.K. & KUMBHAKAR, P.. 2012. Cubic-to-hexagonal phase transition and optical properties of chemically synthesized ZnS nanocrystals. *Results Phys.* **2** pp. 150–155.

LEE, E.J.H., RIBEIRO, C., LONGO, E. & LEITE, E.R.. 2005. Oriented attachment: An effective mechanism in the formation of anisotropic nanocrystals. *J. Phys. Chem. B* **109** (44) pp. 20842–20846.

LI, W., SHAVEL, A., GUZMAN, R., RUBIO-GARCIA, J., FLOX, C., FAN, J., CADAVID, D., IBÁÑEZ, M., ARBIOL, J., MORANTE, J.R., ET AL.. 2011. Morphology evolution of Cu(2-x)S nanoparticles: from spheres to dodecahedrons. *Chem. Commun. (Camb)*. **47** (37) pp. 10332–10334.

LIU, Y., DONG, W., ZHANG, Y., HUANG, C., SUN, Y., CHEN, X. & DAI, N.. 2013. Surface-Dependent Localized Surface Plasmon Resonances in CuS Nanodisks Surface-Dependent Localized Surface Plasmon Resonances in CuS Nanodisks. *ACS Appl. Mater. Interfaces* **5** (21) pp. 10473–10477.

LUTHER, J.M., JAIN, P.K., EWERS, T. & ALIVISATOS, A P.. 2011. Localized surface plasmon resonances arising from free carriers in doped quantum dots. *Nat. Mater.* **10** (5) pp. 361–366.

NIEZGODA, J.S. & ROSENTHAL, S.J.. 2016. Synthetic Strategies for Semiconductor Nanocrystals

Expressing Localized Surface Plasmon Resonance. **17** pp. 645–653.

OLUWAFEMI, O.S., MOHAN, S., OLUBOMEHIN, O., OSIBOTE, O. A. & SONGCA, S.P.. 2016. Size tunable synthesis of HDA and TOPO capped ZnSe nanoparticles via a facile aqueous/thermolysis hybrid solution route. *J. Mater. Sci. Mater. Electron.* **27** (4) pp. 3880–3887.

PATEL, P.C., SRIVASTAVA, N. & SRIVASTAVA, P.C.. 2013. Synthesis of wurtzite ZnS nanocrystals at low temperature. *J. Mater. Sci. Mater. Electron.* **24** (10) pp. 4098–4104.

PATHAK, C.S., MISHRA, D.D., AGARWALA, V. & MANDAL, M.K.. 2012. Optical properties of ZnS nanoparticles produced by mechanochemical method. *Ceram. Int.* **38** (8) pp. 6191–6195.

REVAPRASADU, N. & MLONDO, S.N.. 2006. Use of metal complexes to synthesize semiconductor nanoparticles. *Pure Appl. Chem.* **78** (9) pp. 1691–1702.

SANGHAMITRA, N.J.M. & MAZUMDAR, S.. 2008. Effect of polar solvents on the optical properties of water-dispersible thiol-capped cobalt nanoparticles. **24** (7) pp. 3439–3445.

SANJAY, S.S. & PANDEY, A.C.. 2016. EMR/ESR/EPR Spectroscopy for Characterization of Nanomaterials. *Springer Handb. Nanotechnol.* **62** p. 179.

SEKHAR TIWARY, C., SRIVASTAVA, C. & KUMBHAKAR, P.. 2011. Onset of sphalerite to wurtzite transformation in ZnS nanoparticles. *J. Appl. Phys.* **110** (3) p. 34908.

SHANMUGAM, N., CHOLAN, S., KANNADASAN, N., SATHISHKUMAR, K. & VIRUTHAGIRI, G.. 2013. Effect of Annealing on the ZnS Nanocrystals Prepared by Chemical Precipitation Method. **2013** .

- SPERLING, R. A & PARAK, W.J.. 2010. Surface modification, functionalization and bioconjugation of colloidal inorganic nanoparticles. *Philos. Trans. R. Soc. A* **368** (1915) pp. 1333–1383.
- WELLER, H.. 1993. Colloidal Semiconductor Q-Particles: Chemistry in the Transition Region Between Solid State and Molecules. *Angew. Chemie Int. Ed. English* **32** (1) pp. 41–53.
- YEH, C.Y., LU, Z.W., FROYEN, S. & ZUNGER, A.. 1992. Zinc-blendewurtzite polytypism in semiconductors. *Phys. Rev. B* **46** (16) pp. 10086–10097.
- ZHAO, Y., ZHANG, Y., ZHU, H., HADJIPANAYIS, G.C. & XIAO, J.Q.. 2004. Low-temperature synthesis of hexagonal (wurtzite) ZnS nanocrystals. *J. Am. Chem. Soc.* **126** (22) pp. 6874–6875.

Chapter 5

Overall conclusions, recommendations and future work

5.1 Overall conclusions

Since the breakthrough of the 1,1-dithiolates, the use of dithiolate ligands in the synthesis of metal complex has gained considerable interest in various fields. In this study dithiocarbamate complexes were used as molecular precursors for the synthesis of ZnS and Cu_{2-x}S nanoparticles. Therefore several conclusions can be drawn from this work as listed below:

(i) **Dithiocarbamate ligands and their complexes**

Chapter 3 contained the results and discussion of the prepared ligands and complexes, which gave an insight on the binding sites and the formation of the prepared dithiocarbamates. The formation of the ligands were confirmed by FTIR and NMR spectroscopy. Their complexes were also characterized by FTIR and NMR spectroscopy and their stability was analyzed by TGA. The spectroscopic studies of the ligands suggested the bonding of the CS₂ moiety through the nitrogen atom of the amine group. This was confirmed by FTIR analysis that showed the NCS₂ and CS that were between the single and double bond character of the dithiocarbamate compounds, with their peaks shifting upon complexation. The bonding was further confirmed by NMR analysis that showed signals that corresponds to the predicted structure. In the NMR analysis of all the ligands and complexes (the exceptions were complex 1, 3 and paramagnetic copper complexes; their signals could not be detected), the ¹³NCS₂ signal was observed in the chemical shifts number range of 199-206 ppm. These chemical shifts were in agreement with findings of other researchers. In

terms of the purity of the synthesized samples, they were less pure in comparison to the complex prepared from bis(N-pyrrolidinedithiocarbamate)Zn(II). On the other hand the complex stability was studied and all the complexes gave a final residue of metal sulfide (except complex 1 which gave Zn residue), thus showing their effectiveness as molecular precursors in the synthesis of metal sulfide nanoparticles.

(ii) **ZnS and Cu_{2-x}S nanoparticles**

The thermolysis of the metal complexes in HDA and TOPO at 120 °C gave metal sulfide nanoparticles. Several instruments were used to characterize the prepared nanoparticles, the optical properties were studied by ultraviolet visible (UV-Vis) and photoluminescence (PL) spectrophotometry, the crystal structure was determined from the X-ray diffraction (XRD) and the morphology and size were obtained from transmission electron microscopy. In the ZnS nanoparticles, the absorption spectra were red-shifted (except nanoparticles from the aniline ligand) from the bulk ZnS (345 nm) this was attributed to the surface trap states that are caused by impurities. The assumption was confirmed by XRD analysis that showed the triclinic sulfur impurity in the nanoparticles prepared from HDA as a capping agent, while some of the TOPO-capped nanoparticles also showed the presence of impurities. The phases obtained from the XRD data was the hexagonal phase for samples prepared in HDA and cubic phase was obtained in the TOPO-capped nanoparticles. The XRD data was also used to calculate the size of nanoparticles using the Scherrer equation. The smaller crystallite sizes were further confirmed by the TEM images (other particle sizes were not comparable with crystal sizes) which also showed that the synthesized nanomaterials were very small quantum dots.

On the Cu_{2-x}S nanoparticles the optical properties indicated the formation of the electron deficient copper sulfide. The electron deficient stoichiometry was indicated by the formation of localized surface plasmon resonances, showing emergence of an apparent peak formed at the near infrared region. The stoichiometry was further confirmed by XRD results that gave a hexagonal phase CuS covellite. In some instances the disappearance of the resonance peaks in the absorption spectra was accompanied by the formation of an electron rich stoichiometry (Cu_2S) in the XRD analysis. The broadening of the peaks in the XRD spectra indicated the formation of particles in the nano-regime. The formation of nanoparticles was confirmed by TEM results, which showed small nanoparticles or quantum dots.

This study was based on determining the effect of capping molecule and their concentrations on the formation of nanoparticles. For the ZnS nanoparticles the TOPO-capped nanoparticles were better passivated as seen by an absence of impurity peaks in most of their XRD spectra. For the HDA capped CuS nanoparticles gave well dispersed nanoparticles. While the 6g was found to be the optimum concentration since most of the nanoparticles on this concentration were small and well dispersed. The ligands also showed an effect on the synthesis of nanoparticles. The nanoparticles synthesized from cyclohexylamine ligand were better dispersed and their particles were smaller sizes compared to other ligands.

5.2 Recommendations and future work

I would recommend that on the synthesis of nanoparticles the temperatures should be increased to at least $180\text{ }^\circ\text{C}$ since at elevated temperatures both the nucleation and growth stage takes place in

much faster rate. The increased temperature would also eliminate the amorphous XRD peaks and impurities. The concentration can also be increased to 9g to check what effect it would have.

Since these CuS nanoparticles were small in sizes, they can be used as drug delivery system for biological application. The issue now is the hydrophobic capping agents used (in this study) that would hinder their application in biology. So the future work would be to make their nanocomposites that would render them biocompatible and less toxic. The nanocomposites can be made by incorporating these nanoparticles in a biocompatible polymer. The plasmonic behavior of these nanoparticles can be exploited in the cancer therapies (photothermal ablation or photodynamic applications), as well as in the biological imaging applications.

Appendix

Table 8: Mole ratio of complex to capping agent concentration

Compound	Ratio for HDA	Ratio for TOPO
Complex 1	1:10 for 3g 1:20 for 6g	1:6 for 3g 1:13 for 6g
Complex 2	1:10 for 3g 1:20 for 6g	1:6 for 3g 1:13 for 6g
Complex 3	1:10 for 3g 1:20 for 6g	1:6 for 3g 1:12 for 6g
Complex 4	1:10 for 3g 1:20 for 6g	1:6 for 3g 1:12 for 6g
Complex 5	1:9 for 3g 1:18 for 6g	1:6 for 3g 1:11 for 6g
Complex 6	1:9 for 3g 1:18 for 6g	1:6 for 3g 1:11 for 6g